Title

Heterogeneously Integrated Optofluidic Platforms for Cell Patterning, Sorting and Sensing

Permalink

https://escholarship.org/uc/item/3dm0f735

Author

Zhu, Xiongfeng

Publication Date

2019

Peer reviewed|Thesis/dissertation

UNIVERSITY OF CALIFORNIA

Los Angeles

Heterogeneously Integrated Optofluidic Platforms

for Cell Patterning, Sorting and Sensing

A dissertation submitted in partial satisfaction of the

requirements for the degree Doctor of Philosophy

in Mechanical Engineering

by

Xiongfeng Zhu

2019

ABSTRACT OF THE DISSERTATION

Heterogeneously Integrated Optofluidic Platforms

for Cell Patterning, Sorting and Sensing

by

Xiongfeng Zhu

Doctor of Philosophy in Mechanical Engineering

University of California, Los Angeles, 2019

Professor Pei-Yu Chiou, Chair

Single cell analysis is the study of individual cells isolated from cell populations. A typical workflow of single cell analysis starts from a physiologically heterogeneous cell culture, and involves a high-throughput and robust isolation method based on single or multiple parameters to prepare a subpopulation of cells for further downstream processing and analysis.

New technologies are demanded to conduct single cell analysis on a finer level. Microelectromechanical systems (MEMS) provide good interface with cells because of comparable feature size, and have the advantages of device miniaturization and process integration,

thus are suitable for biological studies. In this dissertation, I focus on developing heterogeneously integrated optofluidic platforms for applications in cell manipulation and sensing.

We first demonstrate a novel dielectrophoresis-integrated pulsed laser activated cell sorter (DEP-PLACS). It consists of a microfluidic channel with 3D electrodes laid out to provide a tunnel-shaped electric field profile for sheathless focusing of microparticles/cells into a single stream in high-speed microfluidic flows. DEP-PLACS has achieved a sorting purity of 91% for polystyrene beads at a throughput of 1,500 particles/sec.

To achieve enhanced DEP forces in high conductivity media, which can potentially improve manipulation throughput in a biocompatible environment, hemispherically shaped, heavily doped (N++) silicon electrode is proposed to decouple the strong electric field region from the electrode interface and provides a large interface capacitance to prevent surface charging in high conductivity media, thereby effectively suppressing electrochemical reactions. Compared to conventional metal electrode, N++ electrode can provide 3 times higher threshold voltage and a corresponding 9-fold enhancement of maximum DEP force in 1× PBS buffer with an electrical conductivity of 1 S/m.

As one kind of downstream analysis, mechanobiology has been an emerging cross-disciplinary field that studies the mechanical properties of cells and tissues and how physical forces can contribute to the changes in biological events such as cell differentiation and disease development. Over the past years several tools and approaches have been developed for quantifying mechanical properties of biological samples. However, the throughput is usually low

and obtaining statistically significant data can be difficult. To address this problem, we proposed a mechanobiological measurement platform consisting of two major steps: high-throughput cell patterning and parallel pressure sensing.

For the first step we developed a novel and simple technique called lift-off cell lithography (LCL). Our approach borrows the key concept of lift-off lithography from microfabrication and utilizes a fully biocompatible process to achieve high-throughput, high-efficiency cell patterning with nearly zero background defects across a large surface area. Using LCL, we reproducibly achieved > 70% patterning efficiency for both adherent and non-adherent cells with < 1% defects in undesired areas.

For the second step we developed a pressure-sensing substrate that can monitor pressure distribution across a large area with high spatial resolution by utilizing colorimetric interferometry and image-based measurements. Vertical optical micro-cavities are constructed on a silicon substrate and covered by a thin planar layer of polymer material that deforms under pressure. Local measurement of pressure is realized by monitoring the change of reflected color spectrum from each micro-cavity. Pressure distribution across 1 cm^2 area with a spatial resolution of 50 μm has been achieved. We demonstrate a measurement range of 0-5psi with < 0.2 psi error. The measurement range can be customized by tuning the design and material properties depending on the specific application such as biological cell or tissue stiffness measurement.

The dissertation of Xiongfeng Zhu is approved.

Lihua Jin

Chang-Jin Kim

Michael Teitell

Pei-Yu Chiou, Committee Chair

University of California, Los Angeles

2019

CONTENTS

LIST OF FIGURES

ACKNOWLEDGEMENTS

First, I would like to thank my advisor Professor Pei-Yu Chiou for his guidance and support in my study and research during the past five years. His passion for technical innovation has motivated me to embrace challenges and open myself up to new opportunities. I would also like to thank Professor Michael Teitell for countless discussion with invaluable insight and knowledge in the fields of biological studies. I thank Professor Chang-Jin Kim and Professor Lihua Jin for serving on my dissertation committee and providing professional suggestions on my work.

I am also sincerely grateful to all my colleagues from Optofluidics Systems Lab. I would like to thank Dr. Ting-Hsiang Wu and Dr. Yu-Chun Kung for being my research mentors on optical system setup and microfabrication techniques when I joined the lab. Kuan-Wen Tung, Cong Wu and Tianxing Man have also contributed significantly to my projects with their expertise. Many thanks go to Dr. Tingyi Liu, Dr. Ximiao Wen, Dr. Yu Ting Chow, Dr. Fan Xiao, Yajia Yang, Meng-Shiue Lee, Pei-Shan Chung and Xing Haw Tan for their tremendous support and inspiration.

Finally, deepest thanks to my family for their unconditional love and support throughout all these years.

VITA

Education

2012 – 2014   M.S., Mechanical Engineering

                 Purdue University, West Lafayette, Indiana

2009 – 2013   B.S., Mechanical Engineering

                 Shanghai Jiao Tong University, Shanghai, China

Publications and Presentations

[1]   T. Man, **X. Zhu**, Y. T. Chow, E. R. Dawson, X. Wen, A. N. Patananan, T. L. Liu, C. Zhao, C. Wu, J. S. Hong, P.-S. Chung, D. L. Clemens, B.-Y. Lee, P. S. Weiss, M. A. Teitell, P.-Y. Chiou, *ACS Nano* **2019**, *13*, 10835.

[2]   C. Wu, **X. Zhu**, T. Man, P. Y. Chiou, *22nd International Conference on Miniaturized Systems for Chemistry and Life Sciences* **2018**.

[3]   *C. Wu, ***X. Zhu**, T. Man, P.-S. Chung, M. A. Teitell, P.-Y. Chiou, *Lab Chip* **2018**, *18*, 3074.

[4]   **X. Zhu**, T. Man, T. Nguven, M. T. Xing Haw, T. L. Liu, X. Wen, M. A. Teitell, P.-Y. Chiou, in *2018 International Conference on Optical MEMS and Nanophotonics (OMN)*, IEEE, Lausanne, **2018**, pp. 1–2.

[5]   Chow Yu Ting, Man Tianxing, Acosta-Vélez Giovanny F., **Zhu Xiongfeng**, Wen Ximiao, Chung Pei-Shan, Liu Tingyi "Leo," Wu Benjamin M., Chiou Pei-Yu, *Advanced Science* **2018**, *0*, 1700711.

[6]   Y. T. Chow, T. Man, G. F. Acosta-Vélez, **X. Zhu**, X. Wen, P. Chung, T. L. Liu, B. M. Wu, P. Chiou, in *2018 IEEE Micro Electro Mechanical Systems (MEMS)*, **2018**, pp. 125–128.

[7]   **X. Zhu**, K.-W. Tung, P.-Y. Chiou, *Applied Physics Letters* **2017**, *111*, 143506.

[8]   **X. Zhu**, Y.-C. Kung, T.-H. Wu, M. A. Teitell, P.-Y. Chiou, International Society For Optics

And Photonics, **2017**, p. 103472K.

[9]   T. Man, **X. Zhu**, Y. T. Chow, T. L. Liu, X. Wen, M. A. Teitell, P. Y. Chiou, in *2017 International Conference on Optical MEMS and Nanophotonics (OMN)*, **2017**, pp. 1–2.

[10] **X. Zhu**, Y. C. Kung, T. H. Wu, M. A. Teitell, P. Y. Chiou, in *2017 IEEE 30th International Conference on Micro Electro Mechanical Systems (MEMS)*, **2017**, pp. 1260–1263.

[11] Y. J. Yang, Y. F. Mao, **X. F. Zhu**, K. S. Shin, C. O. Chui, P. Y. Chiou, in *2015 Transducers - 2015 18th International Conference on Solid-State Sensors, Actuators and Microsystems (TRANSDUCERS)*, **2015**, pp. 654–657.

Chapter 1 Introduction

1.1 Single cell analysis and bio-MEMS systems

Single cell analysis is the study of individual cells isolated from cell populations[1]. A typical workflow of single cell analysis starts from a physiologically heterogeneous cell culture, and involves a high-throughput and robust isolation method based on single or multiple parameters to prepare a subpopulation of cells for either further downstream processing such as drug delivery or gene editing, or analyzing their response to perturbations.
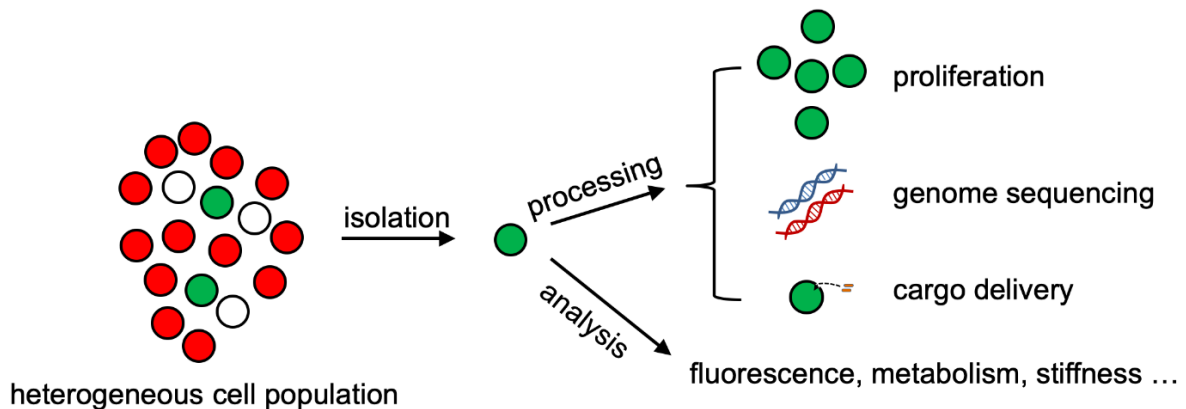
Figure 1.1 Examples of work flow for single cell analysis

New technologies are demanded to conduct single cell analysis on a finer level. In fact, many microelectromechanical systems (MEMS) provide good interface with cells because of comparable feature size, and have the advantages of device miniaturization and process integration, thus are suitable for biological studies. On one hand, MEMS platforms can provide high degree of freedom of control in single cell manipulation and high precision for cell processing. Microarrays, which provide a collection of microspots for cells to rest and efficiently interact with small volume of reagents, are widely used for high-throughput and low-cost cell study[2], [3] or genome analysis[4]. Microfluidic-based cell sorting devices aim to overcome issues of conventional

fluorescence-activated cell sorters (FACS) by removing biohazardous aerosol formation, providing more flexibility in integration and miniaturization while maintaining the same level of performance[5], [6]. Optoelectronic tweezers are able to precisely manipulate single cells in a massively parallel fashion, which has found broad applications in cell therapies, drug screening and gene editing[7], [8]. Laser-assisted heating of micro-scale structures can open tiny pores on cell membrane and precisely control the volume of cargo delivered into cells[9], [10].
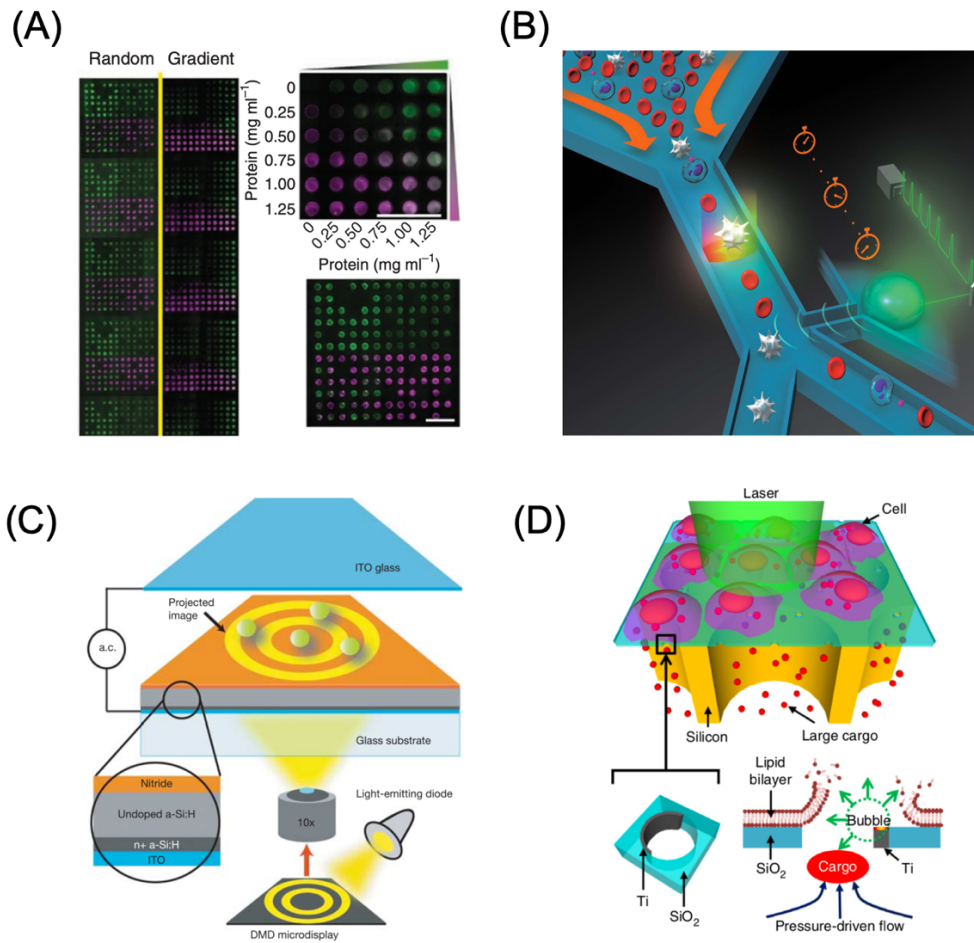
Figure 1.2 Examples of MEMS systems for cell manipulation and processing. (A) Microarray for probing single stem cell fate in high throughput[3]. (B) 3D pulsed laser-triggered high-speed microfluidic fluorescence-activated cell sorter[5]. (C) Massively parallel manipulation of single cells and microparticles using optical images[7]. (D) Massively parallel delivery of large cargo into mammalian cells with light pulses[9].

On the other hand, MEMS sensors have demonstrated advantages of high sensitivity and precision in measurement of biological samples. Micro and nano scale cantilevers and membranes are used as micromechanical sensors to probe the mechanobiological properties of cells and tissues and reveal new findings and insights [11], [12]. Intricately designed micro-electrodes and probes can detect trace amount of biomolecules such as glucose, lactose and cholesterol with high sensitivity[13]. Nano-scale periodic grating structures are also used as surface plasmon resonance (SPR) based optical sensors for similar applications of low-level biomolecule detection in food quality and safety analysis, medical diagnosis and environmental monitoring[14], [15].
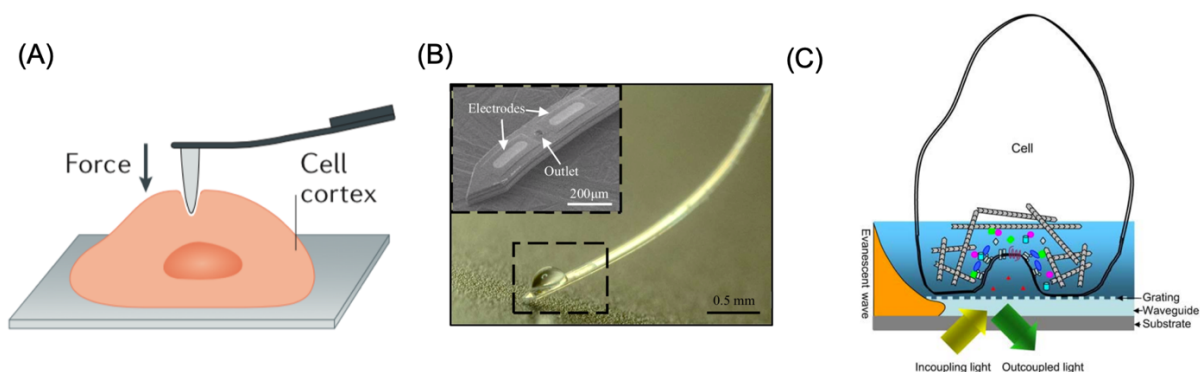
Figure 1.3 Examples of MEMS systems for biological sensing. (A) AFM tips used to probe cellular mechanical property[12]. (B) Flexible, multifunctional neural probe for deep-brain chemical sensing and agent delivery[13]. (C) Resonant waveguide grating biosensor for living cell sensing[15].

1.2 Heterogeneously integrated optofluidic platforms for manipulation and sensing of biological cells

Since the introduction of PDMS-based microfabrication, the field of bio-MEMS has experienced rapid expansion. As the most commonly used elastomeric material, PDMS has unique features of being optically transparent, gas-permeable, chemically inert and non-toxic[16], [17]. These properties make it a suitable material for constructing microfluidic devices for cell

3

manipulation and measurement. Through oxygen plasma treatment, activated PDMS surface can be permanently bonded to glass or silicon dioxide surfaces to provide a good interface to heterogeneously integrate with other mechanical, electrical and optical components[13], [18].
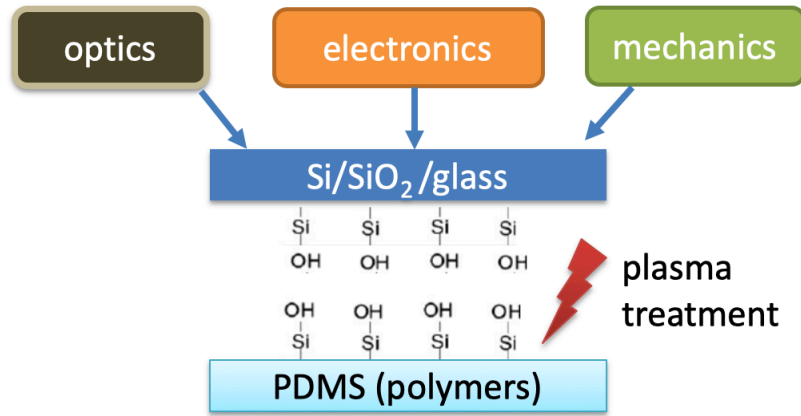
Figure 1.4 Heterogeneous integration of PDMS with optical, electronic and mechanical components.

In this dissertation I focus on the development of heterogeneously integrated optofluidic platforms for two major tasks: cell manipulation and sensing. The first part cell manipulation includes the following systems and devices:

(1) Pulsed laser activated cell sorting (PLACS) for rare cell sorting with sheathless single stream dielectrophoretic (DEP) focusing,

(2) Improve the maximum DEP force that can be induced in high conductivity media without electrolysis by using heavily doped silicon as a new type of electrode,

(3) Lift-off Cell Lithography for Cell Patterning with Clean Background

As one kind of downstream analysis, mechanobiology has been an emerging cross-disciplinary field that studies the mechanical properties of cells and tissues and how physical forces can contribute to the changes in biological events such as cell differentiation and disease

4

development. Over the past decade multiple tools and approaches have been developed for quantifying mechanical properties of biological samples. However, the throughput is usually low and obtaining statistically significant data can be difficult.
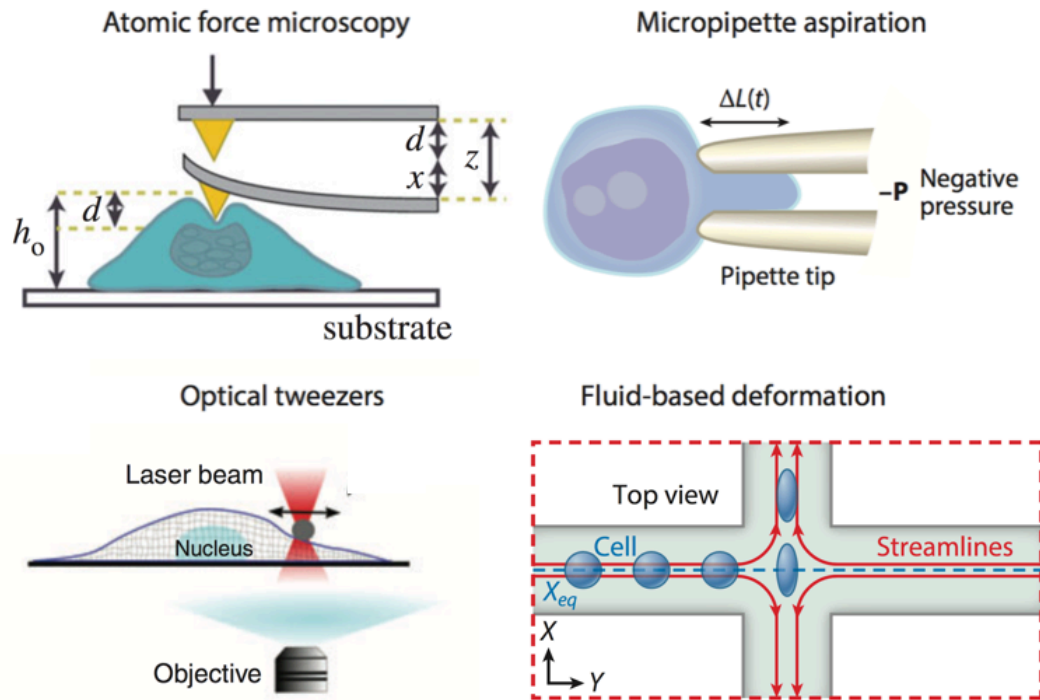
Figure 1.5 Cell stiffness measurement platforms[19].

To probe the mechanical properties of cells we need to detect small amount of displacement, typically in the range of hundred nanometers. While atomic force microscope (AFM) has been considered the gold standard to measure nanometer scale displacement, it is a low throughput method. To address this problem, we investigated two possible approaches to probe cells in parallel while maintaining good sensing ability:

(1) Parallel nanomechanical indentation platform using quantitative phase imaging

(2) Microfluidic pressure distribution mapping using colorimetric interferometry

By developing the nanomechanical force/pressure measurement platforms, along with the clean array pattern of cells onto the platforms using LCL, we can potentially achieve the goal of measuring mechanical properties of biological cells with high throughput.

Chapter 2 Optofluidic Platforms for Cell Manipulation

2.1 3D Dielectrophoretic focusing integrated pulsed laser activated cell sorter

2.1.1 Introduction

Fluorescence-activated cell sorter (FACS) is widely used for single cell analysis in both fundamental biomedical research and clinic applications. In conventional FACS, cells are focused to the center of a stream by sheath flows and pass through a fluorescence detection zone. After exiting a narrow nozzle, the stream of cells is broken into individual droplets that can be selectively charged and deflected based on detected fluorescence signals. However, this droplet approach can result in biohazardous aerosol formation which exposes the operator to potential contamination and infection[20]. It is also difficult to integrate additional upstream or downstream modules with conventional FACS to perform multiple functions in one single run.
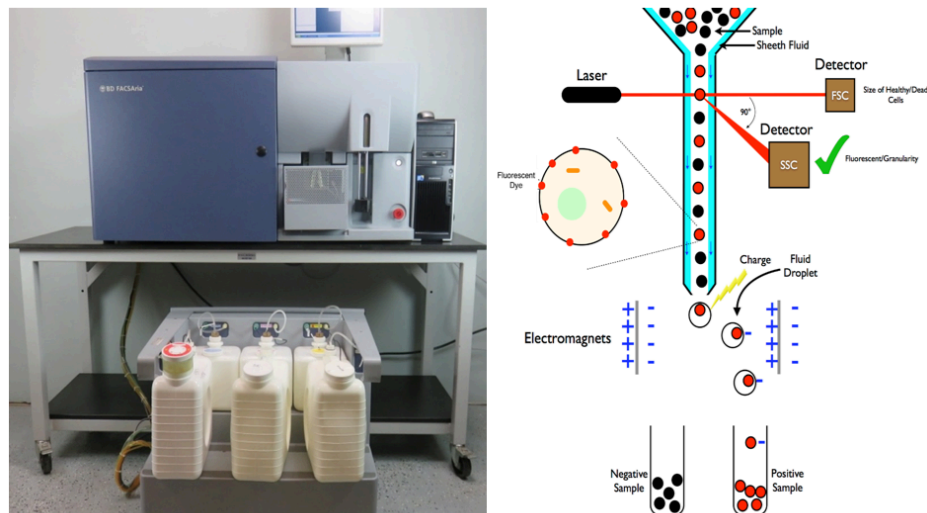
Figure 2.1 Conventional fluorescence-activated cell sorters.

Microfluidic fluorescence activated cell sorting (μFACS) systems aim to provide a fully enclosed environment for sterile cell sorting by eliminating droplet and aerosol formation.

Moreover it has the advantage of integration with upstream pre-sort and downstream post-sort modules to provide flexible sample handling and versatile sample analysis. To narrow down the gap of performance between microfluidic FACS and conventional aerosol-based FACS, several active sorting mechanisms have been employed, including pneumatic valve control[21], piezoelectric actuation[22], optical force switching[23], acoustic wave actuation[24] and pulsed laser activated cell sorting (PLACS)[25]. Among them PLACS shows a great potential in achieving comparable performance to commercial aerosol-based FACS. By utilizing the rapid (~30 µs) and precise fluid perturbation from pulsed laser induced cavitation bubbles, PLACS has achieved a sorting performance of 90% sort purity at 23000 cells sec^{-1} using 3D sheath flows[5]. However due to the large sheath-to-sample flow ratio it suffers from severe sample dilution and requires a high initial sample concentration (>10[7] ml^{-1}), which is not practical for certain applications such as rare cell sorting. Hence a sheathless focusing mechanism is preferred.
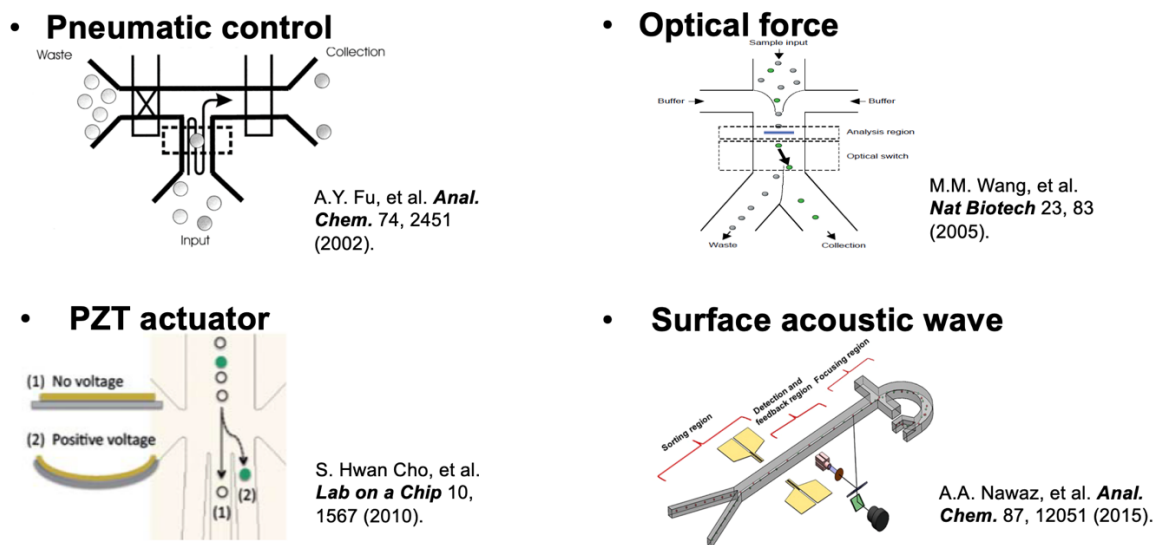
Figure 2.2 Example of microfluidic active sorting mechanisms.

Inertial focusing provides a sheathless mechanism by utilizing inertial forces on particles in high-speed flows in microfluidic channels. However, the focusing effect is size-dependent and

a stable single stream focusing is difficult to obtain[6]. Tuning the focusing location is also difficult since the equilibrium position is dependent upon channel geometry and flow speed.

Here we demonstrate a new dielectrophoretic focusing integrated pulsed laser activated cell sorter (DEP-PLACS) featuring continuous, sheathless, size-independent, real-time tunable, 3D dielectrophoretic single stream focusing for high throughput and high purity sorting.

2.1.2 Dielectrophoretic focusing integrated PLACS

2.1.2.1 Device structure

Figure 2.3 shows the schematic of DEP-PLACS. In the DEP-PLACS system the upstream main channel carrying the sample flow is a 80 μm wide and high, 4 cm long heterogeneously integrated PDMS microchannel. On top and bottom glass substrates the quadro-electrode layout spans the whole length of the main channel to provide an extremely long dielectrophoretic interaction length for focusing cells in high-speed flows. The main channel is divided into two branches in the downstream, one for target sample collection and another for waste. Both are 80 μm in height and 40 μm in width. At the bifurcation the main channel is connected to the dye channel, which is 150 μm in width and expands to 300 μm at the bubble excitation location, by a nozzle of 60 μm in length and 20 μm in width. The device is fabricated by utilizing thin film PDMS fabrication processes[18], [26], [27]. Figure 2.4 shows the schematic of fabrication process flow of the device.
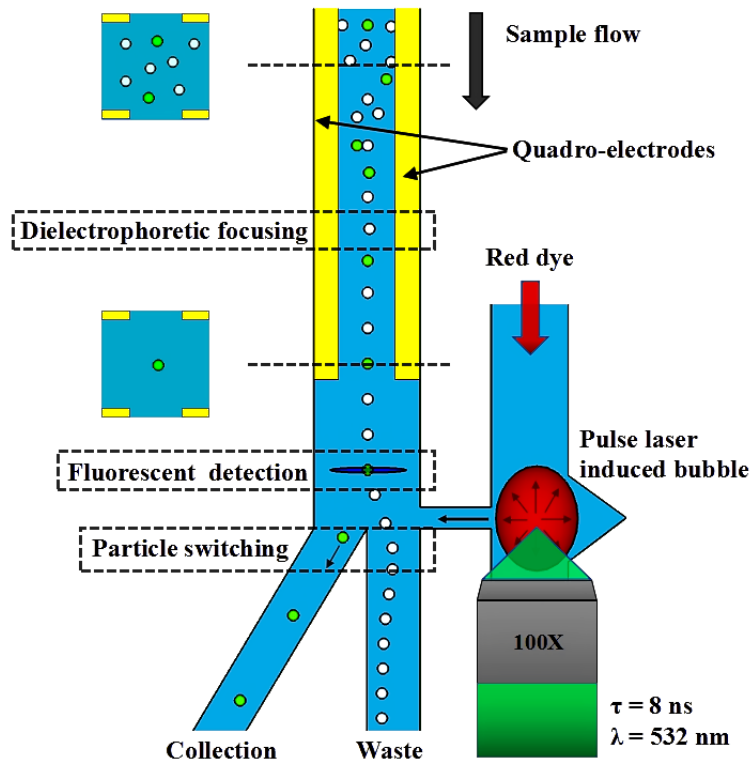
Figure 2.3 Schematic of the DEP-PLACS system for sheathless high throughput and high purity cell sorting. *Randomly distributed particles are focused into a single stream using negative DEP and sorted into separate channels based on fluorescence properties by pulsed laser induced cavitation bubbles.*
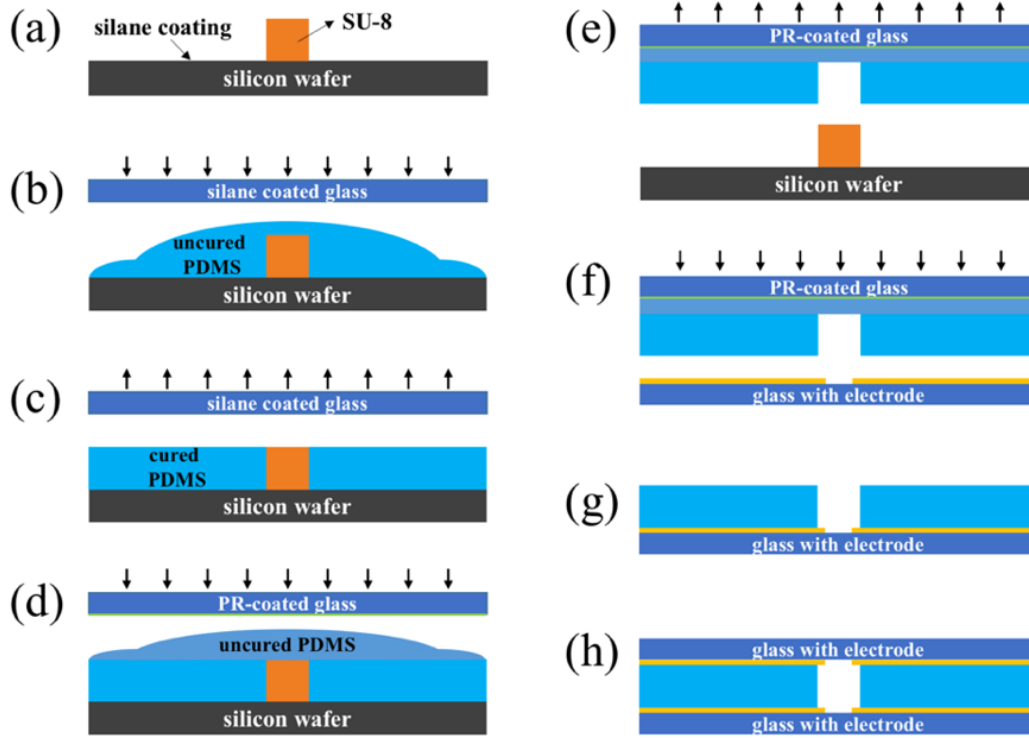
Figure 2.4 Fabrication process of DEP-PLACS device. *(a) A SU-8 mold is treated with silane to facilitate later demolding. (b) Uncured PDMS mixture is poured onto the mold and pressed by a heavily silane-treated glass slide. (c) Glass slide is removed and PDMS thin film stays in the mold. (d) New uncured PDMS is poured onto PDMS thin film and pressed by a PR-coated glass. (e) PDMS thin film is picked up by the stamp. (f) PDMS thin film is oxygen-plasma treated and aligned to bond to the glass substrate with electrode layout. (g) Top glass slide is removed by dissolving PR in acetone, and then the PDMS buffer layer is peeled off. (h) Align and cover the device with another thin glass substrate with electrode layouts to complete the fabrication process.*

2.1.2.2 Tunable single stream dielectrophoretic focusing

Dielectrophoresis (DEP) is the phenomenon in which a force is exerted on a dielectric particle when it is subjected to a non-uniform electric field. It is widely used to manipulate, transport, separate and sort different types of particles. For a homogeneous sphere of radius r and complex permittivity ε_p^* in a medium with complex permittivity ε_m^* the time-averaged DEP force can be modeled as

$$\langle F_{DEP} \rangle = 2\pi r^3 \varepsilon_m \, \mathrm{Re} \left\{ \frac{\varepsilon_p^* - \varepsilon_m^*}{\varepsilon_p^* + 2\varepsilon_m^*} \right\} \nabla \left| \vec{E}_{rms} \right|^2$$
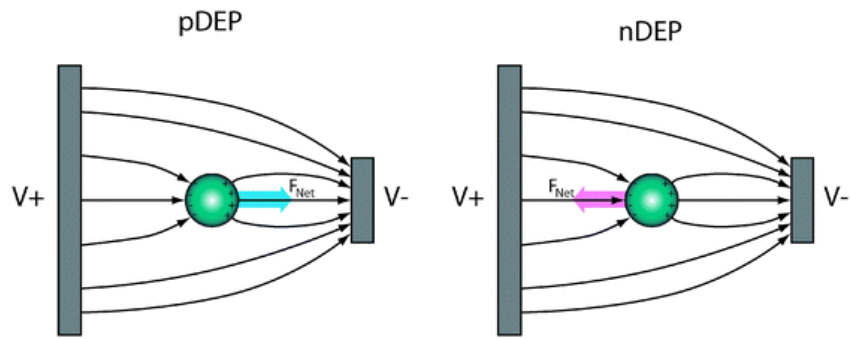
Figure 2.5 Schematics of positive and negative DEP.

When an a.c. signal is applied symmetrically to the electrodes, a tunnel-shaped electric field potential profile forms along the channel. Figure 2.6(a) presents the numerically simulated electric field distribution in the microchannel with a single field minimum at the center.
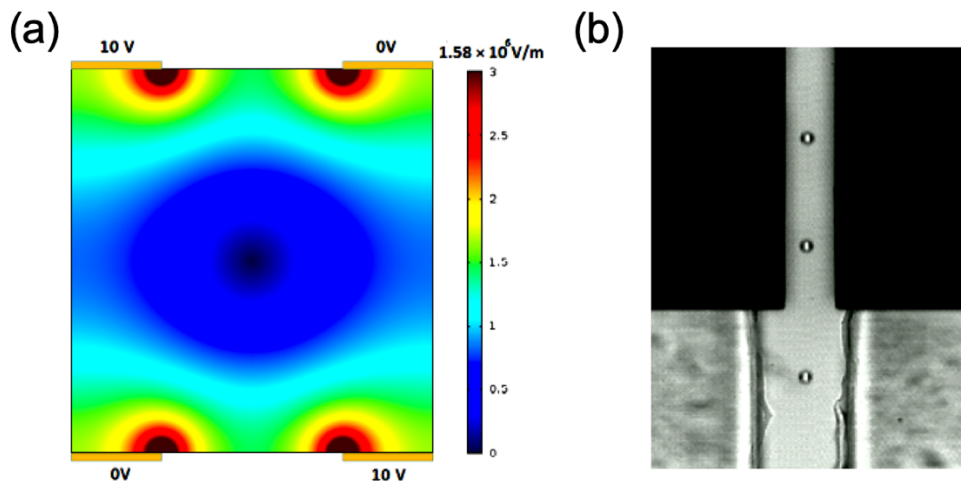
Figure 2.6 Single stream DEP focusing. *(a) Quadro-electrodes generate a single electric field minimum at the center of the microchannel when a.c. signals applied symmetrically. (b) A high-speed imaging of polystyrene beads focused into a single stream after 4 cm long interaction distance with a particle speed of 16 cm/s, 1S/m medium conductivity, and 20 $V_{p\text{-}p}$ electrical voltage applied.*

12

The location of the field minimum can also be tuned in the cross section by changing voltage combinations applied to the electrodes[28]. This can be a useful feature to achieve consistent focusing position even if electrodes are not aligned perfectly during fabrication processes, because detected particles at different streamline arrive at the switching zone at different time and the successful switching relies on precise synchronization in time (Figure 2.7). It can also be used to combine with flow ratio adjustment to guide particles into desired downstream outlets as shown in Figure 2.8.
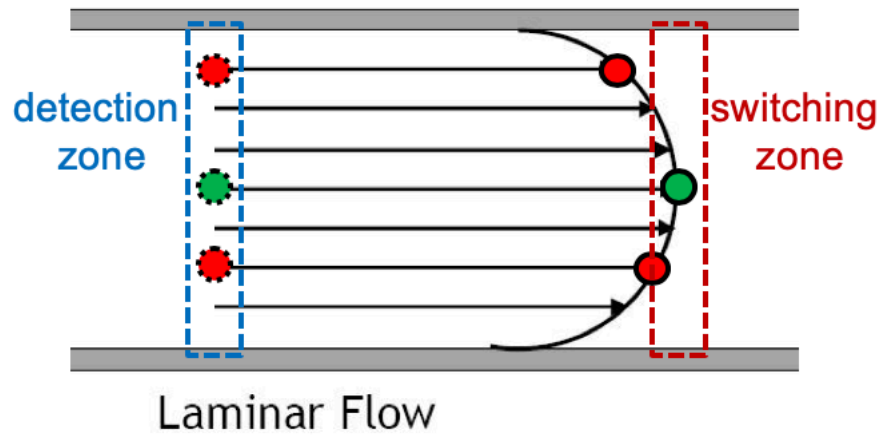
Figure 2.7 Detected particles at different streamline arrive at the switching zone at different time.
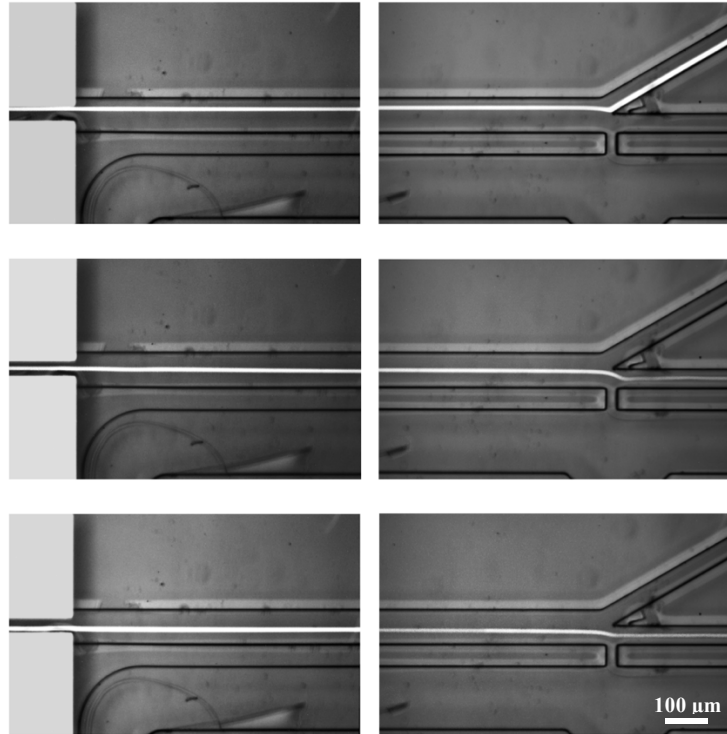
Figure 2.8 Tunable single stream focusing to guide fluorescent polystyrene beads into different downstream outlets.

For a particle more polarizable than the medium, it experiences positive DEP forces and tends to migrate to the electric field maximum; for a particle less polarizable than the medium, it experiences negative DEP and migrates to the field minimum. In regular physiological buffers with high conductivity (>1S/m), dielectric particles and mammalian cells show negative DEP responses at the frequency ranging from kHz to MHz and the DEP forces are weak. Generally it's more challenging to manipulate or focus particles in high conductivity media using DEP than in low conductivity buffers, in which most DEP manipulations are performed, mainly due to the small CM factor value. However for our device due to the extremely long (4 cm) interaction distance, microparticles/cells experience negative DEP forces continuously and can be focused into a single stream in high-speed flows[29]. 10 μm polystyrene spheres suspended in phosphate buffer solution

14

(PBS) with a conductivity of 1S/m can be focused into a single stream at a particle flow speed up to 16 cm/s when a 20 V_{p-p} a.c. signal is applied to the quadro-electrodes as shown in Figure 2.6(b).

2.1.2.3 Pulsed laser activated cell sorting

During cell sorting experiments focused particles are initially biased into the waste channel at the Y-junction by either adjusting the flow ratio between the main channel and dye channel, or changing the voltages applied to electrodes. A 50mW, 488nm CW laser (CrytaLaser, DL-499-50) is focused through a 25×/N.A. 0.4 objective lens into the microchannel before the bifurcation to excite fluorescence. The emission fluorescence is collected through the same objective lens and detected by a photomultiplier tube (PMT, Sens-Tech P30CWAD501) connected to a DAQ card (National Instrument, PCI 7831R) for signal acquisition and processing. Upon the detection of fluorescence a cavitation bubble is generated in the parallel dye channel induced by a 532nm ns laser pulse (Q-switched Nd;YVO4, EKSPLA, Jazz 20) focused by a 100X objective lens (N.A. 0.9). The bubble expands rapidly through the connection nozzle between the main and the dye channels (Figure 2.10), forming a high-speed liquid jet which pushes the target particle over the Y-junction into the collection channel to achieve successful switching (Figure 2.11). The cavitation bubble collapses within 30μs after triggering, which ensures fast and precise particle sorting.
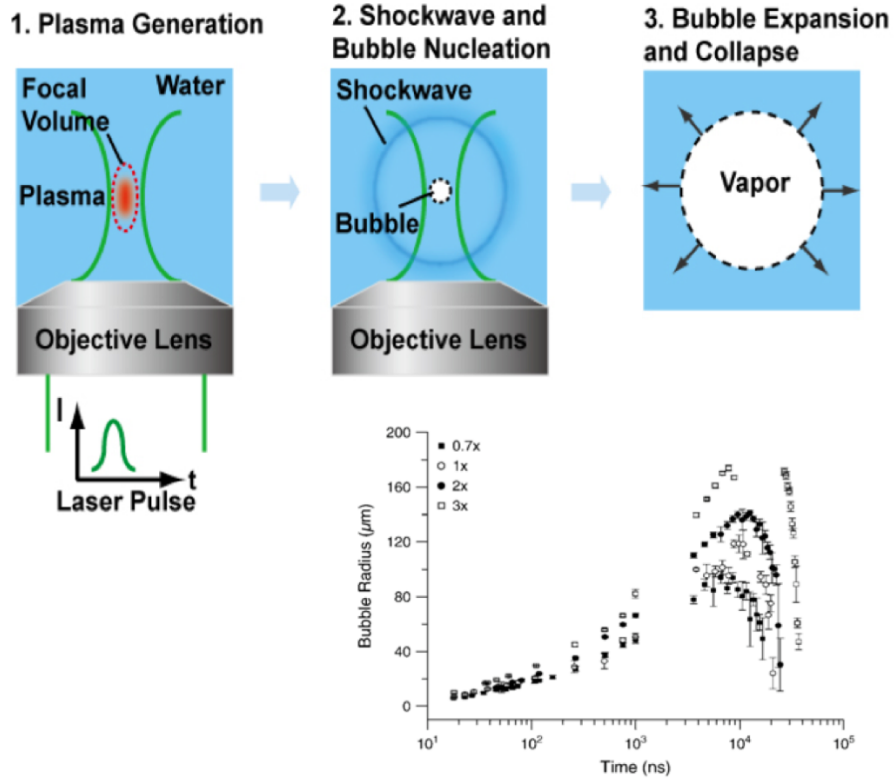
Figure 2.9 Schematic of the formation of a laser-induced cavitation bubble[30].
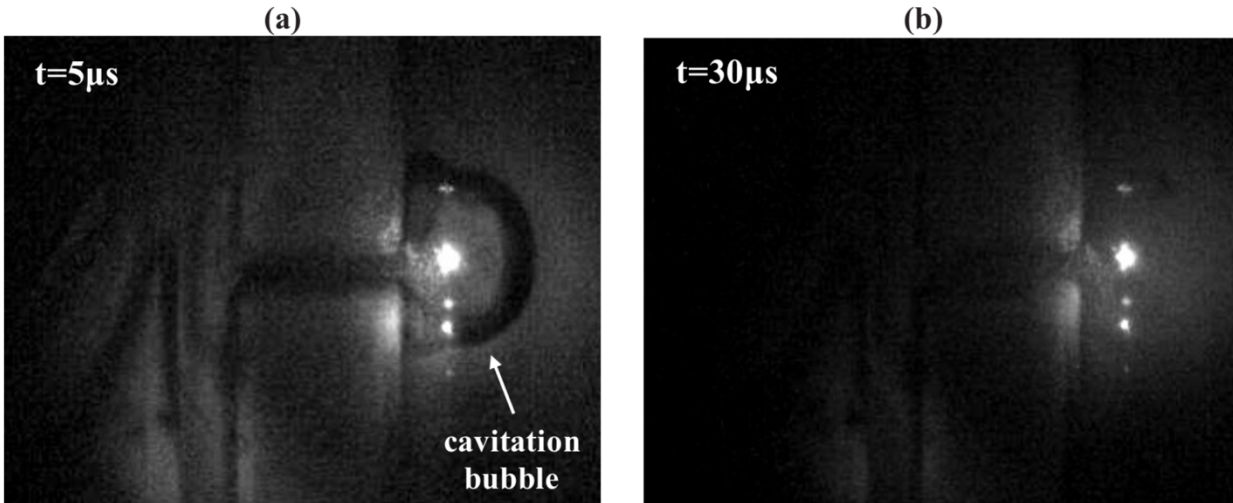
Figure 2.10 Time resolved images of a laser induced cavitation bubble. *A micro cavitation bubble induced by a ns laser pulse (a) expands to its maximum at 5 μs and (b) collapses at 30 μs. A liquid jet through the connection nozzle is formed during the rapid expansion process.*
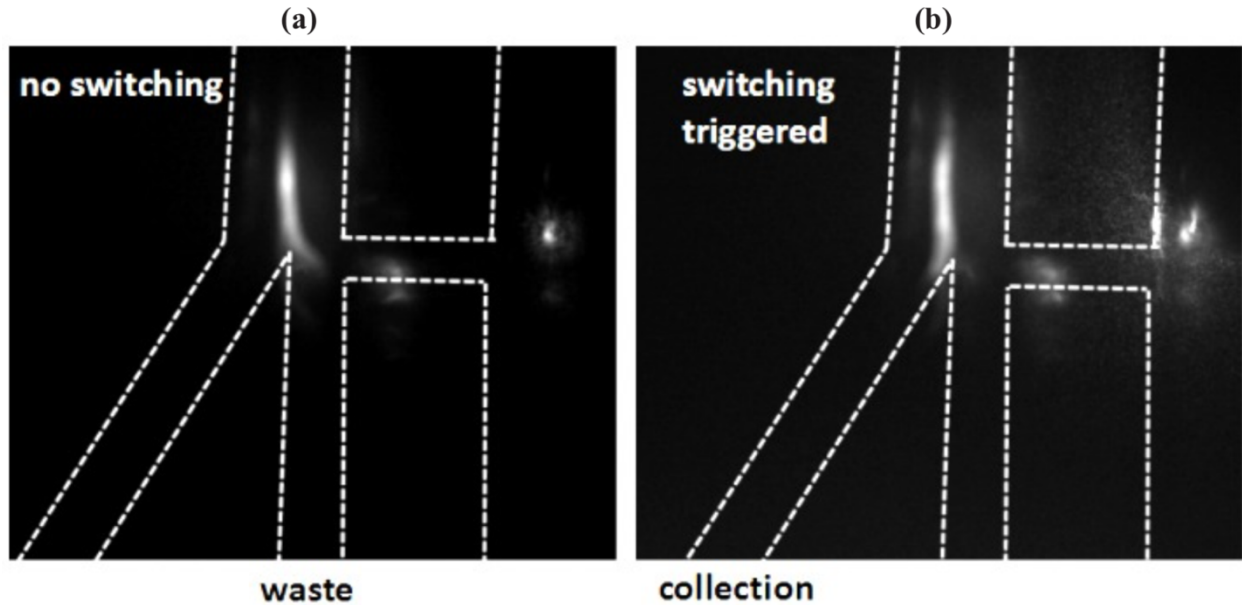
Figure 2.11 Fluorescent particle traces *showing (a) focused particles are initially biased into the waste channel without laser triggering and (b) particles successfully sorted into the collection channel. This switching is achieved by triggering a cavitation bubble in the dye channel with a ns laser pulse upon fluorescence detection.*

2.1.2.4 Sorting results

Sorting of microparticles was performed to characterize the performance of DEP-PLACS system. 10μm green fluorescent polystyrene beads (Fluoro-Max G1000) and 9μm non-fluorescent polystyrene beads (Duke Standards 4209A) were mixed at a ratio of 1:100 and the total concentration of 5.6×10^6 beads/ml. The beads were suspended in an isotonic buffer with a conductivity of 0.1S/m. The sample solution was sent into the main channel by a syringe pump (Harvard Apparatus, PHD 2000) at the flow rate of 1ml/h, which corresponds to a throughput of 1,500 particles sec^{-1}. Allura Red dye (67 mg/ml, Sigma-Aldrich) was pumped into the dye channel to reduce the laser energy threshold for bubble generation. A 20V$_{p-p}$, 1MHz a.c. signal was applied symmetrically to the quadro-electrodes to focus particles into a single stream at the center of the

channel. With synchronized fluorescence detection and pulsed laser triggering, fluorescent beads can be successfully switched into the collection. Initial mixture sample and sorted sample were analyzed by a commercial flow cytometer (BD, FACSCantoII). With the precise single stream focusing and fast particle switching, DEP-PLACS has achieved a sorting purity of 91% for polystyrene beads at a throughput of 1,500 particle/sec (Figure 2.12). The fluorescent beads were enriched from an initial mix ratio of 0.01 to a final ratio of 10.36, corresponding to a 1,036-fold enrichment.

(a) **(b)**
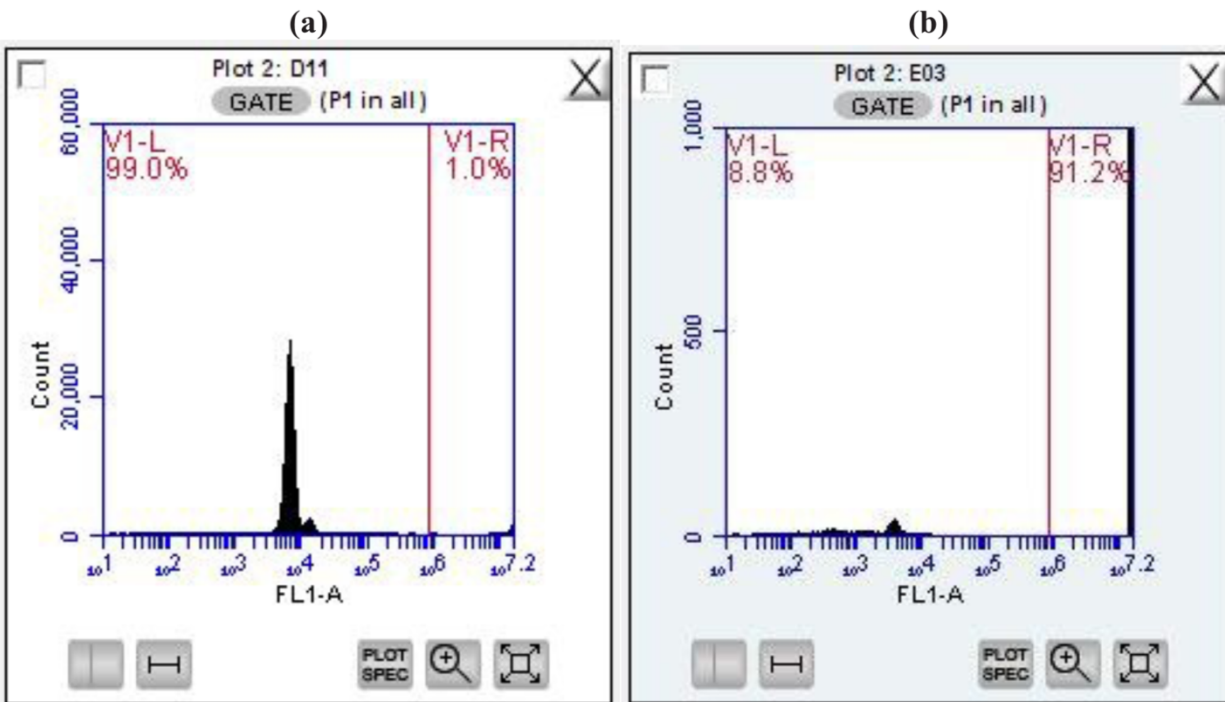
Figure 2.12 Particle sorting purity is verified by a commercial flow cytometer. *(a) 10μm green fluorescent and 9μm non-fluorescence polystyrene beads are mixed before sorting at a ratio of 0.01 with a particle concentration of 5.6×10⁶ beads/mL, sample flow rate 1ml/h, particle moving speed 10cm/s. (b) After sorting sample collected has a 91% purity, providing 1,036-fold enrichment.*

2.1.3 Conclusion

We demonstrated a new dielectrophoretic focusing integrated pulsed laser activated cell sorter (DEP-PLACS) featuring continuous, sheathless, size-independent, real-time tunable, 3D dielectrophoretic single stream focusing at high speed flows for high throughput and high purity sorting. By utilizing the extremely long (4 cm) DEP interaction channel and the rapid (~30 μs) fluid perturbation, 91% sorting purity has been achieved at a throughput of 1,500 particles/sec with polystyrene beads.

2.2 Heavily doped silicon electrode for dielectrophoresis in high conductivity media

2.2.1 Introduction

Dielectrophoresis (DEP) has been widely applied for manipulating, patterning, and sorting of biological cells[8], [31], bacteria[32], microparticles[7], [33], nanowires[34], [35] and liquid droplets[36]. Typically DEP manipulation of biological samples is conducted in low ionic buffers to enable cells to exhibit more distinctive dielectric properties and to minimize electrochemical reactions and Joule heating[37]. However, cells in low ionic media do not maintain normal metabolism functions as in regular physiological buffers, and cell viability can be significantly compromised over time[38], [39]. As a result, DEP manipulation of biological samples is considered less biocompatible than other mechanisms such as acoustic[40], [41] and magnetic[42], [43] manipulation.

There are several major challenges of performing dielectrophoresis in high conductivity buffers. First, electrochemical reactions such as electrolysis can be easily triggered at the edge of electrodes[44], [45]. Second, excessive heat generated due to high conductivity can be detrimental to biological sample as Joule heating is linearly proportional to the electrical conductivity of media

($\sim \sigma E^2$)[39]. In essence, both factors limit the maximum voltage that can be applied to electrodes for creating non-uniform electric fields for DEP manipulation. Additionally, most biological samples such as mammalian cells do not experience sufficient DEP force to be manipulable, stronger electric field strength is needed to enhance the force ($F \sim \nabla E^2$). Therefore, an approach allowing the increase of maximum voltage that can be applied to a DEP platform without triggering electrochemical reactions and reducing the heat generated can effectively increase DEP forces.

In conventional DEP devices, the creation of non-uniform electric field is realized by planar metal electrodes[38], [46]. At the edges of metal electrodes are regions of strongest electric fields due to the field crowding effect (Figure 2.13(a)). In high conductivity media, the electric double layer (EDL) at the edge could be quickly charged up (charging time $\sim RC$). This results in significant voltage drop at the liquid and electrode interface that leads to electrochemical reactions. Not only could the electrodes and samples be damaged but also could bubbles be induced to perturb or even block DEP operations[44], [45].

One way to minimize the EDL charging effect in high conductivity buffers is to operate at high a.c. frequencies, usually above MHz[8], [29]. However, even at such high frequencies, the threshold voltage for triggering electrochemical reactions at electrode edges is still not sufficiently high. Insulator DEP (iDEP) approaches have been proposed to suppress the electrochemical reactions by confining electric current pathways with patterned dielectric structures to generate non-uniform electric fields[47]–[49]. The strongest electric field regions in iDEP are near the patterned insulator structures instead of the electrode surface. One drawback is that most iDEP devices have electrodes separated by a long distance in order to prevent electrochemical reactions. This results in the need of using high voltage to provide adequate electric field strength to create

DEP force for effective manipulation. Voltages higher than 1 kV in iDEP devices are common[50], [51].

Here, we present a hemispherically shaped, heavily doped (N++) silicon electrode for DEP manipulation in high conductivity media (~ 1S/m). The media is 10~100 times more conductive than low ionic buffers commonly used in DEP. The structure of the proposed N++ silicon electrode is illustrated in Figure 2.13(b). On top of the hemispherical and heavily doped silicon, 1μm thick SiO_2 dielectric film confines the electric current pathways through a narrow opening to create non-uniform electric field maximized at the edges of the opening. As the equivalent circuit models show, on a conventional metal electrode, electrical currents from a broad range converge to the edge of the metal electrode, and the EDL at the edge is quickly charged up. Once the voltage drop at the interface exceeds a threshold value, electrochemical reactions occur. On a N++ electrode in comparison, the strongest electric field region is near the dielectric opening, similar to that in iDEP. The hemispherically shaped electrode provides a larger interface capacitance and a longer RC charging time, which effectively suppresses electrochemical reactions and allows a higher threshold voltage. N++ electrode does not require high voltage at the interface to provide enough electric field strength, as in the case of iDEP, because it does not rely on long electrode separation distance to prevent electrochemical reactions. In addition, single crystalline silicon is an excellent heat conductor for thermal dissipation during DEP manipulation in high conductivity media. The 3D bulk silicon electrode also provides low electrical resistance for massively parallel manipulation across a large area without losing voltage and power along long transmission lines. The use of N++ electrodes for DEP manipulation is similar to that of conventional metal electrodes but with higher threshold voltage.
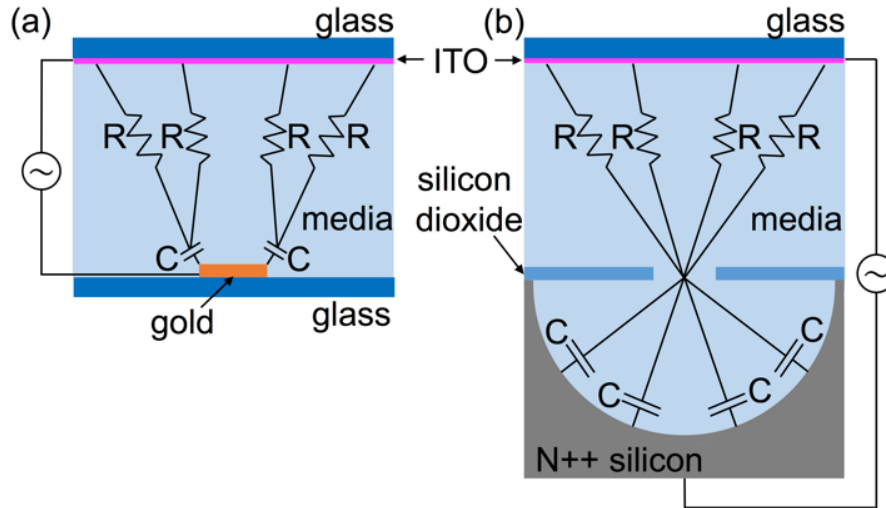
Figure 2.13 Schematics of the equivalent circuit models. *(a) conventional metal electrode, and (b) hemispherical shape N++ silicon electrode for DEP manipulation.*

2.2.2 Results

The fabrication process of N++ electrodes (Figure 2.14(a-d)) is simple. A commercially available heavily doped n-type silicon wafer with 1μm thermal dioxide grown on both sides was used. The first step involves removing the backside oxide by reactive ion etching (STS Advanced Oxide Etcher) to allow electrical connection to the back surface. Next, the frontside oxide was patterned to form desired shapes of openings. Finally, XeF_2 gas was introduced for isotropic undercut etching to create the hemispherically shaped N++ silicon electrodes. An example of a 2D array N++ electrodes with $3\ \mu$m oxide openings are shown in Figure 2.14(e).
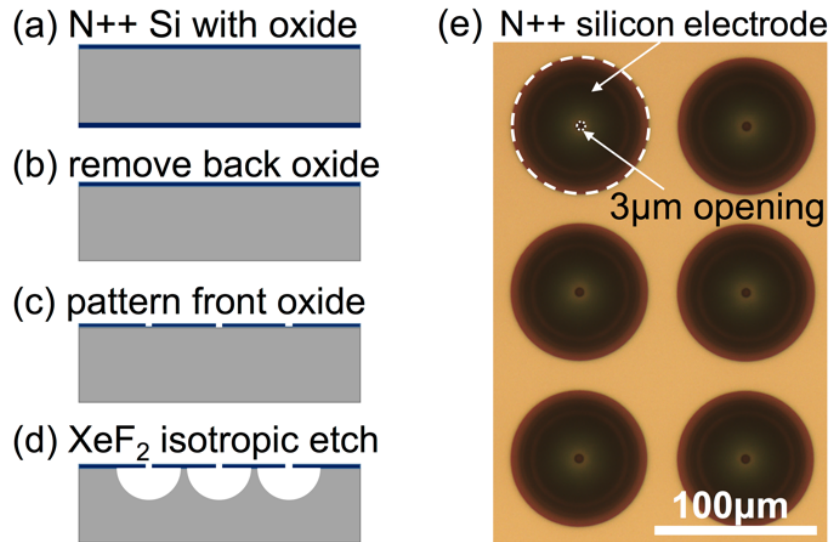
Figure 2.14 Process flow for fabricating N++ silicon electrodes. (a) A commercially available heavily doped n-type silicon wafer with 1μm thermal oxide films grown on both sides. (b) Back side oxide was removed by reactive ion etching to provide electric contact. (c) Front side oxide was patterned and etched to create openings. (d) XeF₂ gas was introduced to etch out the hemispherical shape N++ Si electrodes. (e) A 2D array of N++ electrodes with 3μm oxide openings.

Figure 2.15 shows the comparison of numerically simulated electric field distributions in three types of electrodes: conventional metal electrode, N++ electrode without undercut, and N++ electrode with hemispherically shaped undercut. A $10V_{p-p}$, 1MHz a.c. signal is applied between the top and bottom electrodes in all cases. Electric field strength distribution is extracted at 1μm above the surface of dielectric layer (white dashed lines). As shown in Figure 2.15(d), N++ electrode with undercut has comparable electric field strength to that of the metal line electrode. Since DEP force is proportional to the gradient of electric field intensity (E^2), the locations where maximum DEP forces occur for all three cases are near the edge of electrodes.
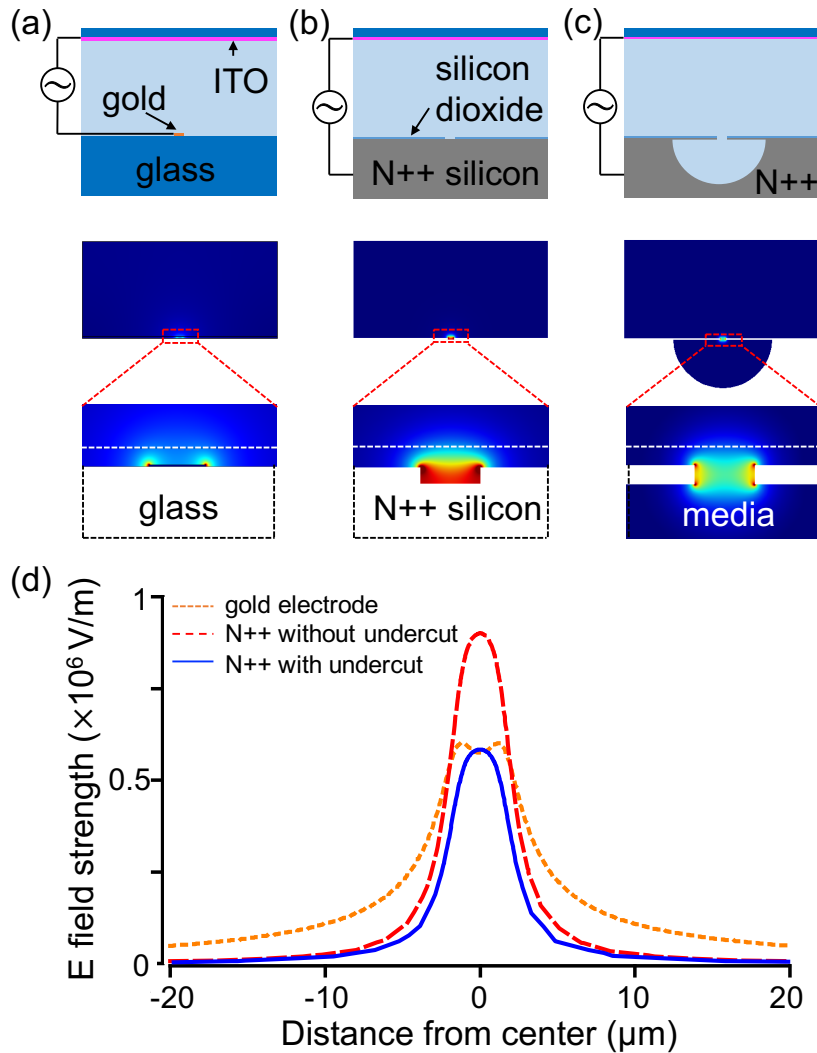
Figure 2.15 Numerically simulated electric field distributions *of (a) 3µm wide metal line electrode, (b) N++ Si electrode with a 3µm circular oxide opening but no silicon undercut and (c) N++ Si electrode with a 3µm circular oxide opening and 25µm in radius hemispherical silicon undercut. (d) E field strength distribution at 1µm above the dielectric surface.*

To compare the performance of N++ silicon electrodes and metal electrodes, we experimentally determined the highest voltage that each type of electrode can sustain in a high conductivity buffer (1× Phosphate-Buffered Saline, electrical conductivity ≈ 1S/m) without triggering electrolysis. The liquid layer is sandwiched between an ITO electrode and the test electrode with a 50μm thick spacer (double sided tape) in all cases. An a.c. signal is sent from a

function generator (Agilent, 33220A) through a power amplifier (ENI, Model 2100L) to the electrodes. During testing, voltages were gradually increased until the generation of bubbles was observed, which remarked the onset of electrolysis (Figure 2.16(a-f)). The corresponding threshold voltages at different frequencies were recorded and are compared in Figure 2.16(g). As illustrated, N++ silicon electrode with undercut can tolerate 3 times higher voltages than regular metal electrode. This corresponds to a 9-fold enhancement of DEP force, which is proportional to the square of electric field strength (E^2)[52], [53]. Note that the N++ electrode without undercut shows a threshold voltage similar to that of metal electrode. This proves that it is the large area effect from the hemispherically shaped undercut that primarily contributes to the increase of threshold voltage.
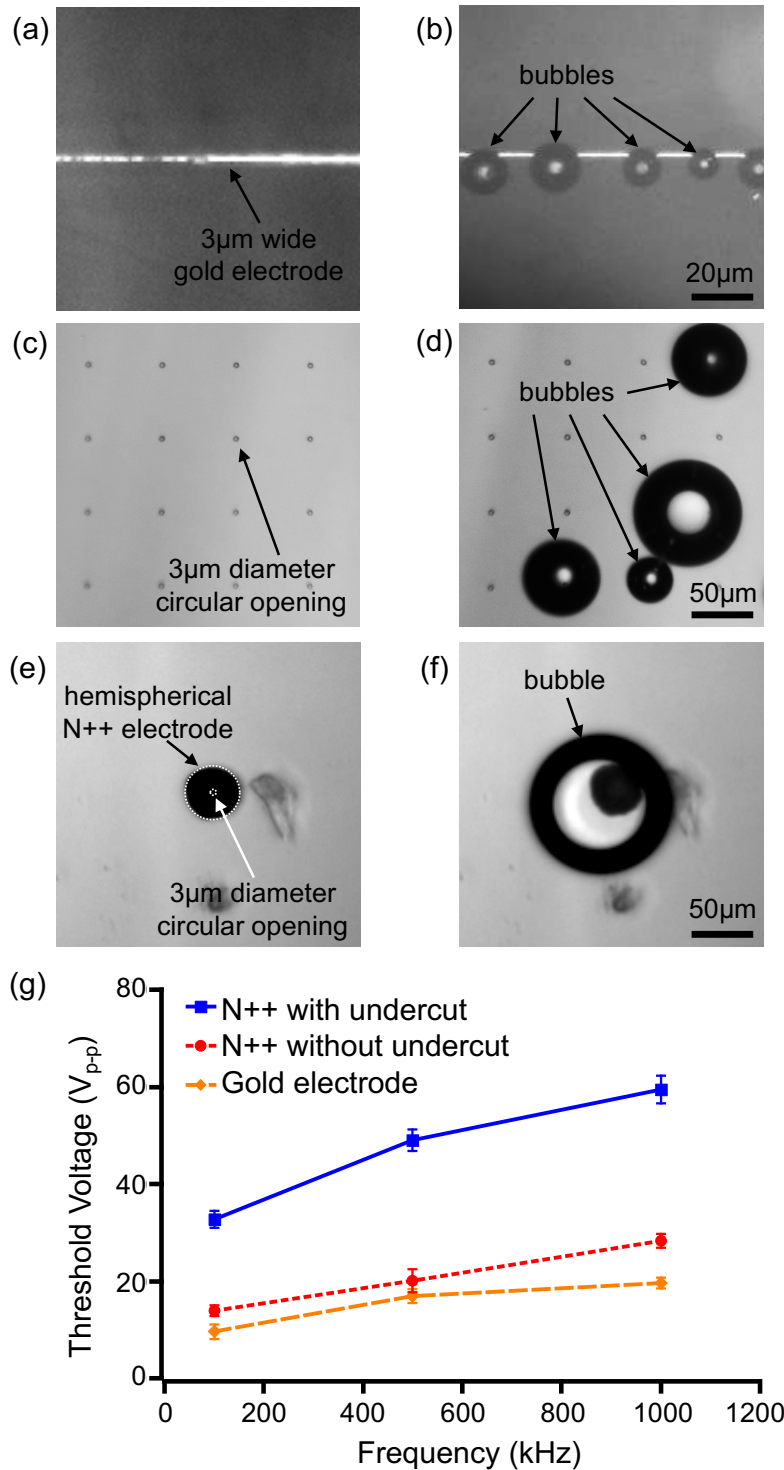
Figure 2.16 Onset of electrolysis. *Microscopic images of a gold line electrode (3 µm wide and 100 nm thick) (a,b), a N++ silicon electrode without undercut (c,d) and a N++ silicon electrode with undercut (e,f) before and after electrolysis. (g) Recorded threshold voltages for three devices at different frequencies. The threshold voltage for N++ electrode with undercut is 3 times higher than metal*

electrode. N++ electrode without undercut shows a slightly higher threshold than metal electrode.

To further demonstrate the capability of using N++ electrodes for DEP operation in high conductivity buffers, an array of line-shaped opening was patterned and etched, which created an elliptical shape silicon undercut. We tested DEP focusing of 10μm green fluorescent polystyrene beads (Fluoro-Max G1000) and GFP HeLa cells in 1× PBS. Buffer solutions containing beads/cells were introduced into a microfluidic chamber by a syringe pump (KD Scientific, 780100) at a flow rate of 0.08ml/hr. Without voltage application, beads/cells flew randomly through the chamber as shown by the stacked fluorescent traces. When an a.c. signal of $35V_{p\text{-}p}$, 1MHz was applied between the top ITO electrode and bottom N++ silicon electrodes, these particles experienced negative DEP forces and focused into narrow traces.
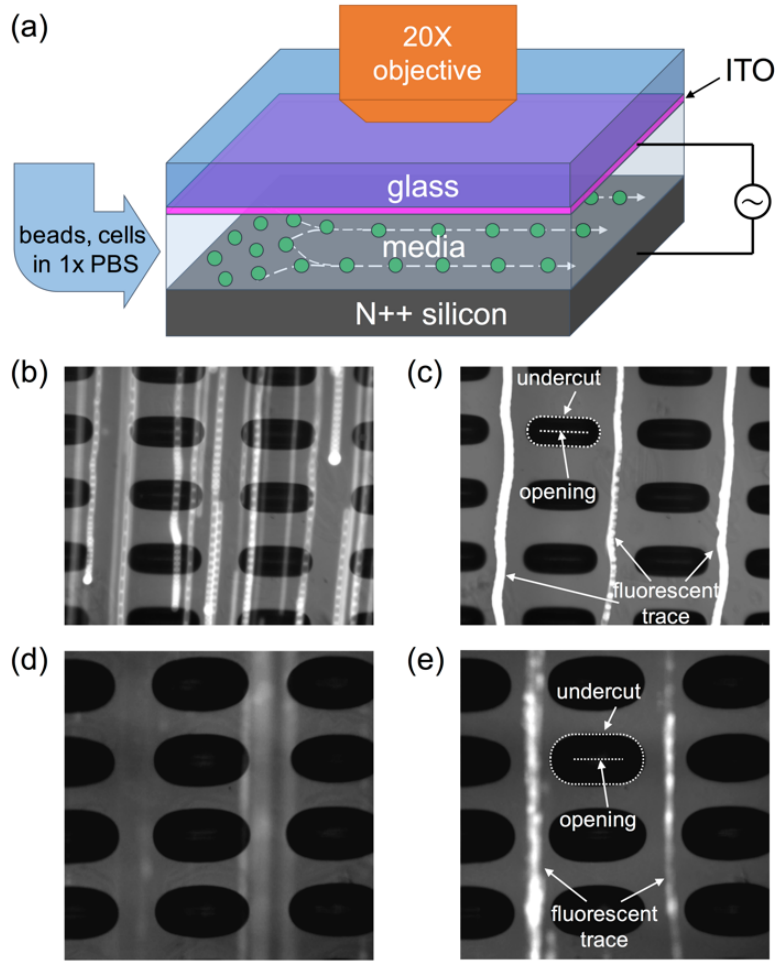
Figure 2.17 DEP manipulation. *(a) Schematic of DEP manipulation experiments, and captured fluorescent traces of particles by stacking multiple exposures of (b) 10µm polystyrene beads, no voltage; (c) 10µm polystyrene beads 35V$_{p-p}$, 1MHz; (d) GFP-HeLa cells, no voltage; (e) GFP-HeLa cells, 35V$_{p-p}$, 1MHz.*

In addition to the advantage of higher threshold voltages for DEP manipulation in high conductivity media, N++ silicon has several other advantageous features. First, the silicon substrate has excellent thermal conduction property. Heat generated from Joule heating in high conductivity media can be dissipated quickly. This feature has been confirmed by other prior works that utilize silicon substrates with patterned metal electrodes for DEP manipulation in high conductivity media[8], [54], [55].

Second, N++ electrode is a bulk electrode. The electrical current supplied to power the DEP operation is through the whole back side surface and flow in the direction normal to the wafer surface. The electrical impedance of a N++ electrode is extremely low, which is ideal for parallel DEP manipulation across the entire chip area, especially in high conductivity media. In conventional thin film metal electrode, the electrode impedance issue becomes severe for DEP operation in high conductivity media across a large area. For reference, a 100nm thick gold electrode layer ($\varrho=2.44\times10^{-8}\Omega\cdot m$) has a sheet resistance of 0.244Ω/sq, while a $50\mu m$ tall, $1cm^2$ area liquid chamber filled with a high conductivity medium (1S/m) has a resistance of 0.5Ω from top to bottom. The comparable value between the gold electrode's sheet resistance and the liquid medium's resistance implies that a significant portion of the applied voltage drops across the electrode and not in the liquid layer for DEP operation. This situation worsens for cases using long and narrow strip electrodes, common in most DEP devices. On the contrary, a $500\mu m$ thick bulk N++ electrode ($\varrho=0.003\Omega\cdot cm$) with a device area of $1cm^2$ has a through-wafer resistance of only 1.5×10^{-4} Ω, making it ideal for powering devices in high conductivity media across a large area.

In addition, the thermal oxide interface of the N++ electrode offers good bonding properties with other commonly used materials in electronics and microfluidics, thus broadening its applications through integration with other modules[56], [57]. The fabrication of N++ electrode is also simple, and requires only one photolithographic patterning and two etching steps from a commercially available heavily doped substrate. This eliminates the step of metal deposition needed for fabricating the conventional metal electrode[45].

2.2.3 Conclusion

To conclude, we have demonstrated a novel N++ silicon electrode for DEP manipulation in media with high electrical conductivity and high ionic strength. Comparing to the conventional metal electrode, it increases the operational threshold voltage in high conductivity buffers by 3 times and results in a 9-fold enhancement of maximum DEP force without inducing electrolysis. In addition, it provides several advantageous features such as excellent heat transfer property, low electrical input impedance, easy manufacturing process, and friendly interface for integration with other electronics and microfluidics components for broad applications.

2.3 Lift-off cell lithography for cell patterning with clean background

2.3.1 Introduction

High-throughput cell patterning is an important technique for many cytobiological studies and for tissue engineering[58]–[60]. Much effort has been expended developing efficient and reproducible strategies for cell patterning[61], [62]. Prior studies include active methods that utilize physical phenomena such as dielectrophoresis (DEP)[63]–[65], optoelectronic tweezers (OET)[7], [8], [66], [67], and magnetic[68], [69] or acoustical forces[70], [71]. Passive approaches include cell trapping in a microwell[72], [73] and surface chemical modifications via selective plasma treatment[74], [75], UV light[76], [77], micro-contact printing (μCP)[78]–[80] and photolithography-based techniques[81]–[83]. These passive approaches require less specialized equipment and are therefore more practical and user-friendly for typical biology laboratories. However, it still remains challenging to achieve well-defined cell patterning with good pattern filling efficiencies at desired locations and with few cells at unwanted locations across a large surface area[84]–[86].

Advances in microfabrication technique applications beyond microelectronics have generated opportunities for studies in biology[87], [88]. Lift-off lithography is a traditional wafer-level microfabrication method that can rapidly generate massive array patterns at high resolution for a target material, such as metals[89]. Previously reported micro-stencil methods employed a similar lift-off lithography concept for creating cell patterns[79], [90]. However, micro-stencils are usually fragile freestanding thin membranes that require delicate handling; therefore, they have not been widely used[91]. Here, we demonstrate a novel and simple cell patterning method called Lift-off Cell Lithography (LCL) that utilizes a fully biocompatible process to achieve high efficiency patterning with nearly zero background defects in masked or blocked areas of a surface. A thin film stacked with SU-8 photoresist and water-soluble polyvinyl alcohol (PVA) was used as a sacrificial layer to lift-off un-patterned cells deposited on the substrate. The substrate was precoated with poly-L-lysine (PLL) to anchor cells at the desired locations. Using LCL, we have achieved over 70% cell patterning efficiency for both adherent and non-adherent cells in the target patterned area, with < 1% defect rate in the blocked area.

2.3.2 Results

The major steps of the fabrication process and experimental protocol for patterning cells using LCL are shown in Figure 2.18. First, a glass coverslip (2.2×2.2 cm^2) is cleaned with 70% ethanol for surface sterilization followed by coating with a poly-L-lysine-FITC labelled solution (Sigma; 0.1 mg mL^{-1}) for 30 minutes at room temperature. PLL is a positively charged cationic polymer that promotes cell adhesion through electrostatic attraction since the plasma cell membrane is negatively charged. Then, an aqueous solution containing 4% (w/w) PVA (Sigma) is spin-coated at 1,000 rpm onto the surface as a sacrificial layer. Next, SU-8 3005 photoresist

(MicroChem) is spun onto surface at 3,000 rpm to produce a 5 μm thin film that is then micro-patterned via standard photolithography. Afterwards, an oxygen plasma treatment (Technics Micro RIE 800, 200 W, 300 mTorr) is performed for 2 minutes to etch the exposed PVA. The final fabrication step involves coating the chip with PLL for a second time for another 10 minutes at room temperature in case the first layer PLL is partially etched away by the oxygen plasma in the previous step.
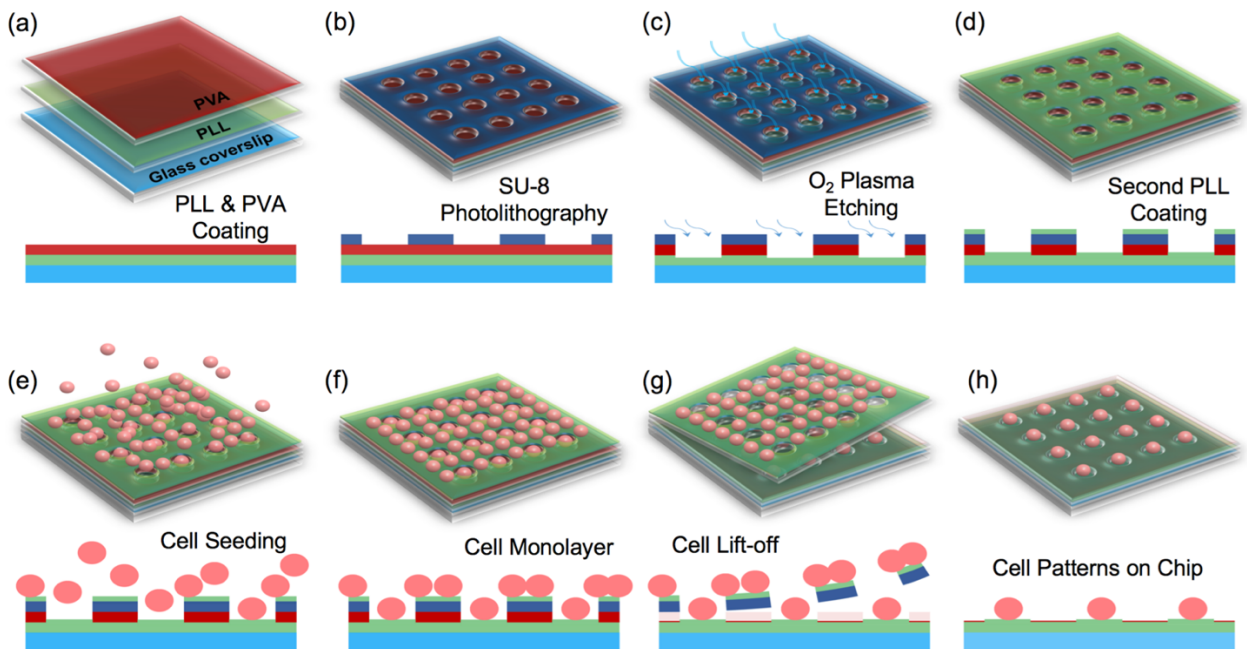
Figure 2.18 Illustration of the process flow for the Lift-off Cell Lithography (LCL) patterning method. *(a) Multilayers (including PLL and PVA) are coated in sequence on a glass coverslip. (b) SU-8 3005 photoresist is patterned on top of the surface via photolithography. (c) PVA layer is further patterned by O_2 plasma etching. (d) PLL is coated for the second time. (e) Cell suspension medium is loaded on the chip for 10 min at room temperature. (f) A monolayer of cells eventually forms. (g) Cells are further cultured for another 30 min in incubator while PVA gradually dissolves and allows cells adhering on the SU-8 film to be peeled off. (h) The patterned array of cells.*

After rinsing and drying the glass substrate, non-adherent Ramos cells suspended in tissue culture medium at a high density of 3.0×10^6 cells mL^{-1} are dispensed onto the substrate for 10

minutes at room temperature where a cell monolayer eventually forms. Ramos suspension cells are free floating in culture media containing RPMI-1640 supplemented with 10% fetal bovine serum and are difficult to attach to the bottom substrate. Serum-free RPMI 1640 medium is found to improve cell adhesion to the glass substrate, possibly due to charged interactions between the hydroxyl groups on the substrate and integrins expressed on the surface of cells[92]–[94]. Our testing also confirms that we can increase the number of surface-attached Ramos cells by about ten-fold with the serum-free culture medium (Figure 2.19). PVA is a water-soluble material with good biocompatibility. The dissolution rate increases with temperature and usually cells do not adhere well to PVA[95], [96]. After cell seeding, the substrate is kept in an incubator at 37°C under a 5% CO_2 humidified atmosphere for another 30 minutes, resulting in the partial removal of the PVA layer underneath the SU-8 film. The continuous SU-8 membrane is thin but rigid enough to be peeled-off together with all the cells adhering to it (Figure 2.20). This leaves only cells at the desired exposed pattern locations. Since a high concentration of cells can be used in the patterning process of LCL without concerns for background defects, high cell fill-up efficiency and clean background patterning can be achieved at the same time without any trade-off. By contrast, this trade-off often needs to be made in other patterning approaches.

33
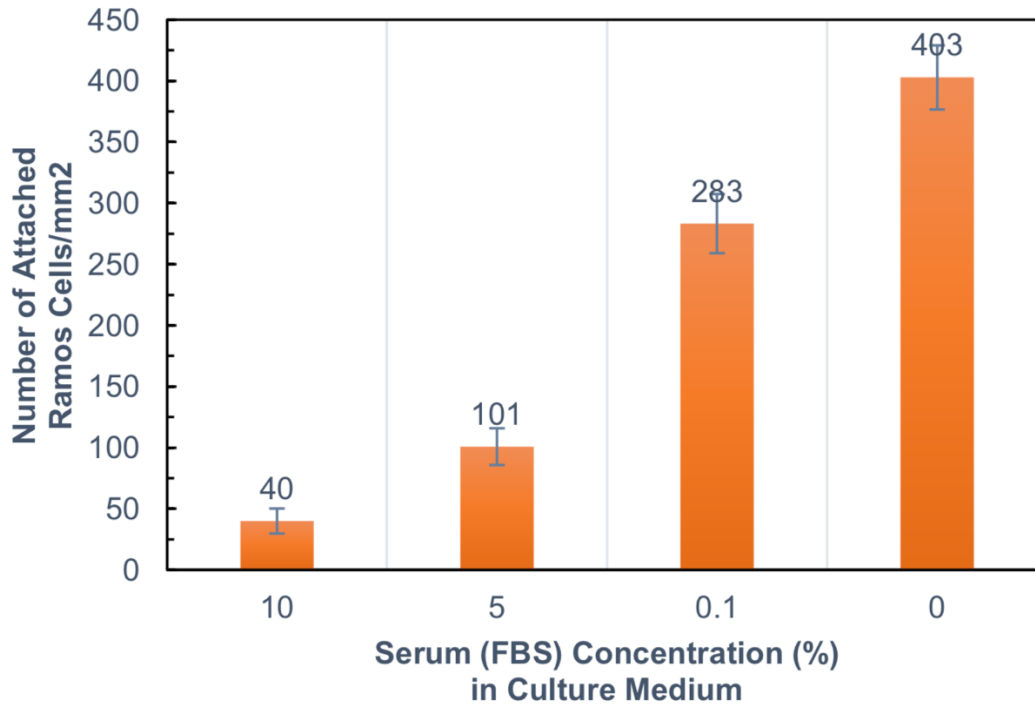
Figure 2.19 Suspension cell attachment. *Attachment of Ramos cells per mm^2 on coverslips in the culture media containing different serum (FBS) concentrations at 10% (regular), 5%, 0.1% and 0, respectively, after 30 minutes. Error bars denote standard deviation of the average value.*
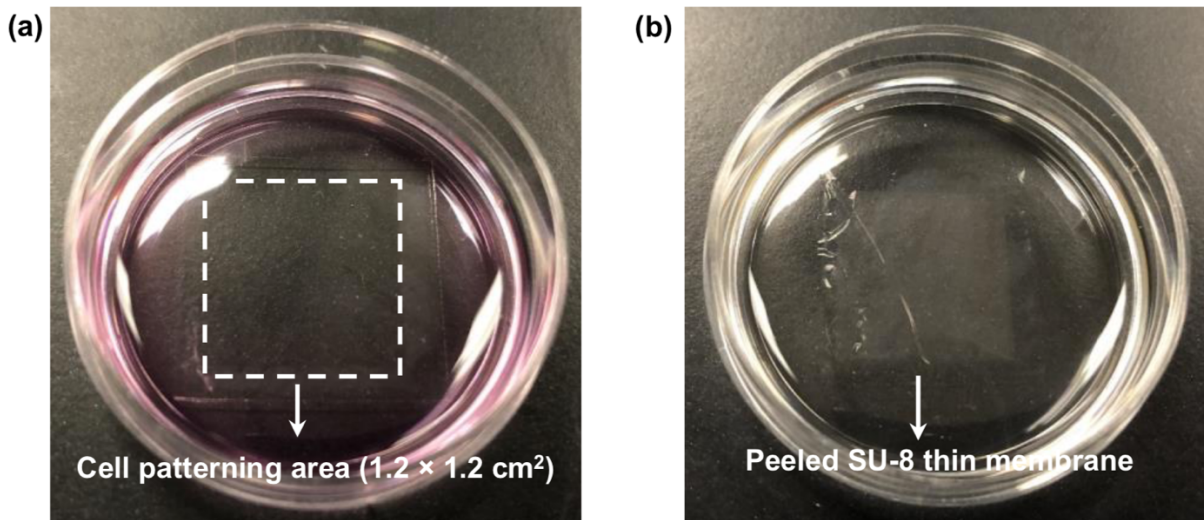
Figure 2.20 SU-8 lift-off. *Pictures of (a) fabricated substrate with cells seeding across a large patterning area, and (b) intact peeled SU-8 thin membrane with cells after cell lift-off.*

An array of circular holes, each with a diameter of 20 μm and a center-to-center spacing of 50 μm, repeated over a large 1.2 × 1.2 cm² area (Figure 2.23a) was used to pattern a Ramos B cell array through LCL (Figure 2.23b). Calcein AM/propidium iodide (Invitrogen) staining is used for live versus dead cell recognition at 1h after cell patterning. LCL shows minimal impact on cell viability (Figure 2.21).
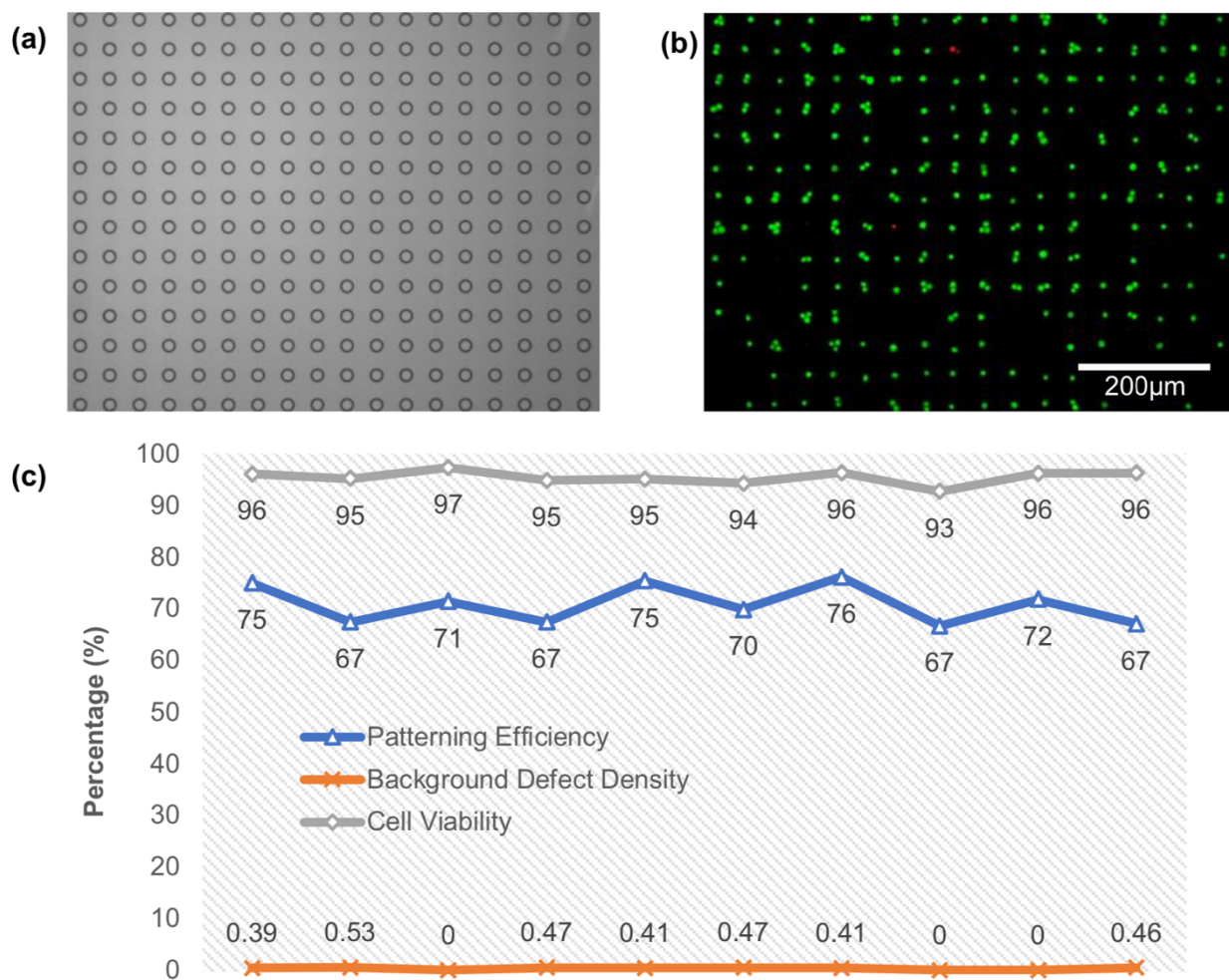
Figure 2.21 Patterning efficiency. *(a) Microscopic images of fabricated SU-8 microwells before experiment; (b) a representative fluorescent microscopic image of Ramos cells stained by Calcein AM/PI after lift-off under 10× objective; (c) recorded data from 10 random selected locations on the chip after lift-off to estimate the patterning performance.*

Patterning experiments were repeated multiple times. The number of total spots, spots occupied by cells, cells in the masked background, and the total number of cells were recorded from randomly selected locations on each chip and this data was used to estimate the average values of patterning efficiency and background defect rate. The patterning efficiency is defined as the percentage of spots occupied by cells, and the background defect rate is defined as the number of cells in undesired positions divided by the total number of cells. Figure 2.23c shows that LCL can achieve a peak 71% patterning efficiency with a background defect rate as low as 0.31%. For comparison, two other widely used surface chemical treatment approaches, namely micro-contact printing (μCP) and lift-off PLL (LPLL), have also been tested to pattern Ramos cells under the same conditions (Figure 2.22).
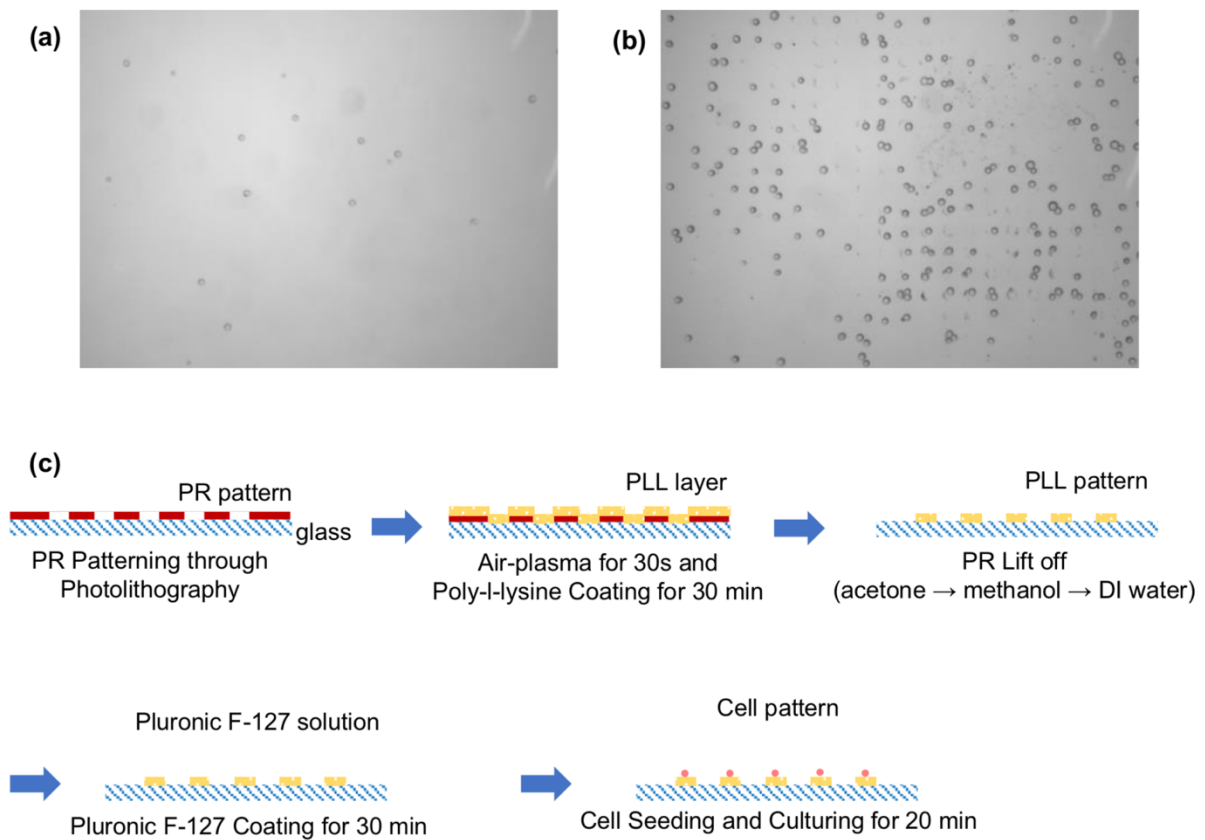
Figure 2.22 Comparison of Ramos cell array patterning produced by (a) μCP and (b) LPLL; (c) the process of LPLL.

μCP shows no significant effect on non-adherent cell patterning with a low efficiency and high defect rate, and LPLL results in an improved patterning efficiency, however, with the background defect rate an order of magnitude higher than our LCL method (Figure 2.23c). With LCL, optimized single-cell array patterning is also possible by reducing the hole diameter further, making it wide enough for one individual cell but not wide enough for multiple cells[84]. The tradeoff is a slightly lower patterning efficiency. In addition, the LCL technique is also effective for patterning cells to form arbitrary shapes. As demonstrated in Figure 2.23d, cells can be arranged into alphanumeric shapes from "1" to "9" with a clean background.
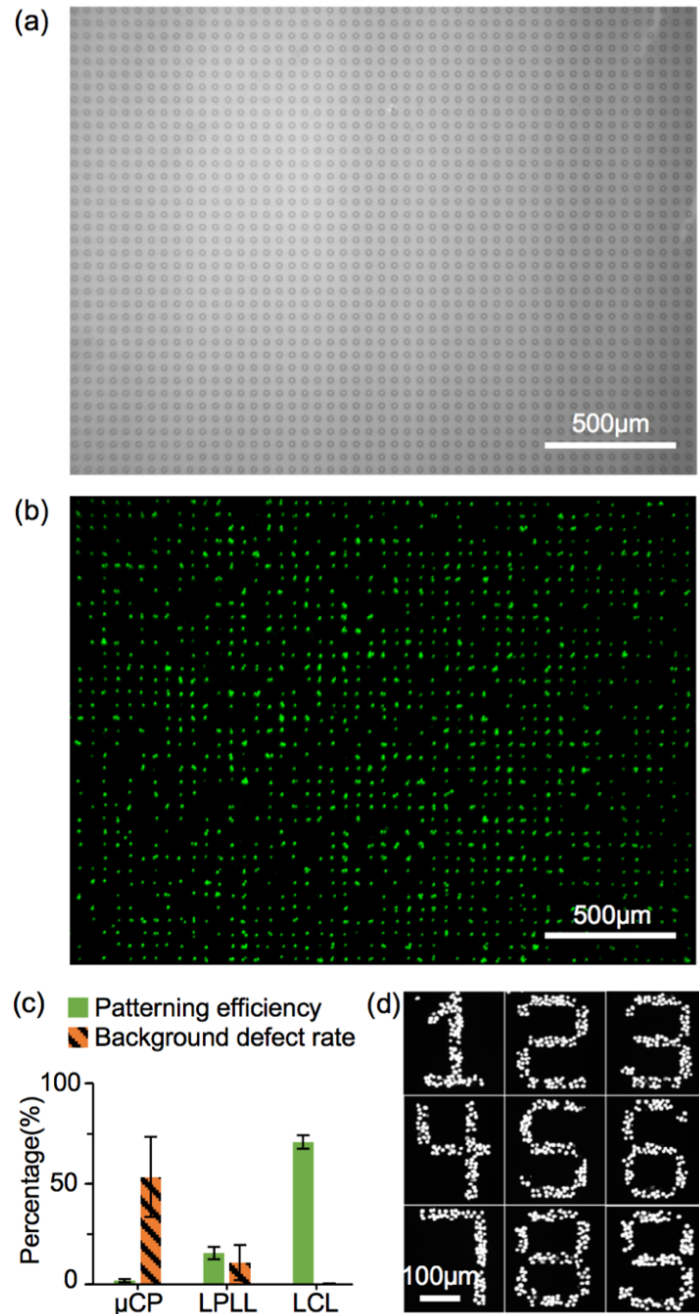
Figure 2.23 Non-adherent Ramos cell patterning through LCL. *(a) Image of a SU-8 microwell array with 20 µm diameter holes. (b) Fluorescence image of patterned cells stained with calcein AM. (c) Results of cell patterning efficiency and background defect rate via µCP, LPLL and LCL. (d) Fluorescence image of cells patterned to form number characters from "1" to "9".*

LCL also works well with adherent cells (Figure 2.24a and b). In order to pattern HeLa cervical carcinoma cells whose average size is larger than Ramos B cells, the circular hole size on LCL is increased to 30 μm. The second PLL coating step is also skipped to prevent HeLa cells from adhering tightly to the PLL-coated SU-8 sidewall, which can result in unexpected removal of cells from desired locations during peel-off.
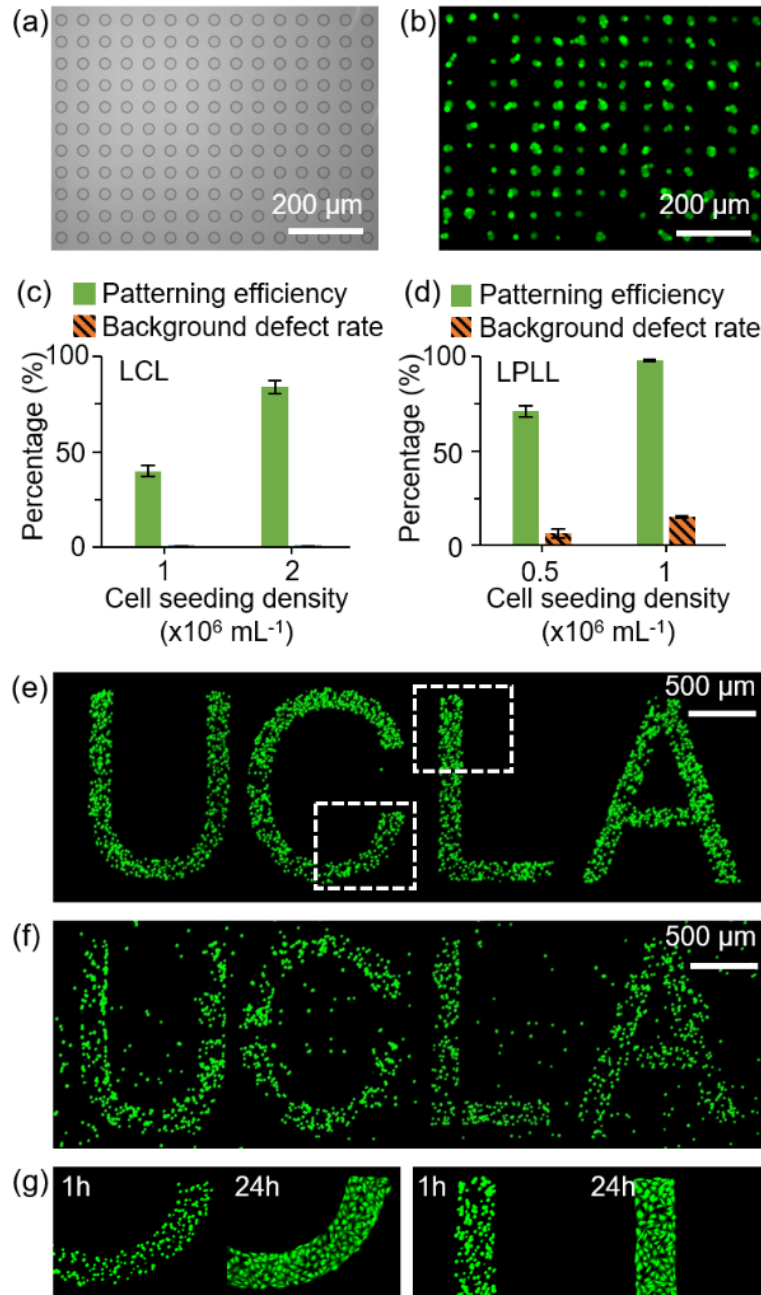
Figure 2.24 Adherent HeLa cell patterning through LCL. *(a) Image of SU-8 microwell array with a diameter of 30 µm on the chip. (b) Fluorescence image of cell array patterning stained with calcein AM. (c) & (d) Results of cell patterning efficiency and background defect rate via LCL and LPLL, respectively, with different cell seeding densities. (e) & (f) Fluorescence images of large-scale cell patterns arranged in the letters of "UCLA" by LPLL and LCL, respectively. (g) Fluorescence images of patterned cells marked in the white dashed boxes in (e), after culturing for 1h and 24h.*

In LCL, high cell patterning efficiencies can be achieved with higher cell seeding densities and no significant increases in background defect rates (Figure 2.24c). This is a unique feature of LCL that differs from traditional surface chemical modification approaches, in which a higher cell seeding density usually adversely results in a corresponding higher background defect rate (Figure 2.24d).

Using LCL, large-scale custom arrays of HeLa cells can also be patterned. As demonstrated in Figure 2.24e, cells can be patterned into the letters of "UCLA" with nearly zero defects in the background. By comparison, Figure 2.24f shows the result of cell patterning via the LPLL method with many cells outside of the desired patterning areas. In Figure 2.24g, the magnified regions exhibit normal cell attachment and proliferation at 1 hour and 24 hours, respectively, after LCL. Since there is undissolved PVA residue in the background, its anti-adhesion property helps to form sharp and well-defined pattern edges as well as clean un-patterned surroundings. The cells can keep growing for days within the defined areas until the PVA dissolves completely, after which patterned cells gradually spread out of the pattern boundaries (Figure 2.25).
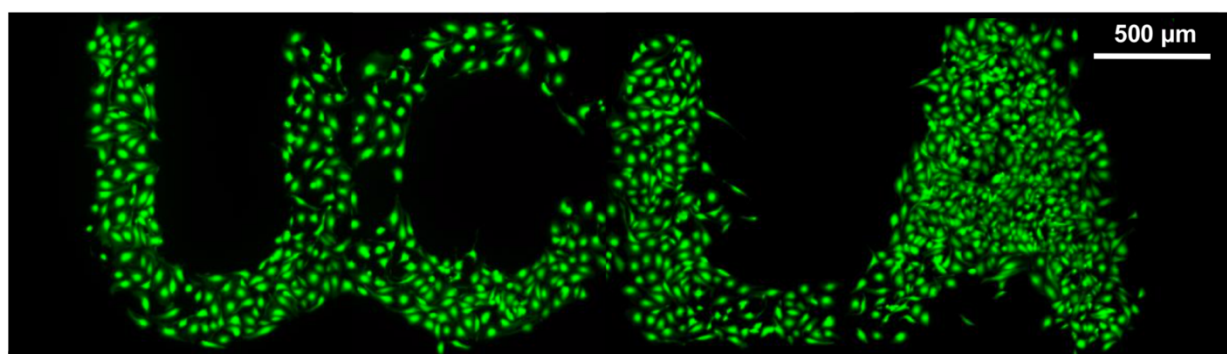
Figure 2.25 Fluorescent images of HeLa cell patterned into letters of "UCLA" via LCL after culturing for three days. Cells can grow beyond boundaries and different regions start to merge after the surrounding PVA residue completely dissolves in culture medium. This image is created by stitching four images of each letter taken under 4× objective lens to present images over a large area.

41

2.3.3 Conclusion

In conclusion, our LCL technique can produce high-throughput and high-efficiency cell patterning across a 1.2×1.2 cm^2 area. A bilayer stack of SU-8 and PVA is used as a sacrificial layer to remove cells deposited at un-patterned locations to realize cell patterning with a low background defect rate. The whole process is biocompatible and easy-to-fabricate. Using LCL, over 70% cell patterning efficiency with a nearly zero background defect rate has been achieved for both adherent and non-adherent cells. This approach can also be applied for patterning cells into arbitrary shapes with clean surroundings on large scales. Therefore, the LCL technique has potential for wide use in cell biology and related fields.

Chapter 3 Optofluidic Platforms for Nanomechanical Measurement

3.1 Parallel nanomechanical indentation platform using quantitative phase imaging

3.1.1 Introduction

Mechanobiology has been an emerging cross-disciplinary field that studies the mechanical properties of cells and tissues and how physical forces can contribute to the changes in biological events such as cell differentiation and disease development. Over the past years several tools and approaches have been developed for quantifying mechanical properties of biological samples. Atomic force microscopy (AFM) provides highly sensitive and accurate cell deformation measurements at sub-cellular level. However, the throughput is low and obtaining statistically significant data can be difficult[11]. Traction force microscopy (TFM) quantifies forces exerted by cells on top of a gel substrate through tracking movements of embedded nanoparticles[97]. Elastic pillars (EP) measure traction forces by optically quantifying the deflections of pillar tips[98]. Yet, both TFM and EP platforms reveal mechanical responses mostly in the lateral direction. It remains difficult with current technologies to capture comprehensive cellular mechanical responses.

Here, we demonstrate a parallel nanomechanical indentation platform using quantitative phase imaging to accurately track the vertical and lateral displacements of a large array of flat and rigid silicon micro-mirrors transfer-printed onto the surface of a transparent elastic polymer film (Figure 3.1). Local deformation in the polymer substrate is detected by the change of optical path length in reflected light from individual micro-mirrors. With known elastic modulus of the soft

43

polymer substrate, local indentation forces, traction forces and rotational torques applied on these mirrors can be quantified at the same time.
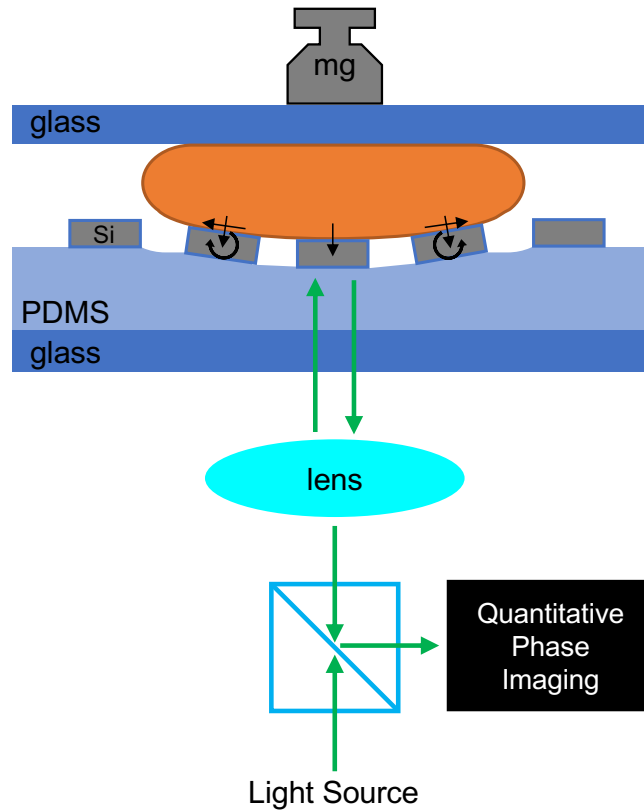
Figure 3.1 Schematic of a parallel nanomechanical indentation platform using quantitative phase imaging.

3.1.2 Design and fabrication

The fabrication process flow is shown in Figure 3.2a-g. A silicon-on-oxide (SOI) wafer with device thickness of 10 μm is patterned by reactive ion etching (RIE) into the device layer to create individual silicon disks. A thin protective SiO_2 layer on the sidewall is deposited by plasma enhanced chemical vapor deposition (PECVD). Timed anisotropic RIE etching is used to remove SiO_2 in the trench and expose the bottom silicon substrate for following isotropic undercut. After

carefully timed isotropic RIE undercut, silicon micro-mirrors are supported by tiny silicon posts underneath (Figure 3.2h). The chip goes through oxygen plasma surface treatment and then flipped to permanently bond with a PDMS substrate. Tiny silicon supports can be easily broken in ultrasound bath to release the silicon mirrors with good yield across a large area. Finally, the heterogeneously integrated device goes through a brief XeF_2 etching to clean out the silicon residue on top of mirrors. Figure 3.2i shows the bottom view through the glass and PDMS substrate of a fabricated device with a large array of highly reflective silicon micro-mirrors. The size of each micro-mirror is 20μm in diameter, and can be tailored for specific applications.
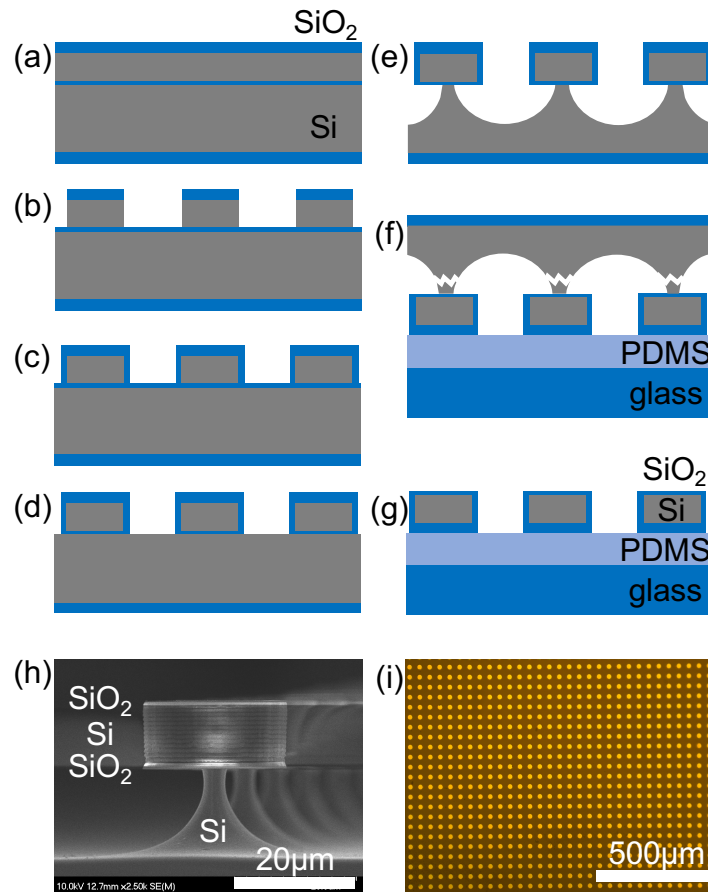
Figure 3.2 Process flow of transferring a micro-mirror array onto a PDMS substrate. *(a) SOI wafer, (b) pattern device silicon layer, (c) PECVD SiO_2 sidewall, (d) timed RIE etch to expose substrate silicon, (e) timed isotropic silicon undercut, (f) bonding with PDMS and ultrasound bath to break silicon supports, (g) XeF_2*

45

cleaning silicon residue. (h) SEM image of a single silicon mirror with isotropic undercut support. (i) Microscopic bottom view of large micro-mirror array.

3.1.3 Results

A blue LED is used as a light source to illuminate the micro-mirrors, with reflected light being imaged by a quantitative phase imaging sensor (Phasics SID 4 GE) mounted on an inverted microscope. A droplet of highly diluted 100μm polystyrene bead solution is dispensed on the device surface and air-dried to have a few beads sitting on the device. Then the device is covered with a thin glass slide. Raw image files are processed to extract optical path length reading from pixels corresponding to micro-mirrors located under the spherical micro-bead.

When imaging locations without beads under a 20× objective lens, uniform displacement reading confirms that the micro-mirrors are extremely flat (Figure 3.3a). When the bead is pressed against the PDMS layer by the loading weight of 1 gram on top, micro-mirrors under the bead move in the vertical and lateral direction and also tilt, revealing the deformation in the PDMS substrate (Figure 3.3b). With the increase of loading weight to 3 grams, PDMS deforms more and these micro-mirrors move even lower (Figure 3.3c). Every tilted micro-mirror shows only one linear slope through the entire mirror surface, confirming that all mirrors remain rigid and flat even when the surrounding PDMS material is severely deformed. With the knowledge of elastic properties of the PDMS substrate, the lateral displacement and average vertical displacement indicate respectively the shear force and total normal force applied to a micro-mirror. And the tilt angle of a mirror denotes the total mechanical torque applied on it.
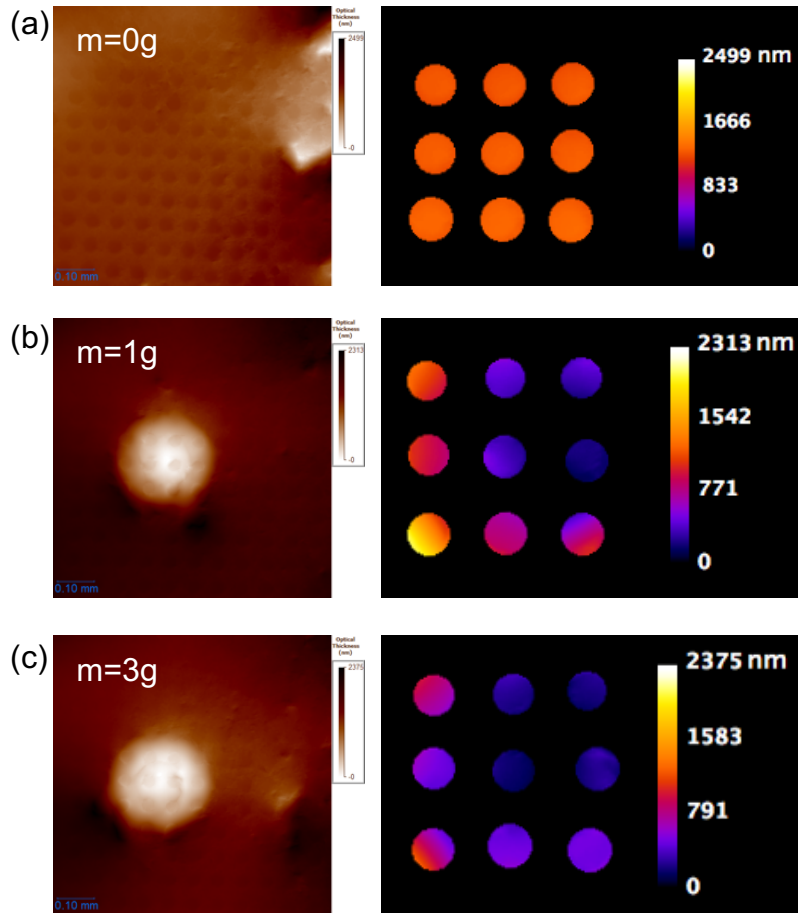
Figure 3.3 Raw and processed images *from quantitative phase imaging reveal the small vertical displacements and tilt angles of silicon mirrors when a bead is pressed by loading weight on top.*

3.1.4 Discussion

We demonstrated a parallel nanomechanical indentation platform using quantitative phase imaging to detect changes in optical path length of reflected light from rigid and flat silicon micro-mirrors. Accurate three-dimensional deformation in the polymer substrate can be obtained with each micro-mirror imaged by a few pixels. Local indentation forces, traction forces and rotational torques can be quantified at the same time.

Although the nano-scale displacement detection utilizing quantitative phase imaging sensor is a promising approach to realize nanomechanical indentation, apart from the micro-

47

fabricated device, the phase imaging sensor itself is an expensive and specialized equipment which may not be available to broader audience. Also because the phase imaging sensor is optimized for accurately sensing phase difference, it compromises in other aspects of imaging capability such as limited spatial resolution and sampling points, small sensor format, low acquisition and output frame rate. These limitations in imaging performance would be a road-blocker for future development of nanomechanical pressure/force sensing platforms for mechanobiology studies. On the other hand, the advancement of modern CMOS grayscale/RGB sensors has come a long way and excel in every aspect of imaging performance compared to the phase imaging sensor. It would be much more beneficial to integrate the nano displacement sensing capability into the micro-fabricated device, decouple and fully utilize the advancement of imaging performance from the development of modern CMOS/CCD image sensors, which are also more widely available to general users. In the next section, we present a micro-fabricated pressure sensing substrate by using colorimetric reflection from an array of optical micro-cavities, and demonstrate one of its potential applications to map the pressure distribution inside a complex microfluidic network. By proving this concept, we achieved a milestone in constructing a more capable platform for mechanobiology studies through the development of this large-scale parallel pressure/force sensing substrate. The remaining parts of the complete system would include a manipulation/pressing setup and a microscopic imaging system.

3.2 Microfluidic pressure distribution mapping using colorimetric interferometry

3.2.1 Introduction

Microfluidics has gained much attention since its emergence in the early 1980s and been widely used in both academic research studies and biotechnology industrial applications. The idea

of lab-on-a-chip technology is introduced to develop devices that integrate one or several laboratory functions, such as sample treatment and chemical detection, on a single chip to achieve automation and high-throughput processing[16], [99]. Key applications include DNA sequence analysis [100], [101], biomolecule synthesis [102], drug discovery [10], [103], [104], biological cellular studies [64], [105]–[110] and point-of-care disease diagnosis [111], [112]. With microfluidic manufacturing becoming more mature in the past years, highly integrated devices can be produced at low-cost [113], [114]. When the microfluidic network is scaled up, especially for systems involving pumps [115] and valves [116], [117], it's important to have a localized monitoring system to check the working condition. For large-scale continuous-flow systems it's crucial to monitor the flow condition in real time, because anomalies such as clogging [118], [119] and leakage [120] can be hard to track down but needed to be addressed promptly to ensure smooth operation. Hydraulic pressure, as one of the most essential parameters in fluid mechanics, is the driving force of fluid flow with an analogy to voltage driving an electric circuit [117]. Mapping of pressure distribution inside a continuously flowing microfluidic network is a good approach to monitor its operation status.

Traditional external pressure transducers are not very compatible with microfluidic systems since they are bulky and cannot provide localized pressure measurement [121]. The number of measurement spots, where we can connect the transducers to extract the local pressure information, is also limited [122], [123]. Several approaches have been proposed to develop more suitable microfluidic pressure sensors [124]–[129]. Electro-fluidic circuits [124], [126] and microflotronic films [125] measure local pressure by monitoring the electrical property change of ionic fluid resulted from pressure-induced channel geometric deformation. Their spatial resolution, however, is low due to the large footprint of a single sensing units. Optical imaging techniques are

49

also commonly used for flow observations. Monitoring the liquid-air [127] or liquid-liquid [128] interface locations provide a way of measuring pressure. However, these approaches require the modification of channel design and not are not always compatible with the operation of fluid network. Optofluidic membrane interferometer [129] is a novel image-based method that can measure the on-chip microfluidic pressure and flow rate simultaneously through monitoring the interference fringe patterns in an optical cavity. This approach, however, requires an image to have sufficient resolution in order to have enough quality to be matched with reference images, thus not easy for further miniaturization and limiting its spatial resolution.

Most of the optical imaging approaches, including the above-mentioned works, utilize the intensity profile of an image for measurement and hence often grayscale images are sufficient [130]. Yet, spectral or color profiles from optical measurements can also contain rich information but are rarely exploited. Here we present a pressure-sensing system using colorimetric interferometry that provides convenient and highly-customizable pressure mapping across a large area with high spatial resolution (Figure 3.4A). It can be easily integrated with arbitrarily-shaped microfluidic network with no modification to the original design and only requires only a simple optical microscope for measurement. Different levels of pressure are recognized by difference colors of reflection (Figure 3.4, B and C). Each pressure sensing unit is an optical cavity consisting of a thin air gap sandwiched between a rigid and transparent silicon dioxide disk suspended under a thin layer of poly(dimethylsiloxane) (PDMS) membrane and a silicon substrate. When the air gap thickness is changed due to the pressure applied on the PDMS membrane, the reflection color changes due to optical interference in the air cavity (Figure 3.4, D and E), which gives us the correlation relationship between pressure and reflection color. We demonstrate a potential utility

of this device by mapping the pressure inside a complex microfluidic network to monitor the flow condition at any location in this network.

(A)

(B)

(C)

(D)

(E)
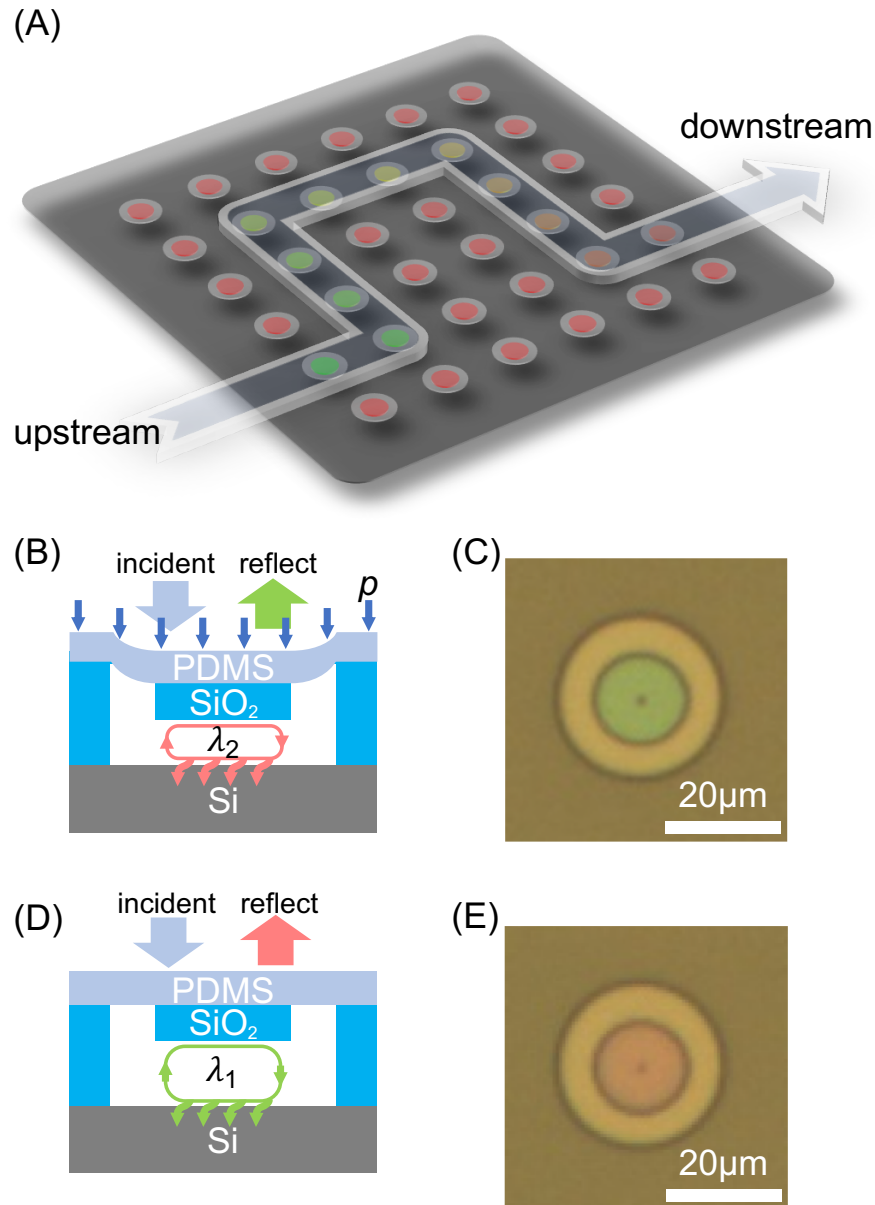
Figure 3.4 Pressure sensing using colorimetric interferometry. (A) Schematic of a pressure sensing substrate using colorimetric interferometry. Microfluidic pressure gradually decreases along the path of flow from upstream to downstream, corresponding to color transitions from green to yellow and to orange. (B) Cross-sectional schematic of the sensor unit under higher level of fluidic pressure at the upstream. The thin PDMS membrane is deformed, resulting in a smaller air gap between the SiO_2 disk and the Si substrate. Certain wavelengths of light (red) mostly transmit into the cavity due to interference at SiO_2/air interface and get partially

absorbed by silicon substrate, other wavelengths of light are mostly reflected from the SiO₂/air interface and form a complementary color (green) as shown in the microscopic image in (C). (D) At the downstream, on the contrary, the air gap remains almost the same due to much lower fluidic pressure. The wavelengths that enter the cavity and get absorbed by silicon (green) change, and the complementary color (red) that we observe under microscope also changes (E).

3.2.2 Results

3.2.2.1 Working principle

Numerical finite-difference time-domain (FDTD) simulation study is carried out for a single optical micro-cavity to show the reflectance spectra for visible light wavelength at different air gap thickness (Figure 3.6A). For light reflected at the SiO₂/air interface, no phase shift occurs because SiO₂ has a higher refractive index than air. At the air/Si interface, the reflected light needs to include an additional π phase shift.
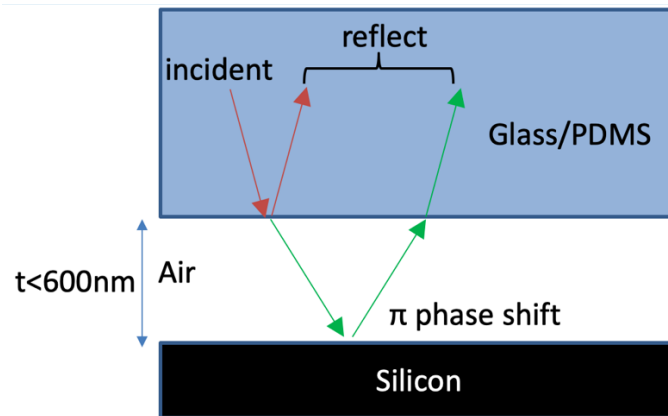
Figure 3.5 Design concept of the vertically interferometric optical cavity.

Consider these two reflected light waves at the SiO₂/air interface, the condition to form destructive interference is the following

$$2t = n\lambda, n = 1, 2, 3, \ldots$$

$$\lambda = 2t, t, \frac{2}{3}t, \ldots$$

52

where t is the thickness of air gap and λ is the wavelength of light. In order to shift the two reflected light waves by a phase π difference, the round-trip optical path length in the air gap needs to be integer multiples of wavelength. Majority light at these wavelengths has low reflection at the glass/air interface and enters the cavity. They bounce back and forth for multiple times and gradually get absorbed by the silicon substrate.

On the other hand, the condition for these two reflected light waves to form constructive interference is

$$2t = \left(n + \frac{1}{2}\right)\lambda, n = 0, 1, 2, \ldots$$

$$\lambda = 4t, \frac{4}{3}t, \frac{4}{5}t, \ldots$$

At these wavelengths the light gets reflected more and constitutes the final color captured by the camera. The colors of reflected light and absorbed light are complementary to each other. On our device, we design the initial air gap thickness t_0 to be slightly smaller than 600 nm, and limit the operation range to have the air gap no smaller than 300nm. Within the 600nm~300nm range, only one absorption peak shows up within the visible light spectrum from 380nm to 740nm. This design contributes to clear color transitions with good contrast when the air gap thickness changes. To maintain this operation range for good optical performance but accommodate for a larger or smaller pressure measurement range, we can change the thickness or elastic modulus [131], [132] of the thin PDMS layer. We selectively plotted the reflectance spectrum for three gaps at 500nm, 420nm and 360nm based on the FDTD simulation results (Figure 3.6B). Their absorption peaks are close to 500nm, 420nm and 720nm respectively, which agree well with our analysis.
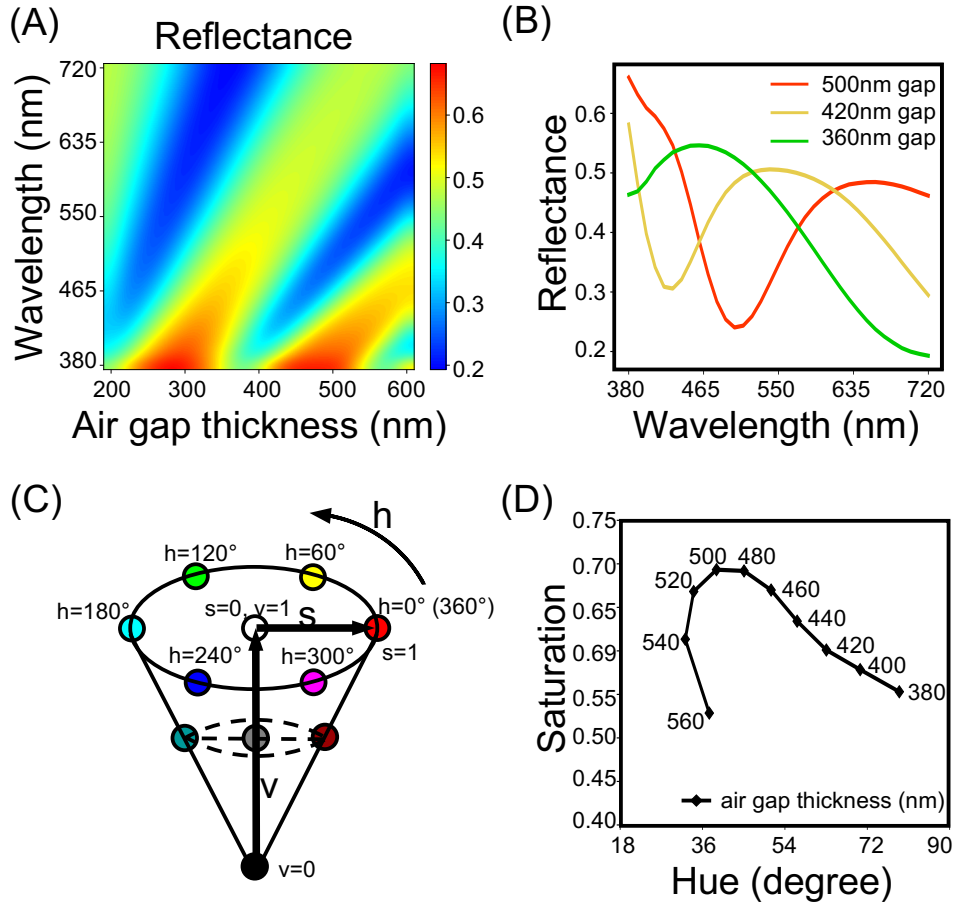
Figure 3.6 Working principal. *(A) Numerical simulation of reflectance spectra within visible light wavelength range as a function of different air gap thickness. (B) Numerical calculation of reflectance spectra at several selected air gap thickness. For each air gap we can clearly see an absorption peak at wavelength equal to or twice the thickness. Each spectrum line is plotted in the color we expect to see from reflection, which is complementary to the absorbed color. (C) Cone plot of HSV (Hue, Saturation and Value) color model. Different perceived colors (red, blue, green, etc.) are represented by different degrees of hue. Different levels of colorfulness are represented by saturation on a scale from 0 to 1. Value describes the brightness of a color relative to the brightness of a similarly illuminated white. (D) Plot of reflected colors in terms of their saturation and hue at different air gap thickness. Colors are calculated by integrating the product of light source intensity, device reflectance and camera pixel sensitivity over the range of visible light wavelength.*

The spectrum of reflective light can be affected by multiple factors inside an imaging system. We simplified the modeling by only considering the main factors to be illumination from

light source, reflection from our device and reception by the color image sensor. While the spectrum of reflected light is an objective physical property, the perception of color is subjective to the characteristics of the end observer [133], namely the color image sensor in our case. To compute the colors perceived by the color sensor from spectral data, we first adopt the RGB color model by calculating each component with the following set of equations

$$R = \int_0^\infty I(\lambda)S(\lambda)r(\lambda)d\lambda$$

$$G = \int_0^\infty I(\lambda)S(\lambda)g(\lambda)d\lambda$$

$$B = \int_0^\infty I(\lambda)S(\lambda)b(\lambda)d\lambda$$

where $I(\lambda)$ is the illumination spectrum of light source obtained by spectrometer measurement (Figure 3.13), and $S(\lambda)$ is the spectral reflectance of our device from numerical simulation. $r(\lambda), g(\lambda), b(\lambda)$ are the spectral sensitivities of red, green and blue pixels on the color image sensor as provided by the manufacturer (Figure 3.13). Due to the cut-off of light source intensity and color pixel spectral sensitivity outside of visible light wavelength, the integration over wavelength is effectively from 380nm to 720nm. As an approximation we sampled spectral data points at an interval of 20nm over wavelength for the three main factors of imaging system and calculated RGB intensities for colors perceived by image sensor at different air gap thickness. We observed that the transitions of red(R) and green(G) closely follow each other with a periodic pattern, which may require some technique similar to phase unwrapping to establish a relation between color and air gap thickness. Also noticed is the fact that even without spectral shift of these three main factors during imaging, the readings of RGB channels are subjected to scale simultaneously when the exposure conditions such as time and intensities fluctuate. Therefore, we

55

further resort to an alternative HSV (hue, saturation and value) color model that can decouple the brightness (value) attribute and retain the other color (hue and saturation) attributes (Figure 3.6C). In the HSV color model hue is the attribute of a visual sensation according to which an area appears to be similar to one of the perceived colors: red, yellow, green, and blue, or to a combination of two of them. Saturation is the colorfulness of a stimulus relative to its own brightness. Value is the brightness relative to the brightness of a similarly illuminated white [134]. As long as the exposure is within the range that no pixel reading is over-saturated, the color attributes provide a more robust measurement that are insensitive to exposure variation. The conversion from RGB color model to HSV color model can be done as follows

$$
H' = \begin{cases} (\dfrac{G-B}{max_{channel} - min_{channel}} + 0)/6; \, if \, max = R^* \\ (\dfrac{B-R}{max_{channel} - min_{channel}} + 2)/6; \, if max = G \\ (\dfrac{R-G}{max_{channel} - min_{channel}} + 4)/6; \, if max = B \end{cases}
$$

$$* \, if \, H' \, is \, less \, than \, 0 \, then \, add \, 1 \, to \, H'$$

$$H = H' \times 360°$$

$$S = \frac{max_{channel} - min_{channel}}{max_{channel}}$$

$$V = max_{channel}$$

After conversion to the HSV color model, we observed that the relative change of the value channel is much smaller than the hue or saturation channels. It corroborates our choice to only look at the hue and saturation attributes because the value attribute or the brightness is not as sensitive to the change of the air gap thickness. Then we visualize the numerical calculation results

by plotting out the air gap thickness with respect to saturation and hue values (Figure 3.6D). A clear trend of clockwise progression in hue and saturation readings is observed when the air gap thickness decreases from 560nm down to 380nm.

3.2.2.2 Pressure calibration

To validate the results from theoretical analysis and numerical calculations, we performed calibration experiments with a fabricated device under a typical microscopic setup (Figure 3.7A). A microfluidic channel is bonded on top of the device and is filled with water as the pressure-transmitting media. Pressure is supplied by a commercial precision pressure regulator with built-in digital readings as calibration source. The regulator is able to provide a stable pressure output with fluctuations less than 0.1 psi with feedback control. We sampled the pressure levels from 0 to 5 psi at an interval of 0.2 psi, and repeated measurements at each pressure level for 45 times. Images were captured using a color CMOS sensor at different pressure levels to demonstrate the color transition (Figure 3.7, BCD). We performed image processing to extract the hue and saturation readings from pixels corresponding to the silicon dioxide disk areas and averaged readings for each disk. The results of pressure levels up to 5psi are compiled into one plot (Figure 3.7E). The trend of hue and saturation transition with increasing pressure level resembles the one with decreasing gap spacing from numerical calculations (Figure 3.6D), where the difference can come from over simplification during modeling and analysis. With the experimental calibration data at our disposal, we now have a more consolidated and quantitative view of the color response of our device when subjected to externally applied pressure.
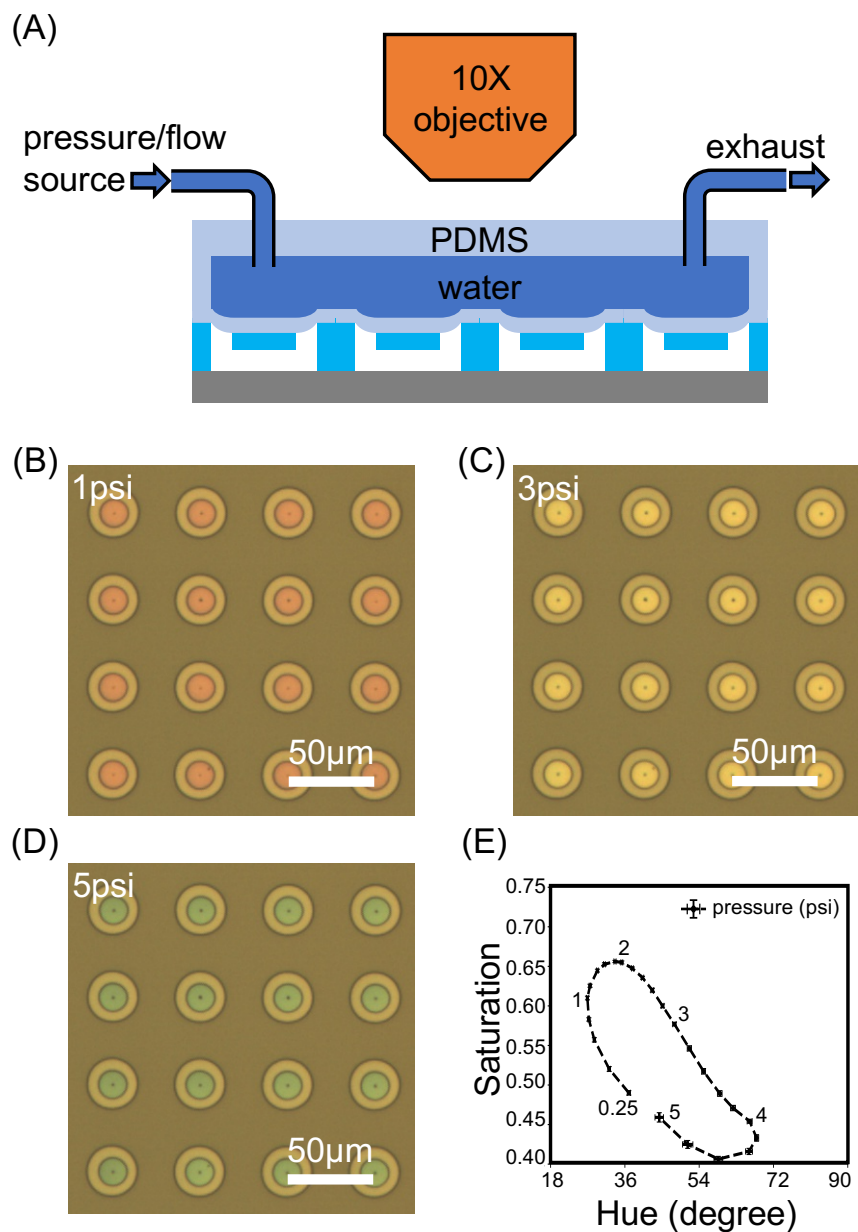
Figure 3.7 Pressure calibration. *(A) Schematic of experimental setup for calibrating color response. A microfluidic channel is bonded on top of our substrate to form a test device. The device is placed under a standard upright microscope with a 10× objective lens attached for imaging. Tubing connects the device with pressure-controlled or flow-rate-controlled source. For pressure calibration the exhaust outlet is sealed to form a closed chamber. (BCD) Microscopic images showing different colors captured by the camera at different pressure levels. (E) Experimentally measured colors at different pressure levels are plotted in terms of their saturation and hue. Each data point is plotted as an average of 45 individual measurements at each pressure level with error bars representing the standard deviation among 45 measurements.*

58

When a new measurement comes in during some future application, hue and saturation readings from the pixels can be extracted through image processing, and we are interested in knowing what pressure level these readings correspond to. In order to establish the correlation between hue and saturation readings and the actual pressure level, we can formulate the problem as multivariate nonlinear sensor calibration using the experimental calibration data (Figure 3.8A). A few statistical learning methods have been previously applied to such nonlinear sensor calibration problems [135]–[138]. Here we explore the applications of two models, polynomial regression and k-nearest neighbors (kNN) regression, to fit the experimental data and build a model that can reliably give the pressure level based on measured hue and saturation readings. Polynomial regression, as a commonly used parametric curve fitting method, fits a nonlinear relationship between independent variables X and dependent variable y by statistically estimating y to be a linear combination of X and its higher-degree terms. The goodness of fitting largely depends on the wise choice of X and proper order of the highest degree. Seeing the clear clockwise progression from visualizing data points in a 2D plot with respect to hue and saturation readings, we first calculated the mean for all hue and saturation readings and used that center point as a new origin. Then the vector of a data point is defined as the one connecting the new origin and the data point itself. The vector of very first calibration data with lowest pressure level was taken as a reference vector, and we chose X to be the clockwise directional angle between any data vector and the reference vector. With a proper choice of the highest degree, we can fit relatively well on the whole set of calibration data (Figure 3.8B).
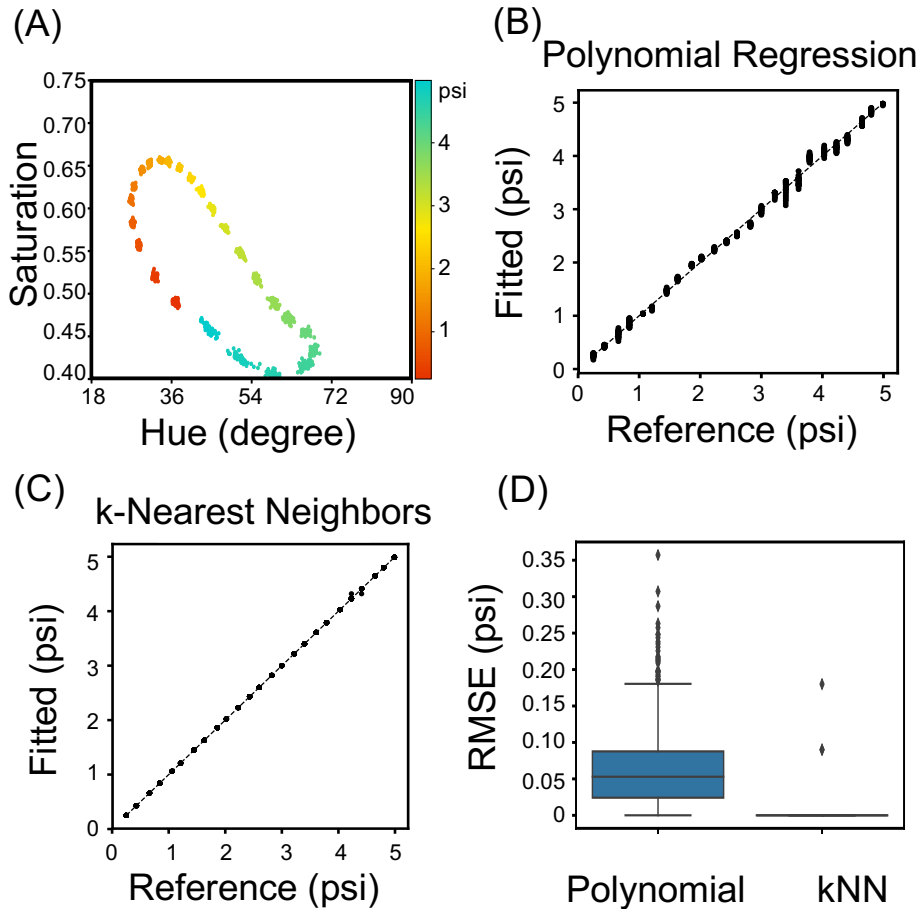
Figure 3.8 Nonlinear sensor calibration with experimental data. (A) Plot of saturation and hue readings corresponding to pressure levels between 0 to 5 psi. (B) The goodness of fitting by applying polynomial regression on the dataset. The fitted value is given by the model based on saturation and hue readings as input and plotted against the actual value as reference. (C) The goodness of fitting by applying kNN regression on the dataset. (D) Generalized model performance by using leave-one-out cross-validation. Each point is the difference between the actual pressure of one test and predicted pressure with saturation and hue readings based on a model fitting on data from all other tests

K-nearest neighbors regression, on the other hand as a non-parametric technique [139], predict the value of y based on a similarity measure between a new measurement and all the existing calibration data. Accuracy is usually affected by the choice of distance function as a measure of similarity, and the choice of how many neighbors to look at. We chose the Euclidean distance between data points as the similarity measurement and achieved an even better fitting on

the whole calibration data (Figure 3.8C). To further evaluate the generalized model performance when encountering new measurements in the future and prevent overfitting, leave-one-out cross-validation (LOOCV) is performed using the calibration dataset when choosing parameters and the error distribution with the optimal parameters is visualized with a boxplot (Figure 3.8D). kNN shows a better performance with lower median error, narrower error variation and fewer outliers. The absolute error is less than 0.2 psi as demonstrated by the outlier with the largest error. The intuition is that our calibration data are essentially clusters of data at different pressure levels with variations due to noises. As long as our calibration well covers the measurement range with a dense enough setting of pressure intervals, it's safe to map any new measurement to be an average of a few most similar data points from calibration. By setting even denser pressure calibration intervals, the error from kNN regression can be ultimately reduced down to the precision of the pressure regulator used for calibration, which is not necessarily true the case for using polynomial regression. Certainly, some compromise needs to be made here between prediction accuracy and the convenience of calibration.

3.2.2.3 Pressure mapping inside a complex microfluidic network

Using the model built by kNN regression with calibration performed beforehand, we are able to map color measurement to the actual pressure level that is applied to a specific location. There are several potential applications of this system that involves multi-spot pressure monitoring using an imaging system. Here we demonstrate one of them by mapping the pressure distribution inside a complex microfluidic network (Figure 3.9A). We made the microfluidic channel with standard soft lithography and then bonded it on top of our device. The microfluidic network spans across an area of 8mm × 5mm and is fully covered by more than a hundred thousand pressure

sensing spots with 50μm center-to-center distance apart from each other. A flow-rate-controlled syringe pump is used to pump water through the network at different flow rates. After the flow gets stabilized, color images are captured at inlet, middle and outlet areas of the network in order to map the pressure. Due to the pressure drop between upstream and downstream of a continuous flow, each area naturally exhibits a different color which can be interpreted as a different pressure level (Figure 3.9A). At each location we repeat the measurements by taking multiple image frames at steady state flow condition. Each frame of image actually contains more than a hundred spot measurements and high spatial resolution pressure mapping across a large area is feasible. As a demonstration we crop the images and look at the same spot consistently for each area at different flow rate conditions. After image-processing, hue and saturation readings from the spot are extracted and plotted as data points with labeled flow rates (Figure 3.9, BCD). Then with the previous calibration data and kNN regression modeling, these data points labeled with flow rates are mapped to corresponding pressure levels applied at that spot when flow condition has been stabilized (Figure 3.9E). It serves as a characterization of the expected flow behavior for this specific channel design. Pressure drop between any two spots can be simply calculated and used to monitor the flow condition, similar to voltage monitoring in electric circuits. If the change is due to overall flow rate adjustment we should expect the pressure drop for different regions to change simultaneously. However, if the change is due to anomalies such as clogging or leakage at some location, we will see the pressure drop changes dramatically in the affected region while not so much for other unaffected regions.
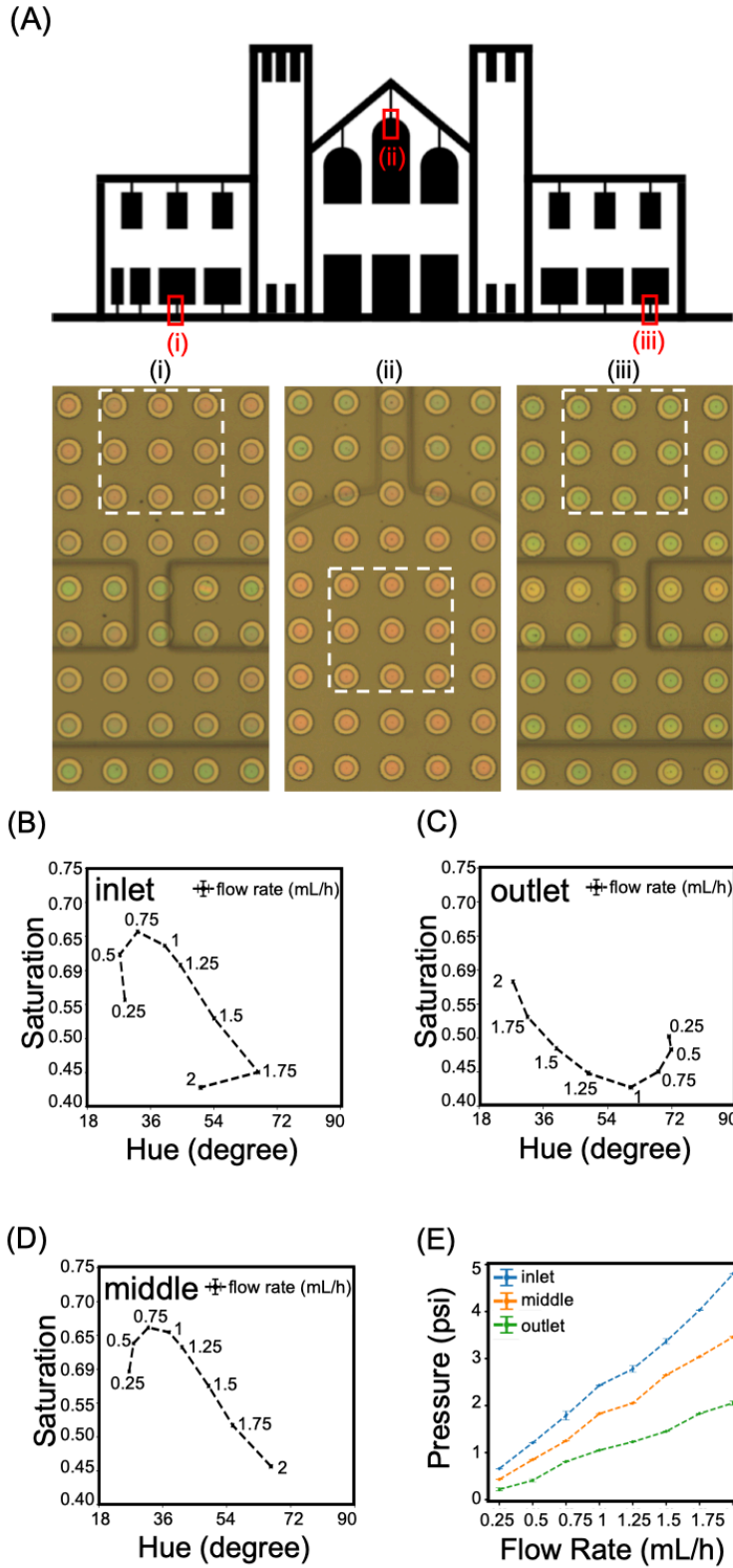
*Figure 3.9 Pressure distribution mapping of a complex microfluidic network. (A)
Design of a complex microfluidic network spanning across 7mm by 4mm area. The*

images of steady-state conditions for 0.25 ml/h flow rate are captured at (i) inlet, (ii) middle and (iii) outlet of the microfluidic network and show different colors representing different pressure levels. (BCD) Saturation and hue readings when the system reaches steady state for a flow rate between 0.25 and 2 ml/h at inlet, middle and outlet locations. (E) Plot of close-to-linear relationship between pressure and flow rate for inlet, middle and outlet locations.

3.2.3 Discussion

The pressure distribution inside a microfluidic network provides vital information about its operating condition. There have been efforts in developing microfluidic pressure sensors but high spatial resolution pressure mapping on a large scale has not been demonstrated yet. We applied facile microfabrication techniques to make this pressure-sensitive substrate with more than a hundred thousand sensing spots in 1cm² area with a 50μm spatial resolution, and it can be further scaled up if necessary. Due to the solid anchoring of silicon between two sensing spots, their mechanical deformation responses are well decoupled when separated by 50μm apart. As a transducer our interferometric device converts mechanical pressure to optical spectral information and utilized the high-resolution, both spatially and temporally, imaging capabilities from modern color image sensors. For our demonstration we used 10× objective in the imaging system, and every spot measurement consists of more than 40 pixels in the image. Due to the fact that the silicon dioxide disk of the optical micro-cavity is rigid and stays flat during operation, these many pixels are actually redundant in terms of measurement as they are expected to and in fact give almost same readings. Ideally, we only need a few pixels for each spot measurement. If we opt for a larger format image sensor and a lower magnification objective lens, as long as the sensor pixel size is not limiting the overall imaging resolution, each frame of image can cover an even larger area and will be more suitable for simultaneous large-scale activity monitoring. As for temporal resolution, latest CMOS sensor from major manufacturers can easily capture images at more than

64

100 frames per second (fps), and specialized high-speed cameras can provide frame rates up to a million fps. Transient processes that involve rapid pressure transition or propagation can be well monitored.

We choose to operate the device by limiting the air gap thickness within the range of roughly 300-600 nm because it has the best color performance and transition contrast. For the specific mechanical design in our demonstration, the pressure can be measured up to 5psi. Because the optical design and mechanical design are relatively decoupled, this dynamic range can be easily customized by tuning the thickness or elastic modulus of the PDMS thin film depending on the specific application. We achieved 0.2 psi measurement precision, which can be further improved by obtaining more data points for the nonlinear sensor calibration using a calibrated pressure source with better feedback control for higher accuracy and stability.

An offline framework of sensor calibration, image processing and finally pressure calculation has been demonstrated in this work. With an optimized and well-implemented computation framework, flow conditions inside a complex microfluidic network can be monitored in real-time with fully mapped pressure distribution to detect anomalies such as clogging or leakage promptly. As a pressure-sensitive device, our system can also find potential applications in other fields such as biomechanical studies of cells and tissues [140]–[143].

3.2.4 Methods

3.2.4.1 Device fabrication

Based on the design concept we initially tried to adopt the fabrication technique used in making the phase-spot device and transfer oxide disks directly onto an array of soft PDMS micro O-rings to construct micro optical cavities. However, the difference here is that the disk is not fully

in contact with soft PDMS. During the step of ultrasonication to break the silicon anchors, due to

the lack of mechanical support and damping to absorb the vibration, the thin silicon dioxide disk

would break and leave a hole in the middle of it, resulting in the failure of device fabrication.
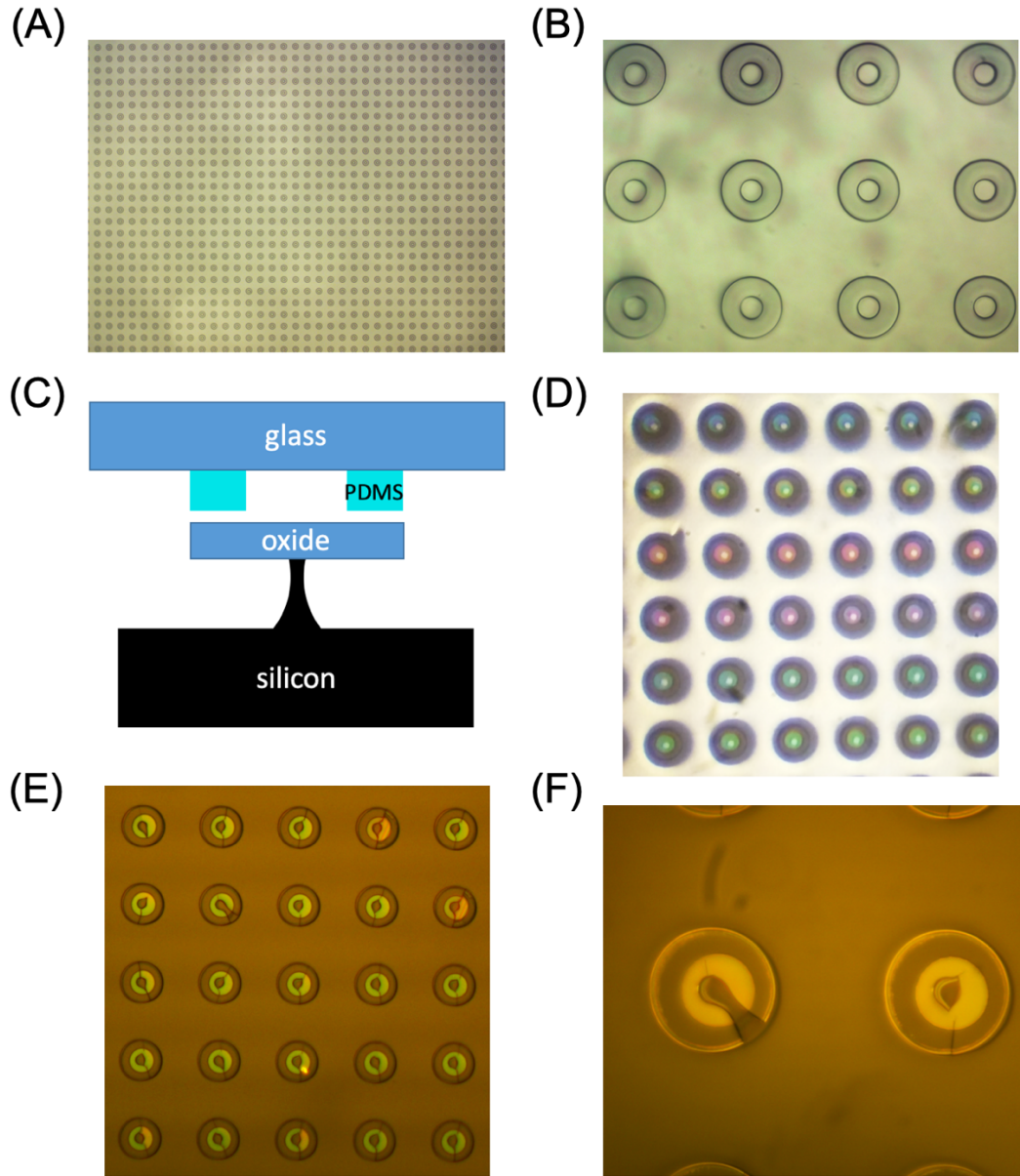
Figure 3.10 Initial fabrication of micro optical cavity array. (A) Massive micro O-ring array made of soft PDMS on glass. (B) Higher magnification microscopic images of PDMS micro O-ring on glass. (C) Initial fabrication process design. (D) Device assembly right after contact between two parts in aligner showing beautiful colors due to interferometric reflection. (E) Oxide disks break after ultrasonication. The remaining oxide still forms an optical cavity with air and glass substrate, while

the hole without oxide shows no color (F) Higher magnification microscopic images showing damage of oxide disk.

After realizing the oxide disks need to have good contact and support during transfer, the final device is fabricated using a combination of standard silicon-based microfabrication and PDMS-based heterogeneous integration processes [13]. It can be summarized into three major steps: (1) A thin PDMS film is prepared by spin coating (4000rpm, 5min) and baking inside an oven at 65C until cure to achieve a final thickness of 6 μm. This PDMS film is later peeled and attached temporarily onto a hybrid glass-PDMS buffer. (2) A 1.56 μm thick thermally grown silicon dioxide layer is patterned into a disk array and the silicon substrate underneath is isotropically etched to form thin needle-shaped anchors. The silicon dioxide disks are then permanently bonded to the thin PDMS film with oxygen plasma treatment (80 W, 500 mT, 30 s) and oven baking (65◦C, 2 hours). After that the whole piece is immersed into a mixed water/acetone (1:1 v/v ratio) ultrasonic bath to break the silicon anchors and transfer the disk array. (3) A same silicon substrate with thermally-grown oxide goes through oxide deposition using plasma-enhanced chemical vapor deposition (PECVD) to add extra height (~550 nm) and define the initial air gap spacing. An array of holes is etched out to accommodate the oxide disk array and form optical cavities. Finally, this substrate is align-bonded to the thin PDMS film with oxide disk array and the hybrid buffer is peeled off. The device can go through an optional prolonged oxygen plasma treatment (80 W, 500 mT, 7 mins) which creates a thin silica-like layer on top of the PDMS to help block the penetration of water vapor and greatly extend its working life span under high hydraulic pressure [144], [145]. More detailed fabrication processes are illustrated in Figure 3.11.
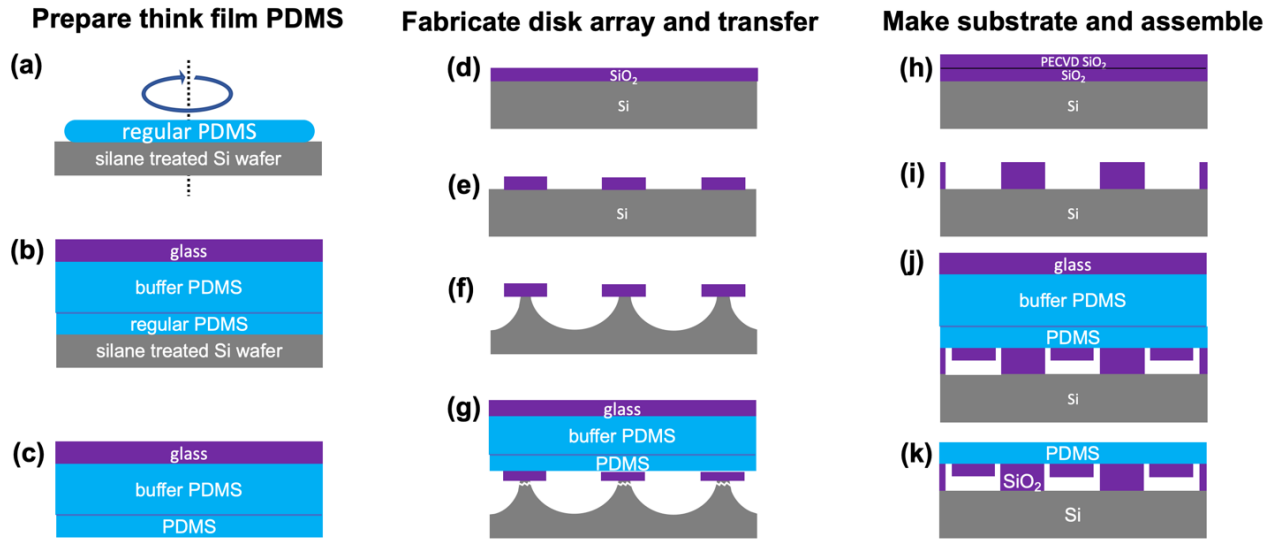
Figure 3.11 Fabrication process of optical cavity array.
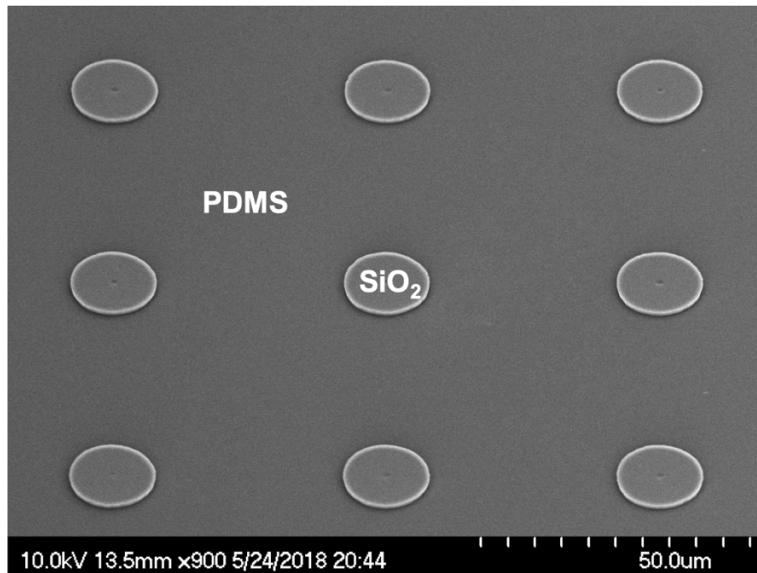
Figure 3.12 Circular oxide disks transferred onto flat PDMS film.

3.2.4.2 Imaging setup

An upright microscope (Zeiss Axio Scope A1) is used to image the device with a 10× objective lens (N.A. 0.25). The broadband white illumination is from a halogen lamp (HAL 100) attached to the microscope and set to a fixed driving voltage during every experiment to ensure

consistency. A color CMOS camera sensor (Grasshopper GS3-U3-41C6C-C) is attached to the microscope to capture images for analysis. The camera is set to a fixed 0.35 ms exposure time with all image preprocessing turned off and export images as raw files to prevent information loss.

3.2.4.3 FDTD simulation and numerical calculation

The numerical simulation is conducted using a commercial FDTD software (RSoft) for a single unit of optical cavity. The model is simplified to a 2D cross-sectional study with periodic boundary conditions on two sides. Material properties are set accordingly with the built-in refractive index library. An emitter sends optical waves vertically into the cavity and a receiver behind the emitter measures the reflected power. We run parametric sweep on the wavelength of light and air gap thickness to generate the reflectance spectra in Figure 3.6A. To compute the color transition in Figure 3.6D, we adopted the illumination spectrum of the halogen lamp (Figure 3.13a) measured by a commercial spectrometer (Ocean Optics HL-2000-HP), and the camera sensor color sensitivity spectra (Figure 3.13b) in the specification manual provided by the manufacturer.
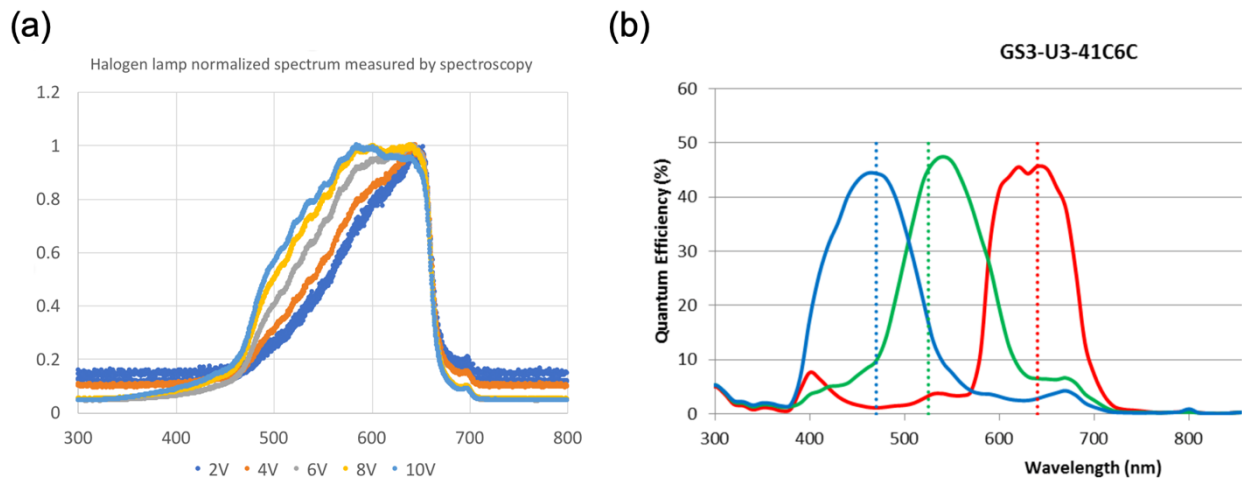
Figure 3.13 Spectrum data *of (a) halogen lamp and (b) camera RGB sensitivity.*

69

3.2.4.4 Pressure and flow rate control

A precision pressure regulator (Marsh Bellofram 510PI0G015P0100 Digital Pressure Regulator) is used to control the pressure output during calibration experiments. The regulator takes a 20psi compressed air as input and regulates the pressure output within the range of 0 to 15 psi based on the voltage control signal from 0 to 10V using a DC power supply (Gw Instek GPS-3303), and has a built-in digital display for pressure readout. It can maintain a stable pressure output with < 0.1psi fluctuations using feedback control. Pressure levels from 0.2 psi to 5 psi with a step of 0.2 psi are tested. At each pressure level calibration is repeated multiple times by taking 45 consecutive images with 100 ms interval and fixed 0.35 ms exposure.
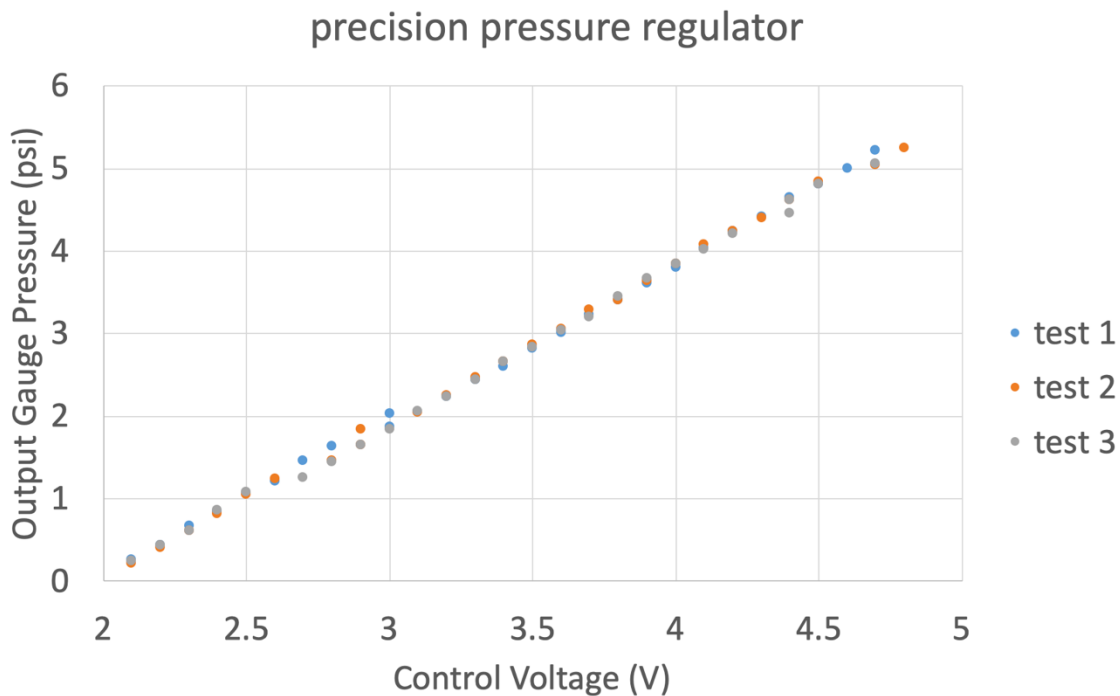
Figure 3.14 Liner response of output pressure from precision regulator with voltage control

A syringe pump (Harvard PHD 2000 Infusion) is used to control the flow rate during pressure mapping demonstrations. A syringe (BD 10 ml, Luer-Lok) filled with DI water is mounted onto the pump and supply a continuous flow to the microfluidic network through tubing

connection. Various flow rates from 0.25 ml/h to 2 ml/h with a step of 0.25 ml/h are tested. After each flow rate adjustment, we wait for at least 10 mins in order to let the flow stabilize and reach steady state condition [122]. Then images are captured at several locations inside the microfluidic network to map out the pressure distribution. For each condition the measurement is repeated multiple times by taking 45 consecutive images with 100 ms time gap and fixed 0.35 ms exposure.

3.2.4.5 Image processing

Each measurement consists of 45 still images with minimal relative movement. We take the first frame from each measurement to find the center coordinates for pressure sensing spots of interest and assume them to remain the same for following frames. Scikit-image, an open-sourced image processing library for the Python programming language [146], together with customized codes are used to extract the hue and saturation readings with high efficiency. Each color spot actually contains more than 100 pixels in the image. To improve accuracy, we don't include pixels close to object edges and image artifacts, and thus limit our calculations to pixels within a ring-shaped area whose inner circle is 3 pixels away from the spot center and outer circle 3 pixels away from the spot edge, leaving us about 40 pixels for each spot with plenty of redundancy. The hue and saturation readings for these pixels are averaged such that each spot ends up having one hue reading and one saturation reading in a single frame of image. Therefore 45 images provide 45 times of measurements for each pressure level calibration experiment. Since there are 25 pressure levels sampled between 0.2 psi to 5 psi every 0.2 psi, we append these measurements together to form a calibration dataset consisting of 1125 data points in total and provide the basis for regression analysis of one measurement spot. Each calibration data point has the hue and saturation readings, and is associated/labeled with a pressure level somewhere between 0.2 psi to 5 psi.

71
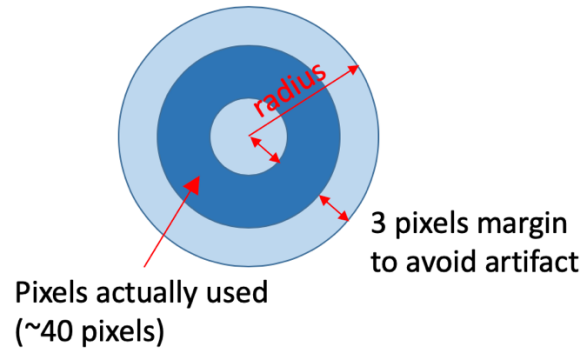
Figure 3.15 Image processing of a single disk.

3.2.4.6 Regression analysis and pressure prediction

For each measurement spot we have 1125 calibration data points based on which we want to perform a regression analysis between the color attributes and the pressure level as a way of nonlinear sensor calibration. Fig4a serves as the data visualization and inspires us to try out two regression models: parametric polynomial regression and non-parametric kNN regression. Scikit-learn, an open-sourced statistical learning library for the Python programming language [147], is used for the regression analysis and establish the relationship between color attribute readings and the pressure level. To select the optimal parameters, namely the highest degree in polynomial regression and the number of neighbors in kNN regression, we used leave-one-out cross-validation (LOOCV) to evaluate the model performance with mean absolute error as the evaluation metric. After establishing the relationship and saving the model, we are able to make pressure prediction based on the color of a measurement spot by extracting the hue and saturation readings as inputs and correlating them to a pressure level.

Chapter 4 Conclusion

This dissertation focused on the engineering development of optofluidic platform using heterogeneous integration with potential applications in manipulation and mechanical property analysis of biological cells. To properly prepare the cell sample for downstream processing and analysis, we first developed a new pulsed laser activated sorter integrating tunable single stream DEP focusing which can be more beneficial for fluorescence-based rare cell sorting because of no dilution. To enhance the DEP manipulation force, potentially improving sorting throughput, we developed a heavily doped silicon electrode to decouple the strong electric field region from the electrode interface and provides a large interface capacitance to prevent surface charging in high conductivity media, thereby effectively suppressing electrochemical reactions. 9-fold enhancement of maximum DEP force in 1× PBS buffer with an electrical conductivity of 1 S/m, providing more efficient DEP manipulation.

While MEMS systems also have been widely used for downstream processing and analysis, we explored the opportunities in developing optofluidic platforms for mechanobiology studies of cells. To tackle the big problem of high-throughput cell stiffness measuring, we believe the complete system can be broken down into three components: a method to efficiently pattern cells into an 2D array, a setup to apply external forces to cells with precise control and a sensor to accurately measure the small deformation of cells with a high throughput. Following this roadmap, we set out to develop solutions for each step individually and in the future integrate them together.

We developed a lift-off cell lithography for cell patterning with high-throughput and high-efficiency. Compared to previous methods our method can pattern cells across a much larger area (1.2 x 1.2 cm² area) and the result pattern is much cleaner with almost no cell residue in undesired

areas. The whole process is biocompatible and easy-to-fabricate, and it can work with both adherent and non-adherent cells.

Finally, we developed a pressure sensing substrate that can map pressure distribution in a parallel fashion across 1 cm^2 area with spatial resolution of 50 μm. It utilizes colorimetric interferometry from an array of micro-fabricated optical cavities and the device can be easily integrated into an optical microscope setup. To prove the concept and demonstrate its capability we used the substrate to map out the pressure distribution inside a complex microfluidic network with more than 100,000 sensing spots. The measurement range can be customized by tuning the design and material properties depending on the specific application. We achieved 0.2 psi measurement precision, which can be further improved by obtaining more data points for the nonlinear sensor calibration using a calibrated pressure source with better feedback control for higher accuracy and stability. At the same time, we fully utilized the advancement of latest CMOS sensor technologies which offer higher resolution, larger sensor format and higher frame rate, which all promise a future of large area and high spatial/temporal resolution monitoring of mechanobiological activities.

While we have worked out some of the engineering issues in developing heterogeneously integrated optofluidic platforms, one must note that it will take much greater efforts and more resources to get them work in and contribute to actual cell studies. It requires engineers to closely collaborate with biologists and doctors to figure out the compatibility issues and optimize the designs and processes based on specific applications. During my research work I had some successful collaboration of this kind through trials and errors, but a more systematic approach of collaboration to effectively identify supply and demand between multiple parties will save a lot of time and resources.

Appendix A

DEP-PLACS setup and experimental procedure
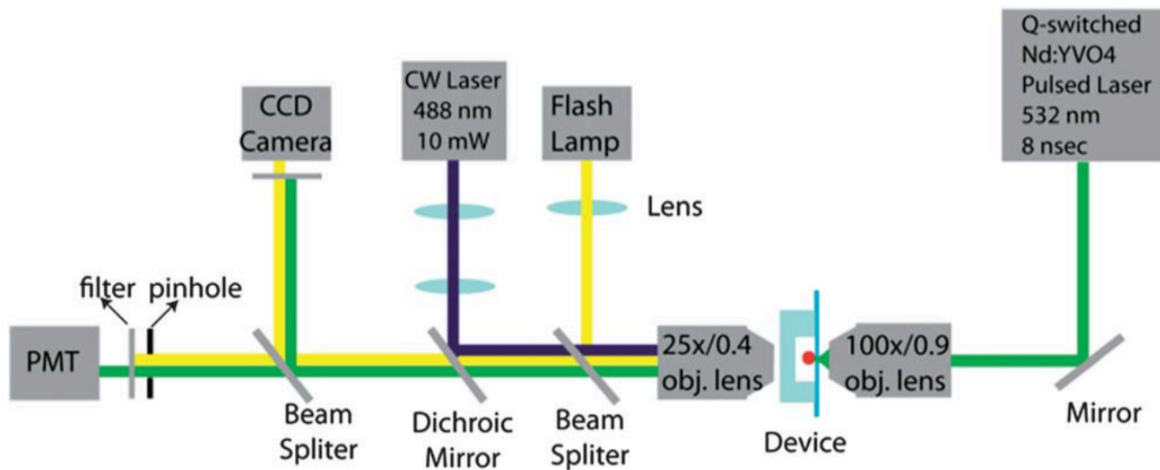
Schematic of optical setup for PLACS[5]

(1) Turn on all equipment and warm up 532nm pulsed laser for a few minutes.

(2) Load device onto setup (thinner PDMS connector gives better image quality), adjust device position to have roughly in-focus image of device onto camera, insert paper between device and 100×, adjust lens components in front of 488nm laser and dichroic mirror to align 488nm blue laser with optical axis of 25× objective and have max intensity seen from the paper.

(3) Adjust device channel position to have 488nm blue laser spot close to switching junction. Take out paper, change 532nm pulsed laser to adj energy mode (low energy) and internal trigger mode, adjust mirror in front of 532nm and 100× objective to align 532nm laser spot to triggering position. Adjust camera position to have the switching junction in frame. Adjust 25× objective to have 532nm spot in best focus observed from camera, then adjust device to have best focus onto camera.

(4) Adjust flashlamp, lens and beam splitter to have flash lamp spot overlapped with 488/532nm laser on and beyond flip mirror of beam splitter. Use the right filter in front of camera.

(5) Adjust white illumination LED to have overlap with 488/532nm laser on and beyond flip mirror.

(6) Put a USB camera in the position of PMT tube and adjust to have visible image of switching junction. Align pinhole to close around detection region. Remove USB camera put PMT back.

(7) Connect tubings, electrical wiring connections, pump in sample, start DEP focusing.

(8) Fix flow rate with 2ml/h for sample channel and 2.5ml/h for dye channel. Wait until there is no more gas/air bubble in tubing to make sure flow is stablized. Reduce 532nm pulsed laser energy by rotating half wave plate (~82degree), start camera trigger laser/flash 1000us master delay, 3us flash delay, camera 20ms exposure, 2fps, laser max power, ext trigger, adjust device lateral position to find stable but not max size bubble. Gradually increase 532nm pulsed laser energy (rotate half wave plate) to ensure not burning device, up to 86 deg. (Too large energy disrupts flow pattern)

(9) Start PMT trigger laser flash, power on PMT 1V/5V, 400 ticks period, threshold 60 counts, 488 nm laser 20mW.

(10) Tunable focusing to bias particle stream into waste close to junction. Delay to ~300us and tune resistor (350 Ω) and delay time to maximize switching efficiency. Keep switching window within 200us. Put on a green pass filter in front of camera to have better trace image.

(11) Start collecting sample. Gauge 22 tubing=0.64mm diameter. Collection at 1ml/h, it flushes 5cm tubing per minute. Each 6min collection gives 100uL volume collection sample.

Appendix B

Summary of DEP response for typical particle types

higher conductivity

smaller particle

more difficult to trap
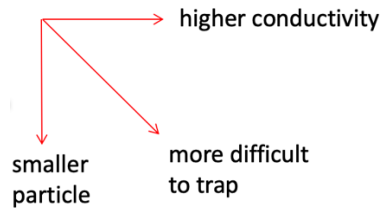
Medium conductivity	0.01S/m		0.1S/m		1S/m	
HeLa cells	+	-	+	-	-	
10um PS beads	-		-		-	
E-coli	+	-	+	-	-	
<1um PS beads	+	-	+	-	-	
proteins, DNA	N/A		N/A		+	-

Note: + for positive DEP, - for negative DEP

Appendix C

Summary of fabrication processes and parameters

- **Fibronectin coating**

  20ul solution +180ul PBS to dilute. Substrate in air plasma for 1min, put on solution and let sit

  for 10min, then rinse.

- **Recipe for AZ-4620**

  7um thickness: 4000rpm, soft bake 100c 1.5min, expose 60s, develop 1:3 2min

  15um thickness: 1000rpm, soft bake 100c 6min, expose 160s, develop 1:3 2min

- **Image reversal of AZ-5214IR**

  Soft bake 95c 2min, 3s exposure, 2nd bake 125c 30s, flood exposure 16s, develop 1:4 1min

- **Tune PDMS adhesion with glass/oxide**

  Reduce adhesion: silane treatment

  Increase temporary adhesion: low power air plasma treatment for 1~2 seconds

  Permanent bonding: oxygen plasma treatment for ~30 seconds

Reference

[1] M. E. Lidstrom and M. C. Konopka, "The role of physiological heterogeneity in microbial population behavior," *Nature Chemical Biology*, vol. 6, no. 10, pp. 705–712, Oct. 2010.

[2] C. J. Flaim, S. Chien, and S. N. Bhatia, "An extracellular matrix microarray for probing cellular differentiation," *Nat. Methods*, vol. 2, no. 2, pp. 119–125, Feb. 2005.

[3] S. Gobaa, S. Hoehnel, M. Roccio, A. Negro, S. Kobel, and M. P. Lutolf, "Artificial niche microarrays for probing single stem cell fate in high throughput," *Nat. Methods*, vol. 8, no. 11, pp. 949–955, Oct. 2011.

[4] W. M. Weaver *et al.*, "Advances in High-Throughput Single-Cell Microtechnologies," *Curr Opin Biotechnol*, vol. 0, pp. 114–123, Feb. 2014.

[5] Y. Chen, T.-H. Wu, Y.-C. Kung, M. A. Teitell, and P.-Y. Chiou, "3D pulsed laser-triggered high-speed microfluidic fluorescence-activated cell sorter," *The Analyst*, vol. 138, no. 24, p. 7308, 2013.

[6] Y. Chen, A. J. Chung, T.-H. Wu, M. A. Teitell, D. Di Carlo, and P.-Y. Chiou, "Pulsed Laser Activated Cell Sorting with Three Dimensional Sheathless Inertial Focusing," *Small*, vol. 10, no. 9, pp. 1746–1751, May 2014.

[7] P. Y. Chiou, A. T. Ohta, and M. C. Wu, "Massively parallel manipulation of single cells and microparticles using optical images," *Nature*, vol. 436, no. 7049, pp. 370–372, Jul. 2005.

[8] Y. Yang, Y. Mao, K.-S. Shin, C. O. Chui, and P.-Y. Chiou, "Self-Locking Optoelectronic Tweezers for Single-Cell and Microparticle Manipulation across a Large Area in High Conductivity Media," *Scientific Reports*, vol. 6, no. 1, Sep. 2016.

[9] Y.-C. Wu *et al.*, "Massively parallel delivery of large cargo into mammalian cells with light pulses," *Nature Methods*, vol. 12, no. 5, pp. 439–444, Apr. 2015.

[10] T. Man *et al.*, "Intracellular Photothermal Delivery for Suspension Cells Using Sharp Nanoscale Tips in Microwells," *ACS Nano*, vol. 13, no. 9, pp. 10835–10844, Sep. 2019.

[11] S. E. Cross, Y.-S. Jin, J. Rao, and J. K. Gimzewski, "Nanomechanical analysis of cells from cancer patients," *Nature Nanotechnology*, vol. 2, no. 12, pp. 780–783, Dec. 2007.

[12] D. Alsteens, H. E. Gaub, R. Newton, M. Pfreundschuh, C. Gerber, and D. J. Müller, "Atomic force microscopy-based characterization and design of biointerfaces," *Nature Reviews Materials*, vol. 2, no. 5, p. 17008, Mar. 2017.

[13] X. Wen *et al.*, "Flexible, multifunctional neural probe with liquid metal enabled, ultra-large tunable stiffness for deep-brain chemical sensing and agent delivery," *Biosensors and Bioelectronics*, vol. 131, pp. 37–45, Apr. 2019.

[14] J. Homola, "Present and future of surface plasmon resonance biosensors," *Anal Bioanal Chem*, vol. 377, no. 3, pp. 528–539, Oct. 2003.

[15] Y. Fang, A. M. Ferrie, N. H. Fontaine, J. Mauro, and J. Balakrishnan, "Resonant Waveguide Grating Biosensor for Living Cell Sensing," *Biophysical Journal*, vol. 91, no. 5, pp. 1925–1940, Sep. 2006.

[16] G. M. Whitesides, "The origins and the future of microfluidics," *Nature*, vol. 442, no. 7101, pp. 368–373, Jul. 2006.

[17] Y. Xia and and G. M. Whitesides, "Soft Lithography," *Annual Review of Materials Science*, vol. 28, no. 1, pp. 153–184, 1998.

[18] T. L. Liu, X. Wen, Y.-C. Kung, and P.-Y. C. Cru, "Fabrication strategy for micro soft robotics with semiconductor devices integration," in *2017 IEEE 30th International Conference on Micro Electro Mechanical Systems (MEMS)*, 2017, pp. 663–666.

[19] E. M. Darling and D. Di Carlo, "High-Throughput Assessment of Cellular Mechanical Properties," *Annu. Rev. Biomed. Eng.*, vol. 17, no. 1, pp. 35–62, Dec. 2015.

[20] K. L. Holmes *et al.*, "International Society for the Advancement of Cytometry cell sorter biosafety standards," *Cytometry A*, vol. 85, no. 5, pp. 434–453, May 2014.

[21] A. Y. Fu, H.-P. Chou, C. Spence, F. H. Arnold, and S. R. Quake, "An Integrated Microfabricated Cell Sorter," *Anal. Chem.*, vol. 74, no. 11, pp. 2451–2457, Jun. 2002.

[22] S. Hwan Cho, C. H. Chen, F. S. Tsai, J. M. Godin, and Y.-H. Lo, "Human mammalian cell sorting using a highly integrated micro-fabricated fluorescence-activated cell sorter (μFACS)," *Lab on a Chip*, vol. 10, no. 12, pp. 1567–1573, 2010.

[23] M. M. Wang *et al.*, "Microfluidic sorting of mammalian cells by optical force switching," *Nat Biotech*, vol. 23, no. 1, pp. 83–87, Jan. 2005.

[24] A. A. Nawaz *et al.*, "Acoustofluidic Fluorescence Activated Cell Sorter," *Anal. Chem.*, vol. 87, no. 24, pp. 12051–12058, Dec. 2015.

[25] T.-H. Wu *et al.*, "Pulsed laser triggered high speed microfluidic fluorescence activated cell sorter," *Lab on a Chip*, vol. 12, no. 7, p. 1378, 2012.

[26] Y.-C. Kung, K.-W. Huang, Y.-J. Fan, and P.-Y. Chiou, "Fabrication of 3D high aspect ratio PDMS microfluidic networks with a hybrid stamp," *Lab Chip*, vol. 15, no. 8, pp. 1861–1868, Mar. 2015.

[27] Ximiao Wen, Tingyi Liu, and Pei-Yu Chiou, "A hybrid silicon-PDMS multifunctional neural probe," 2016, pp. 1–2.

[28] Y.-C. Kung and P.-Y. Chiou, "Tunable, high-speed, and three-dimensional microfluidic device for ultra-high precision size-based particle separation," in *2016 IEEE 29th*

International Conference on Micro Electro Mechanical Systems (MEMS), 2016, pp. 800–803.

[29] Y.-C. Kung, K.-W. Huang, W. Chong, and P.-Y. Chiou, "Tunnel Dielectrophoresis for Tunable, Single-Stream Cell Focusing in Physiological Buffers in High-Speed Microfluidic Flows," *Small*, vol. 12, no. 32, pp. 4343–4348, Aug. 2016.

[30] K. R. Rau, P. A. Quinto-Su, A. N. Hellman, and V. Venugopalan, "Pulsed Laser Microbeam-Induced Cell Lysis: Time-Resolved Imaging and Analysis of Hydrodynamic Effects," *Biophys J*, vol. 91, no. 1, pp. 317–329, Jul. 2006.

[31] F. F. Becker, X.-B. Wang, Y. Huang, R. Pethig, J. Vykoukal, and P. R. Gascoyne, "Separation of human breast cancer cells from blood by differential dielectric affinity," *Proceedings of the National Academy of Sciences*, vol. 92, no. 3, pp. 860–864, 1995.

[32] H. Li and R. Bashir, "Dielectrophoretic separation and manipulation of live and heat-treated cells of Listeria on microfabricated devices with interdigitated electrodes," *Sensors and Actuators B: Chemical*, vol. 86, no. 2, pp. 215–221, 2002.

[33] C. Iliescu, G. Tresset, and G. Xu, "Continuous field-flow separation of particle populations in a dielectrophoretic chip with three dimensional electrodes," *Applied Physics Letters*, vol. 90, no. 23, p. 234104, Jun. 2007.

[34] A. Jamshidi *et al.*, "Dynamic manipulation and separation of individual semiconducting and metallic nanowires," *Nat Photonics*, vol. 2, no. 2, pp. 86–89, 2008.

[35] J. Li, Q. Zhang, N. Peng, and Q. Zhu, "Manipulation of carbon nanotubes using AC dielectrophoresis," *Applied Physics Letters*, vol. 86, no. 15, p. 153116, Apr. 2005.

[36] S. Park *et al.*, "Floating electrode optoelectronic tweezers: Light-driven dielectrophoretic droplet manipulation in electrically insulating oil medium," *Appl. Phys. Lett.*, vol. 92, no. 15, p. 151101, Apr. 2008.

[37] W. A. Braff, A. Pignier, and C. R. Buie, "High sensitivity three-dimensional insulator-based dielectrophoresis," *Lab on a Chip*, vol. 12, no. 7, p. 1327, 2012.

[38] N. Mittal, A. Rosenthal, and J. Voldman, "nDEP microwells for single-cell patterning in physiological media," *Lab on a Chip*, vol. 7, no. 9, p. 1146, 2007.

[39] J. Voldman, "Electrical forces for microscale cell manipulation," *Annu. Rev. Biomed. Eng.*, vol. 8, pp. 425–454, 2006.

[40] X. Ding *et al.*, "On-chip manipulation of single microparticles, cells, and organisms using surface acoustic waves," *PNAS*, vol. 109, no. 28, pp. 11105–11109, Jul. 2012.

[41] T. Laurell, F. Petersson, and A. Nilsson, "Chip integrated strategies for acoustic separation and manipulation of cells and particles," *Chem. Soc. Rev.*, vol. 36, no. 3, pp. 492–506, 2007.

[42] J. Yan, D. Skoko, and J. F. Marko, "Near-field-magnetic-tweezer manipulation of single DNA molecules," *Phys. Rev. E*, vol. 70, no. 1, p. 011905, Jul. 2004.

[43] H. Lee, A. M. Purdon, and R. M. Westervelt, "Manipulation of biological cells using a microelectromagnet matrix," *Applied Physics Letters*, vol. 85, no. 6, pp. 1063–1065, Aug. 2004.

[44] C. Qian *et al.*, "Dielectrophoresis for Bioparticle Manipulation," *International Journal of Molecular Sciences*, vol. 15, no. 10, pp. 18281–18309, Oct. 2014.

[45] R. Martinez-Duarte, "Microfabrication technologies in dielectrophoresis applications-A review: Microfluidics and Miniaturization," *ELECTROPHORESIS*, vol. 33, no. 21, pp. 3110–3132, Nov. 2012.

[46] A. Ramos, H. Morgan, N. G. Green, and A. Castellanos, "Ac electrokinetics: a review of forces in microelectrode structures," *J. Phys. D: Appl. Phys.*, vol. 31, no. 18, p. 2338, 1998.

[47] C.-F. Chou *et al.*, "Electrodeless dielectrophoresis of single-and double-stranded DNA," *Biophysical Journal*, vol. 83, no. 4, pp. 2170–2179, 2002.

[48] E. B. Cummings and A. K. Singh, "Dielectrophoresis in Microchips Containing Arrays of Insulating Posts: Theoretical and Experimental Results," *Analytical Chemistry*, vol. 75, no. 18, pp. 4724–4731, Sep. 2003.

[49] A. LaLonde, M. F. Romero-Creel, M. A. Saucedo-Espinosa, and B. H. Lapizco-Encinas, "Isolation and enrichment of low abundant particles with insulator-based dielectrophoresis," *Biomicrofluidics*, vol. 9, no. 6, p. 064113, Nov. 2015.

[50] K.-T. Liao and C.-F. Chou, "Nanoscale Molecular Traps and Dams for Ultrafast Protein Enrichment in High-Conductivity Buffers," *Journal of the American Chemical Society*, vol. 134, no. 21, pp. 8742–8745, May 2012.

[51] B. H. Lapizco-Encinas, B. A. Simmons, E. B. Cummings, and Y. Fintschenko, "Dielectrophoretic Concentration and Separation of Live and Dead Bacteria in an Array of Insulators," *Analytical Chemistry*, vol. 76, no. 6, pp. 1571–1579, Mar. 2004.

[52] T. B. Jones, "Basic theory of dielectrophoresis and electrorotation," *IEEE Engineering in medicine and Biology Magazine*, vol. 22, no. 6, pp. 33–42, 2003.

[53] R. S. Thomas, H. Morgan, and N. G. Green, "Negative DEP traps for single cell immobilisation," *Lab on a Chip*, vol. 9, no. 11, pp. 1534–1540, 2009.

[54] H. Hsu, A. T. Ohta, P.-Y. Chiou, A. Jamshidi, S. L. Neale, and M. C. Wu, "Phototransistor-based optoelectronic tweezers for dynamic cell manipulation in cell culture media," *Lab Chip*, vol. 10, no. 2, pp. 165–172, 2010.

[55] N. Manaresi *et al.*, "A cmos chip for individual cell manipulation and detection," *IEEE Journal of Solid-State Circuits*, vol. 38, no. 12, pp. 2297–2305, Dec. 2003.

[56] S. R. Quake and A. Scherer, "From Micro- to Nanofabrication with Soft Materials," *Science*, vol. 290, no. 5496, pp. 1536–1540, 2000.

[57] F.-C. Huang, C.-S. Liao, and G.-B. Lee, "An integrated microfluidic chip for DNA/RNA amplification, electrophoresis separation and on-line optical detection," *ELECTROPHORESIS*, vol. 27, no. 16, pp. 3297–3305, Aug. 2006.

[58] A. Khademhosseini, R. Langer, J. Borenstein, and J. P. Vacanti, "Microscale technologies for tissue engineering and biology," *Proc. Natl. Acad. Sci. U.S.A.*, vol. 103, no. 8, pp. 2480–2487, Feb. 2006.

[59] B. Guillotin and F. Guillemot, "Cell patterning technologies for organotypic tissue fabrication," *Trends Biotechnol.*, vol. 29, no. 4, pp. 183–190, Apr. 2011.

[60] H. Andersson and A. van den Berg, "Microfabrication and microfluidics for tissue engineering: state of the art and future opportunities," *Lab Chip*, vol. 4, no. 2, pp. 98–103, Apr. 2004.

[61] S. Lindström and H. Andersson-Svahn, "Overview of single-cell analyses: microdevices and applications," *Lab Chip*, vol. 10, no. 24, pp. 3363–3372, Dec. 2010.

[62] C. A. Goubko and X. Cao, "Patterning multiple cell types in co-cultures: A review," *Materials Science and Engineering: C*, vol. 29, no. 6, pp. 1855–1868, Aug. 2009.

[63] C.-T. Ho, R.-Z. Lin, W.-Y. Chang, H.-Y. Chang, and C.-H. Liu, "Rapid heterogeneous liver-cell on-chip patterning via the enhanced field-induced dielectrophoresis trap," *Lab Chip*, vol. 6, no. 6, pp. 724–734, Jun. 2006.

[64] X. Zhu, K.-W. Tung, and P.-Y. Chiou, "Heavily doped silicon electrode for dielectrophoresis in high conductivity media," *Applied Physics Letters*, vol. 111, no. 14, p. 143506, Oct. 2017.

[65] Chow Yu Ting *et al.*, "Liquid Metal-Based Multifunctional Micropipette for 4D Single Cell Manipulation," *Advanced Science*, vol. 0, no. 0, p. 1700711, May 2018.

[66] N. Liu *et al.*, "Extracellular-controlled breast cancer cell formation and growth using non-UV patterned hydrogels via optically-induced electrokinetics," *Lab Chip*, vol. 14, no. 7, pp. 1367–1376, Mar. 2014.

[67] Y. Liu, C. Wu, H. S. S. Lai, Y. T. Liu, W. J. Li, and Y. J. Shen, "Three-Dimensional Calcium Alginate Hydrogel Assembly via TiOPc-Based Light-Induced Controllable Electrodeposition," *Micromachines*, vol. 8, no. 6, p. 192, Jun. 2017.

[68] K. Ino, A. Ito, and H. Honda, "Cell patterning using magnetite nanoparticles and magnetic force," *Biotechnology and Bioengineering*, vol. 97, no. 5, pp. 1309–1317, 2007.

[69] Z. Lin, X. Fan, M. Sun, C. Gao, Q. He, and H. Xie, "Magnetically Actuated Peanut Colloid Motors for Cell Manipulation and Patterning," *ACS Nano*, vol. 12, no. 3, pp. 2539–2545, 27 2018.

[70] D. J. Collins, B. Morahan, J. Garcia-Bustos, C. Doerig, M. Plebanski, and A. Neild, "Two-dimensional single-cell patterning with one cell per well driven by surface acoustic waves," *Nat Commun*, vol. 6, no. 1, pp. 1–11, Nov. 2015.

[71] J. Shi, D. Ahmed, X. Mao, S.-C. S. Lin, A. Lawit, and T. J. Huang, "Acoustic tweezers: patterning cells and microparticles using standing surface acoustic waves (SSAW)," *Lab Chip*, vol. 9, no. 20, pp. 2890–2895, Oct. 2009.

[72] C.-H. Lin *et al.*, "A microfluidic dual-well device for high-throughput single-cell capture and culture," *Lab Chip*, vol. 15, no. 14, pp. 2928–2938, Jul. 2015.

[73] J. Park *et al.*, "Single cell trapping in larger microwells capable of supporting cell spreading and proliferation," *Microfluidics and nanofluidics*, vol. 8, pp. 263–268, Feb. 2010.

[74] M. Junkin and P. K. Wong, "Probing cell migration in confined environments by plasma lithography," *Biomaterials*, vol. 32, no. 7, pp. 1848–1855, Mar. 2011.

[75] Y. Yang, N. Jamilpour, B. Yao, Z. S. Dean, R. Riahi, and P. K. Wong, "Probing Leader Cells in Endothelial Collective Migration by Plasma Lithography Geometric Confinement," *Sci Rep*, vol. 6, p. 22707, Mar. 2016.

[76] A. Azioune, M. Storch, M. Bornens, M. Théry, and M. Piel, "Simple and rapid process for single cell micro-patterning," *Lab Chip*, vol. 9, no. 11, pp. 1640–1642, Jun. 2009.

[77] K. Mandal, M. Balland, and L. Bureau, "Thermoresponsive micropatterned substrates for single cell studies," *PLoS ONE*, vol. 7, no. 5, p. e37548, 2012.

[78] S. Alom Ruiz and C. S. Chen, "Microcontact printing: A tool to pattern," *Soft Matter*, vol. 3, no. 2, pp. 168–177, 2007.

[79] R. S. Kane, S. Takayama, E. Ostuni, D. E. Ingber, and G. M. Whitesides, "Patterning proteins and cells using soft lithography," *Biomaterials*, vol. 20, no. 23–24, pp. 2363–2376, Dec. 1999.

[80] X. Tang, M. Y. Ali, and M. T. A. Saif, "A novel technique for micro-patterning proteins and cells on polyacrylamide gels," *Soft Matter*, vol. 8, no. 27, pp. 7197–7206, Jun. 2012.

[81] J. Moeller, A. K. Denisin, J. Y. Sim, R. E. Wilson, A. J. S. Ribeiro, and B. L. Pruitt, "Controlling cell shape on hydrogels using lift-off protein patterning," *PLOS ONE*, vol. 13, no. 1, p. e0189901, Jan. 2018.

[82] "Photolithographic Patterning of 3D-Formed Polycarbonate Films for Targeted Cell Guiding - Hirschbiel - 2015 - Advanced Materials - Wiley Online Library." [Online]. Available:

https://onlinelibrary.wiley.com/doi/abs/10.1002/adma.201500426. [Accessed: 22-Oct-2019].

[83] I. Wong, X. Ding, C. Wu, and C.-M. Ho, "Accurate and effective live bacteria microarray patterning on thick polycationic polymer layers co-patterned with HMDS," *RSC Adv.*, vol. 2, no. 20, pp. 7673–7676, Aug. 2012.

[84] J. R. Rettig and A. Folch, "Large-Scale Single-Cell Trapping And Imaging Using Microwell Arrays," *Anal. Chem.*, vol. 77, no. 17, pp. 5628–5634, Sep. 2005.

[85] K. Leong, A. K. Boardman, H. Ma, and A. K.-Y. Jen, "Single-Cell Patterning and Adhesion on Chemically Engineered Poly(dimethylsiloxane) Surface," *Langmuir*, vol. 25, no. 8, pp. 4615–4620, Apr. 2009.

[86] J. Xia, Y. Qiu, X. Xun, L. Ma, J. Guan, and M. Su, "Single cell patterning for high throughput sub-cellular toxicity assay," *Analytica Chimica Acta*, vol. 1007, pp. 26–32, May 2018.

[87] D. B. Weibel, W. R. Diluzio, and G. M. Whitesides, "Microfabrication meets microbiology," *Nat. Rev. Microbiol.*, vol. 5, no. 3, pp. 209–218, Mar. 2007.

[88] T. H. Park and M. L. Shuler, "Integration of cell culture and microfabrication technology," *Biotechnol. Prog.*, vol. 19, no. 2, pp. 243–253, Apr. 2003.

[89] D. W. Widmann, "Metallization for integrated circuits using a lift-off technique," *IEEE Journal of Solid-State Circuits*, vol. 11, no. 4, pp. 466–471, Aug. 1976.

[90] R. J. Jackman, D. C. Duffy, O. Cherniavskaya, and G. M. Whitesides, "Using Elastomeric Membranes as Dry Resists and for Dry Lift-Off," *Langmuir*, vol. 15, no. 8, pp. 2973–2984, Apr. 1999.

[91] D. Wright *et al.*, "Reusable, reversibly sealable parylene membranes for cell and protein patterning," *J Biomed Mater Res A*, vol. 85, no. 2, pp. 530–538, May 2008.

[92] J. F. Audiffred, S. E. De Leo, P. K. Brown, H. Hale-Donze, and W. T. Monroe, "Characterization and applications of serum-free induced adhesion in Jurkat suspension cells," *Biotechnol. Bioeng.*, vol. 106, no. 5, pp. 784–793, Aug. 2010.

[93] T. Nakayama, K. Mihara, J. Kawata, H. Kimura, and H. Saitoh, "Adhesion of suspension cells on a coverslip in serum-free conditions," *Anal. Biochem.*, vol. 466, pp. 1–3, Dec. 2014.

[94] M. Tsang, J. Gantchev, F. M. Ghazawi, and I. V. Litvinov, "Protocol for adhesion and immunostaining of lymphocytes and other non-adherent cells in culture," *BioTechniques*, vol. 63, no. 5, pp. 230–233, 01 2017.

[95] C.-Y. Huang, K.-H. Hu, and Z.-H. Wei, "Comparison of cell behavior on pva/pva-gelatin electrospun nanofibers with random and aligned configuration," *Sci Rep*, vol. 6, p. 37960, 05 2016.

[96] C. M. Hassan, P. Trakampan, and N. A. Peppas, "Water Solubility Characteristics of Poly(vinyl alcohol) and Gels Prepared by Freezing/Thawing Processes," in *Water Soluble Polymers: Solutions Properties and Applications*, Z. Amjad, Ed. Boston, MA: Springer US, 2002, pp. 31–40.

[97] N. Q. Balaban *et al.*, "Force and focal adhesion assembly: a close relationship studied using elastic micropatterned substrates," *Nature Cell Biology*, vol. 3, no. 5, pp. 466–472, May 2001.

[98] J. L. Tan, J. Tien, D. M. Pirone, D. S. Gray, K. Bhadriraju, and C. S. Chen, "Cells lying on a bed of microneedles: An approach to isolate mechanical force," *Proceedings of the National Academy of Sciences*, vol. 100, no. 4, pp. 1484–1489, Feb. 2003.

[99] L. R. Volpatti and A. K. Yetisen, "Commercialization of microfluidic devices," *Trends in Biotechnology*, vol. 32, no. 7, pp. 347–350, Jul. 2014.

[100] F. Taub E., J. M. DeLEO, and E. B. Thompson, "Sequential Comparative Hybridizations Analyzed by Computerized Image Processing Can Identify and Quantitate Regulated RNAs," *DNA*, vol. 2, no. 4, pp. 309–327, Dec. 1983.

[101] A. Wainright, U. T. Nguyen, T. Bjornson, and T. D. Boone, "Preconcentration and separation of double-stranded DNA fragments by electrophoresis in plastic microfluidic devices," *ELECTROPHORESIS*, vol. 24, no. 21, pp. 3784–3792, 2003.

[102] C.-C. Lee *et al.*, "Multistep Synthesis of a Radiolabeled Imaging Probe Using Integrated Microfluidics," *Science*, vol. 310, no. 5755, pp. 1793–1796, Dec. 2005.

[103] P. S. Dittrich and A. Manz, "Lab-on-a-chip: microfluidics in drug discovery," *Nat Rev Drug Discov*, vol. 5, no. 3, pp. 210–218, Mar. 2006.

[104] J. Pihl, M. Karlsson, and D. T. Chiu, "Microfluidic technologies in drug discovery," *Drug Discovery Today*, vol. 10, no. 20, pp. 1377–1383, Oct. 2005.

[105] P. J. Hung, P. J. Lee, P. Sabounchi, R. Lin, and L. P. Lee, "Continuous perfusion microfluidic cell culture array for high-throughput cell-based assays," *Biotechnol. Bioeng.*, vol. 89, no. 1, pp. 1–8, Jan. 2005.

[106] A. R. Wheeler *et al.*, "Microfluidic Device for Single-Cell Analysis," *Anal. Chem.*, vol. 75, no. 14, pp. 3581–3586, Jul. 2003.

[107] A. A. Werdich *et al.*, "A microfluidic device to confine a single cardiac myocyte in a sub-nanoliter volume on planar microelectrodes for extracellular potential recordings," *Lab Chip*, vol. 4, no. 4, pp. 357–362, Aug. 2004.

[108] B. G. Chung *et al.*, "Human neural stem cell growth and differentiation in a gradient-generating microfluidic device," *Lab Chip*, vol. 5, no. 4, pp. 401–406, Apr. 2005.

[109] A. M. Taylor, S. W. Rhee, C. H. Tu, D. H. Cribbs, C. W. Cotman, and N. L. Jeon, "Microfluidic Multicompartment Device for Neuroscience Research," *Langmuir*, vol. 19, no. 5, pp. 1551–1556, Mar. 2003.

[110] G. M. Walker, J. Sai, A. Richmond, M. Stremler, C. Y. Chung, and J. P. Wikswo, "Effects of flow and diffusion on chemotaxis studies in a microfabricated gradient generator," *Lab Chip*, vol. 5, no. 6, pp. 611–618, Jun. 2005.

[111] C. M. Pandey *et al.*, "Microfluidics Based Point-of-Care Diagnostics," *Biotechnology Journal*, vol. 13, no. 1, p. 1700047, 2018.

[112] S. K. Sia and L. J. Kricka, "Microfluidics and point-of-care testing," *Lab Chip*, vol. 8, no. 12, pp. 1982–1983, Dec. 2008.

[113] A. Manz *et al.*, "Planar chips technology for miniaturization and integration of separation techniques into monitoring systems: Capillary electrophoresis on a chip," *Journal of Chromatography A*, vol. 593, no. 1, pp. 253–258, Feb. 1992.

[114] T. Thorsen, S. J. Maerkl, and S. R. Quake, "Microfluidic Large-Scale Integration," *Science*, vol. 298, no. 5593, pp. 580–584, Oct. 2002.

[115] D. J. Laser and J. G. Santiago, "A review of micropumps," *J. Micromech. Microeng.*, vol. 14, no. 6, pp. R35–R64, Apr. 2004.

[116] D. B. Weibel, M. Kruithof, S. Potenta, S. K. Sia, A. Lee, and G. M. Whitesides, "Torque-Actuated Valves for Microfluidics," *Anal. Chem.*, vol. 77, no. 15, pp. 4726–4733, Aug. 2005.

[117] J. W. Hong and S. R. Quake, "Integrated nanoliter systems," *Nat Biotechnol*, vol. 21, no. 10, pp. 1179–1183, Oct. 2003.

[118] Y. Yoon *et al.*, "Clogging-free microfluidics for continuous size-based separation of microparticles," *Sci Rep*, vol. 6, no. 1, pp. 1–8, May 2016.

[119] E. Dressaire and A. Sauret, "Clogging of microfluidic systems," *Soft Matter*, vol. 13, no. 1, pp. 37–48, Dec. 2016.

[120] Kai Hu, Feiqiao Yu, Tsung-Yi Ho, and K. Chakrabarty, "Testing of Flow-Based Microfluidic Biochips: Fault Modeling, Test Generation, and Experimental Demonstration," *IEEE Trans. Comput.-Aided Des. Integr. Circuits Syst.*, vol. 33, no. 10, pp. 1463–1475, Oct. 2014.

[121] Y. Chen *et al.*, "A microfluidic circulatory system integrated with capillary-assisted pressure sensors," *Lab Chip*, vol. 17, no. 4, pp. 653–662, Feb. 2017.

[122] N. Mavrogiannis, M. Ibo, X. Fu, F. Crivellari, and Z. Gagnon, "Microfluidics made easy: A robust low-cost constant pressure flow controller for engineers and cell biologists," *Biomicrofluidics*, vol. 10, no. 3, p. 034107, May 2016.

[123] J. R. Lake, K. C. Heyde, and W. C. Ruder, "Low-cost feedback-controlled syringe pressure pumps for microfluidics applications," *PLOS ONE*, vol. 12, no. 4, p. e0175089, Apr. 2017.

[124] M.-C. Liu *et al.*, "Electrofluidic pressure sensor embedded microfluidic device: a study of endothelial cells under hydrostatic pressure and shear stress combinations," *Lab on a Chip*, vol. 13, no. 9, p. 1743, 2013.

[125] R. Li, B. Nie, P. Digiglio, and T. Pan, "Microflotronics: A Flexible, Transparent, Pressure-Sensitive Microfluidic Film," *Adv. Funct. Mater.*, vol. 24, no. 39, pp. 6195–6203, Oct. 2014.

[126] E. P. Kartalov, G. Maltezos, W. F. Anderson, C. R. Taylor, and A. Scherer, "Electrical microfluidic pressure gauge for elastomer microelectromechanical systems.," *J Appl Phys*, vol. 102, no. 8, pp. 84909–849094, 2007.

[127] N. Srivastava and M. A. Burns, "Microfluidic pressure sensing using trapped air compression," *Lab on a Chip*, vol. 7, no. 5, p. 633, 2007.

[128] N. S. Suteria, M. Nekouei, and S. A. Vanapalli, "Microfluidic bypass manometry: highly parallelized measurement of flow resistance of complex channel geometries and trapped droplets," *Lab on a Chip*, vol. 18, no. 2, pp. 343–355, 2018.

[129] W. Song and D. Psaltis, "Optofluidic membrane interferometer: An imaging method for measuring microfluidic pressure and flow rate simultaneously on a chip," *Biomicrofluidics*, vol. 5, no. 4, p. 044110, Dec. 2011.

[130] K. Hosokawa, K. Hanada, and R. Maeda, "A polydimethylsiloxane (PDMS) deformable diffraction grating for monitoring of local pressure in microfluidic devices," *J. Micromech. Microeng.*, vol. 12, no. 1, pp. 1–6, Dec. 2001.

[131] R. N. Palchesko, L. Zhang, Y. Sun, and A. W. Feinberg, "Development of Polydimethylsiloxane Substrates with Tunable Elastic Modulus to Study Cell Mechanobiology in Muscle and Nerve," *PLoS ONE*, vol. 7, no. 12, p. e51499, Dec. 2012.

[132] Z. Wang, A. A. Volinsky, and N. D. Gallant, "Crosslinking effect on polydimethylsiloxane elastic modulus measured by custom-built compression instrument," *Journal of Applied Polymer Science*, vol. 131, no. 22, p. n/a-n/a, Nov. 2014.

[133] T. Smith and J. Guild, "The C.I.E. colorimetric standards and their use," *Trans. Opt. Soc.*, vol. 33, no. 3, pp. 73–134, Jan. 1931.

[134] M. D. Fairchild, *Color Appearance Models*. John Wiley & Sons, 2005.

[135] B. M. Nikolova, G. T. Nikolov, and M. H. Todorov, "Curve Fitting of Sensors' Characteristics," p. 4, 2009.

[136] W. P. Carey and S. S. Yee, "Calibration of nonlinear solid-state sensor arrays using multivariate regression techniques," *Sensors and Actuators B: Chemical*, vol. 9, no. 2, pp. 113–122, Aug. 1992.

[137] S. Sekulic, M. B. Seasholtz, Z. Wang, B. R. Kowalski, S. E. Lee, and B. R. Holt, "Nonlinear multivariate calibration methods in analytical chemistry," p. 11.

[138] D. H. Hagan *et al.*, "Calibration and assessment of electrochemical air quality sensors by co-location with regulatory-grade instruments," *Atmospheric Measurement Techniques*, vol. 11, no. 1, pp. 315–328, Jan. 2018.

[139] N. S. Altman, "An Introduction to Kernel and Nearest-Neighbor Nonparametric Regression," *The American Statistician*, vol. 46, no. 3, pp. 175–185, Aug. 1992.

[140] P.-H. Wu *et al.*, "A comparison of methods to assess cell mechanical properties," *Nature Methods*, vol. 15, no. 7, pp. 491–498, Jul. 2018.

[141] B. F. Kennedy, P. Wijesinghe, and D. D. Sampson, "The emergence of optical elastography in biomedicine," *Nat Photon*, vol. 11, no. 4, pp. 215–221, Apr. 2017.

[142] I. Pushkarsky *et al.*, "Elastomeric sensor surfaces for high-throughput single-cell force cytometry," *Nature Biomedical Engineering*, vol. 2, no. 2, p. 124, Feb. 2018.

[143] C. Wu, X. Zhu, T. Man, P.-S. Chung, M. A. Teitell, and P.-Y. Chiou, "Lift-off cell lithography for cell patterning with clean background," *Lab Chip*, vol. 18, no. 20, pp. 3074–3078, Oct. 2018.

[144] S. Béfahy *et al.*, "Thickness and Elastic Modulus of Plasma Treated PDMS Silica-like Surface Layer," *Langmuir*, vol. 26, no. 5, pp. 3372–3375, Mar. 2010.

[145] S. H. Tan, N.-T. Nguyen, Y. C. Chua, and T. G. Kang, "Oxygen plasma treatment for reducing hydrophobicity of a sealed polydimethylsiloxane microchannel," *Biomicrofluidics*, vol. 4, no. 3, Sep. 2010.

[146] S. van der Walt *et al.*, "scikit-image: image processing in Python," *PeerJ*, vol. 2, p. e453, Jun. 2014.

[147] F. Pedregosa *et al.*, "Scikit-learn: Machine Learning in Python," *Journal of Machine Learning Research*, vol. 12, no. Oct, pp. 2825–2830, 2011.